Crystal ribcage: a platform for probing real-time lung function at cellular resolution in health and disease

Authors: Rohin Banerji[1]†, Gabrielle N. Grifno[1]†, Linzheng Shi[1], Dylan Smolen[1], Rob LeBourdais[1], Johnathan Muhvich[1], Cate Eberman[1], Bradley E. Hiller[2], Jisu Lee[2], Kathryn Regan[1], Siyi Zheng[1], Sue Zhang[1], John Jiang[1], Ahmed A. Raslan[2], Julia C. Breda[2], Riley Pihl[2], Katrina Traber[2], Sarah Mazilli[2], Giovanni Ligresti[2], Joseph P. Mizgerd[2], Béla Suki[1], Hadi T. Nia[1,2*]

Affiliations:
[1] Department of Biomedical Engineering, Boston University; Boston MA
[2] Boston University Pulmonary Center, Chobanian & Avedisian School of Medicine; Boston MA
† These authors contributed equally to this work
[*] Corresponding author. Email: htnia@bu.edu

Abstract
Understanding the dynamic pathogenesis and treatment response in pulmonary diseases requires probing the lung at cellular resolution in real-time. Despite recent progress in intravital imaging, optical imaging of the lung during active respiration and circulation has remained challenging. Here, we introduce the crystal ribcage: a transparent ribcage that (i) allows truly multiscale optical imaging of the lung in health and disease from whole-organ to single cell, (ii) enables the modulation of lung biophysics and immunity through intravascular, intrapulmonary, intraparenchymal, and optogenetic interventions, and (iii) preserves the 3-D architecture, air-liquid interface, cellular diversity, and respiratory-circulatory functions of the lung. Utilizing these unprecedented capabilities on murine models of primary and metastatic lung tumors, respiratory infection, pulmonary fibrosis, emphysema, and acute lung injury we probed how disease progression remodels the respiratory-circulatory functions at the single alveolus and capillary levels. In cancer, we identified the earliest stage of tumorigenesis that compromises alveolar and capillary functions, a key state with consequences on tumor progression and treatment response. In pneumonia, we mapped mutual links between the recruited immune cells and the alveolar-capillary functions. We found that neutrophil migration is strongly and reversibly responsive to vascular pressure with implications for understanding of how lung physiology, altered by disease and anatomical location, affects immune cell activities. The crystal ribcage and its broad applications presented here will facilitate further studies of real-time remodeling of the alveoli and capillaries during pathogenesis of nearly any pulmonary disease, leading to the identification of new targets for treatment strategies.

Introduction
The lung is continuously exposed to mechanical, biological, and immunological stresses throughout its lifetime, and it is the site of many fatal pathologies such as primary and metastatic cancers, respiratory infections, and both obstructive and fibrotic diseases among many others. Exemplified by the COVID-19 pandemic, our understanding of lung pathophysiology is limited. Mechanistic understanding of the complex structure-function of the lung at the cellular level and

its remodeling at the earliest stages of disease requires characterization of cause-effect relationships at multiple scales down to cellular resolution.

Continuous mechanical motion and enclosure by the ribcage makes the lung one of the most challenging organs to study at cellular resolution in real-time while retaining key physiological functions. Clinical imaging modalities (e.g., MRI, CT, and PET) lack the spatiotemporal resolution needed to resolve dynamic alveolar respiratory function, capillary flow, and cellular trafficking and motility. Histological analysis can visualize fixed lungs at subcellular resolution, however the temporal dynamics of lung microphysiology is entirely lost in these "snapshot" images. Recently, intravital microscopy has enabled high resolution imaging of microcirculation in real-time[1-5], which led to major discoveries in lung biology and immunity[2,5-7]. However, these methods compromise the respiratory function of the lung, a defining feature of the pulmonary system with crucial effects on the physics, biology, and immunity of the lung[8-11]. Furthermore, these approaches only visualize a few alveoli of the lung through a small imaging window, and cannot capture whole-organ heterogeneities (e.g., apex vs base lung mechanics) and have limited ability to track rare or dynamic events that may span beyond the imaging window.

Here, in a major departure from existing approaches, we introduce the crystal ribcage, a transparent ribcage that enables optical imaging of nearly the entire surface of a functioning murine lung. The crystal ribcage enables real-time probing of the lung at cellular resolution while its respiratory functions are preserved via positive- or negative-pressure ventilation (as in mechanically assisted or spontaneous breathing), while its circulatory functions are preserved through *ex vivo* pulmonary perfusion of whole blood or media of interest. The crystal ribcage combines the *in vivo* benefits, i.e., preserving the cellular diversity and complex architecture of the lung, with the benefits of organ-on-chip models, i.e., imaging capability and high controllability of microphysiology. These unique capabilities of the crystal ribcage in perturbing the biophysics and immunity of the lung through intrapulmonary, intravascular, and optogenetic interventions while visualizing real-time cellular events in a functioning lung provide enormous opportunities for understanding cause-effect relationships in the pathogenesis of pulmonary diseases.

To this end, we utilized the crystal ribcage to probe remodeling of alveolar and capillary functions in mouse models of primary and metastatic lung cancer, bacterial infection, pulmonary fibrosis, emphysema, and acute lung injury. We identified the earliest stage of tumorigenesis when alveolar structure-functions are compromised and probed the dynamic circulatory functions of capillaries remodeled by tumor growth and pneumonia. Utilizing the controllability of the crystal ribcage combined with the maintenance of *in vivo* complexity, we identified a dramatic and reversible mechano-responsiveness in immune cell migration.

Finally, the unique capabilities of crystal ribcage in imaging and controllability of a functioning lung are scalable to human whole-lung, and adaptable to other organs such as heart, brain, and liver. Given the recent advances in long-term maintenance of large animal and human lung[12,13], brain[14] and liver[15], our transformative approach opens new avenues in transplantation and organ regeneration research in addition to understanding the real-time cellular pathogenesis in functional organs.

Results

Development, validation, and capabilities of the crystal ribcage

The crystal ribcage is a transparent, biocompatible platform designed to provide a physiological environment for a functioning lung *ex vivo* and allows the first truly multiscale optical imaging of the lung in health and disease. The crystal ribcage allows 3-D imaging over the entire surface of the lung (**Fig. 1a**), while uniquely combining the benefits of *in vivo* mouse models (cellular diversity, 3-D lung architecture, breathing and circulation function) and *in vitro* organ-on-chip models[16] (imaging advantages and extensive, precise control over microphysiology) (**Fig. 1b**). We designed the crystal ribcage to mimic the geometry and key properties of the native ribcage to preserve the *in vivo* physiological conditions of the mouse lung during imaging. We used micro computed tomography (μCT) data of mouse chest cavities to create 3-D molds of the ribcage that were specific to the age and strain of mice of interest (in this study: C57/B6, FVB N/J and A/J strains, aged 6-12 weeks). This 3-D mold was used in multi-step additive, sacrificial and thermoforming processes to fabricate the crystal ribcage (**Fig. 1c**, **Extended Data Fig. 1**). To provide the same surface properties as the native parietal pleura in the mouse chest cavity, we engineered the internal surface of the crystal ribcage to be hydrophilic, so that the lung slides freely along it in its natural configuration during ventilation (**Extended Data Fig. 2, Extended Data Movies 1-5**). We fabricated the crystal ribcage to be 150 μm thick (similar to a glass coverslip) for imaging with high-powered objectives (e.g., 60x), and confirmed that the ribcage's curved geometry did not cause optical aberrations (**Extended Data Fig. 3**). We fabricated two versions of crystal ribcage using polystyrene and polydimethylsiloxane (PDMS) as they are biocompatible, free of autofluorescence and ubiquitous in biological research. Polystyrene, used to fabricate petri-dishes, generates a rigid crystal ribcage that is easily scalable to large animal and human lungs, and allows ventilation of the lung using positive- or negative-pressure ventilation (as in mechanically assisted or spontaneous breathing). The rigid crystal ribcage closely mimics the *in vivo* ribcage in quiet breathing as the majority of the lung ventilation is performed by diaphragm[17] (**Extended Data Fig. 4**). PDMS generates a soft crystal ribcage that is partially deformable to mimic the macroscale ribcage deformation that occurs *in vivo* during exercise, sighs, and coughs. Additionally, the PDMS ribcage is pierceable and self-healing to enable intraparenchymal injections. Finally, we confirmed the crystal ribcage does not affect alveolar respiratory function by directly comparing ventilation inside the crystal ribcage to ventilation inside the intact mouse ribcage (**Extended Data Fig. 5**).

To preserve the lung's circulatory and respiratory functions, the crystal ribcage is equipped with custom and commercial external ventilators (for both negative- and positive-pressure ventilation), pumps (uniform and pulsatile), sensors, data acquisition units and displays (**Fig. 1d**). Additionally, we fabricated a custom 6-degree-of-freedom arm to adjust the orientation of the crystal ribcage to directly position the region of interest on the lung surface inside the crystal ribcage overtop or underneath any microscope objective, such that the whole distal lung surface may be imaged as a whole lobe or the desired anatomical location using any optical microscope configuration (**Extended Data Fig. 6**). The ability to image the whole, functional lung surface in its native geometry allows capturing the spatial heterogeneities from the lung apex to the base on both the right and left sides of the lung (**Fig. 1e**, **Extended Data Fig. 6**). This ability is necessary for probing pulmonary diseases that may be localized to specific anatomical regions, such as in a

model of left-lobar pneumonia (**Fig. 1e**), or to capture features that may be rare, such as tumor metastases to the lung. Additionally, the ability to image the whole surface of the functional lung at any magnification enables focusing and tracking of single alveoli as the lung's physiology changes (**Fig. 1f**), for quantitative analyses of lung function at the alveolar scale.

We first quantified alveolar respiratory function by tracking a specific region of interest (ROI) over the normal inspiratory quasi-static pressure range from 3 to 18 cmH_2O[18] and imaging the alveolar geometry at high resolution (**Fig. 1g**). We then computed the sub-alveolar strain (normalized deformation) field (**Fig. 1h**) for the ROI over this pressure range, as an indirect measure of alveolar functionality. While not explicitly representative of the true function of alveoli (gas exchange), alveolar strain across the ventilation cycle is related to it in two ways. First, increasing alveolar volume during inspiration reduces gas pressure in comparison to the opening pressure of airways, driving convective gas transport in the upstream airways. Secondly, increasing alveolar size results in an increased surface area available for gas exchange across the alveolocapillary barrier[19]. Next, we studied how alveolar mechanics would change during dynamic ventilation. We used a confocal microscope equipped with a resonant scanning mirror to continuously image the moving lung at alveolar resolution during positive-pressure ventilation. From the video data, we quantified changes in alveolar diameter across the ventilation cycle at 120 and 60 breaths/min (**Fig. 1i, Extended Data Fig. 7, Extended Data Movie 3, 4**) and found that alveoli near the base of the lung have a larger diameter for a longer duration of the ventilation cycle at higher respiratory rates (120 breaths/min) versus lower rates (60 breaths/min).

We next demonstrated the capability of crystal ribcage to probe the pulmonary circulation in the context of cancer and other pathologies by perfusing a fluorescent tracer through the vasculature and imaging the spatiotemporal dynamics of the dye distribution (**Fig. 1j**). Additionally, we demonstrated the capability of the crystal ribcage to probe single capillary and single cell phenomenon by imaging of capillaries and trafficking of single immune cell within the capillary at high spatiotemporal resolution (**Fig. 1k, Extended Data Fig. 8, Extended Data Movie 6**). The crystal ribcage enables imaging of key resident cell types in the lung, as demonstrated for alveolar type II cells (SPC-GFP+; **Extended Data Fig. 9**), and can be used to visualize the lung illuminated with fluorescent nuclear, membrane, and vascular labels, or through label-free approaches, some of which are demonstrated below.

We demonstrated the versatility of the crystal ribcage to probe lung dysfunction in nearly any pulmonary disease or condition with parenchymal presentation, such as primary and metastatic breast cancer, pneumonia, emphysema, and fibrosis at the whole organ, whole lobe, and alveolar scales (**Fig. 1l**). While we have focused our study on cancer models (**Fig. 2**), and immune response after bacterial infection and acute injury (**Figs. 3-5**), the mouse models of pulmonary fibrosis (**Fig. 1l, Extended Data Figs. 10, 11**) and emphysema (**Fig. 1l**) have been studied briefly for proof-of-concept. We have demonstrated that the disease presentation and remodeling of the structure-function differ dramatically in different diseases. The crystal ribcage can be used to study these differences at multiple scales from whole lobe down to single cells in real-time while maintaining the lung's native geometry and cellular diversity, and retaining control over the tissue physiology.

We demonstrated that crystal ribcage is microscope agnostic by utilizing different imaging modalities including a fluorescent stereomicroscope, confocal and multiphoton microscopes, and

optical coherence tomography (OCT), in both top-down and bottom-up configurations through air, water/oil-immersion objectives (**Extended Data Fig. 6**). Additionally, both a rigid or semi-flexible crystal ribcage can be fabricated to match the geometry of any mouse strain, age, or sex depending on the application (**Extended Data Fig. 1)**. The crystal ribcage fabrication protocol[20] has been successfully reproduced by individuals with different training backgrounds, making it deployable to different institutions.

Figure 1

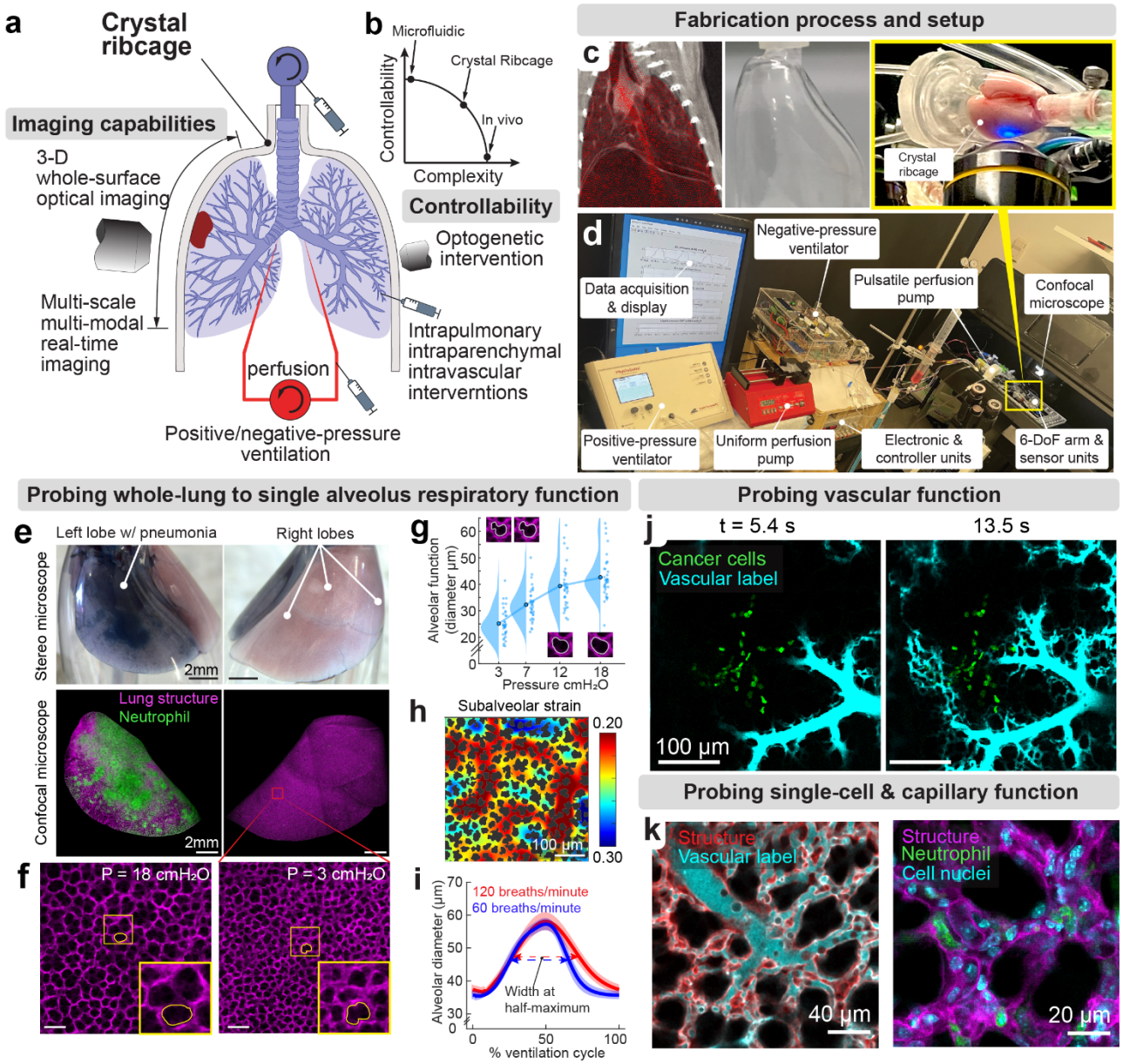
a
Crystal ribcage
Imaging capabilities
3-D whole-surface optical imaging
Multi-scale multi-modal real-time imaging
perfusion
Positive/negative-pressure ventilation
Intrapulmonary intraparenchymal intravascular interverntions
Optogenetic intervention
Controllability
b
Microfluidic
Crystal Ribcage
In vivo
Controllability
Complexity
Fabrication process and setup
c
Crystal ribcage
d
Negative-pressure ventilator
Data acquisition & display
Pulsatile perfusion pump
Confocal microscope
Positive-pressure ventilator
Uniform perfusion pump
Electronic & controller units
6-DoF arm & sensor units
Probing whole-lung to single alveolus respiratory function
e
Left lobe w/ pneumonia
Right lobes
Stereo microscope
2mm
Confocal microscope
Lung structure
Neutrophil
2mm
f
P = 18 cmH₂O
P = 3 cmH₂O
g
Alveolar function (diameter µm)
Pressure cmH₂O
h
Subalveolar strain
0.20
0.30
100 µm
i
120 breaths/minute
60 breaths/minute
Width at half-maximum
Alveolar diameter (µm)
% ventilation cycle
Probing vascular function
j
t = 5.4 s
13.5 s
Cancer cells
Vascular label
100 µm
Probing single-cell & capillary function
k
Structure
Vascular label
40 µm
Structure
Neutrophil
Cell nuclei
20 µm
l
Healthy
Breast cancer lung metastasis
Nodular
Infiltrative
Primary lung cancer
Pneumonia (bacterial)
Pulmonary fibrosis
Emphysema
Whole organ
5mm
Whole lobe
Structure
2000µm
Nodular (MMTV)
Infiltrative (E0771)
Neutrophil (MRP8+)
Alveolus level
Structure
100µm
Nodular (MMTV)
Infiltrative (E0771)
Primary tumor
Neutrophil (inside alveoli)
Collagen (SHG)
Fibrotic region
Emphysematous alveoli

FIGURE 1 | Development, capabilities, and application of crystal ribcage in pulmonary research. (a) Schematic representation of imaging, controllability, and intervention capabilities of the crystal ribcage for mechanistic studies of the lung in health and disease. **(b)** The crystal ribcage benefits from the imaging capability and controllability of organ-on-chip models while preserving the complexities and cellular diversity of *in vivo* models. **(c)** Age- and strain-specific μCT scans used to model the mouse chest cavity to fabricate the crystal ribcage through a multistep additive and sacrificial fabrication process. **(d)** The portable platform to maintain, monitor, and record the physiological condition of the lung during imaging in the crystal ribcage. Crystal ribcage and a functioning lung is shown during real-time imaging. **(e)** The crystal ribcage allows the visualization of nearly the entire surface of the lung with the intact 3-D geometry, demonstrated by both stereomicroscope imaging of the right and left lobes of a mouse lung with a left-lobar bacterial pneumonia infection (labeled by leakage of intravascular Evans blue into the lung airspace), and confocal microscopy showing neutrophil infiltration into the lung parenchyma 24 hours after the start of infection. **(f)** The ability to navigate to desired regions of the lung, here two contoured alveoli, and image the lung at multiple spatial scales across the respiratory cycle under quasi-static conditions. **(g)** Detailed analysis of lung function by measuring alveolar diameter as a function of air pressure during quasi-static ventilation, presented as a distribution of diameters connected by the mean from m = 4 ROI taken from n = 4 mice. **(h)** Representative map of the strain experienced by the alveolar septum during quasi-static ventilation, with sub-alveolus resolution for 1 ROI. **(i)** The alveolar diameter measured at distinct points of the ventilation cycle during dynamic ventilation at 120 and 60 breaths/min presented as the mean ± SEM of data from m = 4 ROI from n = 2 mice **(j)** Remodeling of single capillary function in lung cancer in the crystal ribcage is assessed by real-time confocal microscopy of the spatiotemporal distribution of a bolus of Cascade Blue-dextran (10 kDa) to label the vascular flow under quasi-static inflation. **(k)** Single cell scale confocal microscopy allows probing relationships between cellular activity and alveolar-capillary structure-function during quasi-static ventilation. **(l)** The crystal ribcage is capable of probing nearly any pulmonary disease with parenchymal presentation, as demonstrated on models of breast cancer lung metastasis, primary lung cancer, respiratory infection, pulmonary fibrosis, and emphysema at length and functional scales starting at the whole organ down to single alveoli, single capillaries, and single cells, imaged here by confocal and multi-photon microscopy.

Disruption of alveolar and capillary dynamics by tumor growth

Primary lung cancer is among the leading fatal cancers in both men and women[21]. The lung is also one of the major sites of metastasis for many cancer types including breast cancer[22]. While early steps of cancer cell extravasation and immune interactions have been studied using intravital microscopy in a lung immobilized by glue or vacuum[1,3], understanding of tumor dynamics during active respiration and circulation is lacking. Equipped with the crystal ribcage, we probed how tumor remodeling of the lung parenchyma disrupts respiratory and circulatory functions at the alveolus and capillary level. The ability to visualize the lung structure-function from single cell to whole-organ level (**Extended Data Fig. 12**, **Extended Data Movie 7**) has provided an unprecedented insight into lung-tumor interactions in mouse models of breast cancer lung metastasis and carcinogen-induced primary lung cancer.

To answer long-standing questions surrounding remodeling of the structure and function of the alveoli by tumors, we investigated two mouse models of breast cancer lung metastasis with differential growth patterns. According to our previous work[23] and others[24], tumor growth patterns are generally categorized as *nodular* (growth as a dense nodule that pushes the existing normal tissue outward) or *infiltrative* (cancer cells replace normal cells with minimal remodeling of surrounding architecture and blood vessels; also known as co-optive[24]), with distinct biological and clinical outcomes. These designations have been studied the most extensively in the context of angiogenesis, where infiltrative tumors co-opt the tissue's existing blood vessels and structure and initiate less angiogenesis. In contrast, nodular tumors disrupt the existing microarchitecture and form new blood vessels[24]. The genetic mechanisms that drive nodular versus infiltrative phenotypes are not well understood, however inhibiting pathways such as Wnt7 have been shown to reduce the infiltrative) phenotype in some cases, sensitizing the tumors to anti-angiogenic

therapies[25]. We have previously characterized the infiltrative vs growth pattern in primary brain tumors (e.g. glioblastoma, known to be infiltrative) versus metastatic brain tumors (known to be largely nodular)[23]. Surprisingly, the same two phenotypes were also observed in breast cancer metastasis to the lung.

Motivated by these works, we probed the differential remodeling of the peritumor microenvironment[26] by nodular versus infiltrative lung metastases. We designed experiments to show how nodular vs. infiltrative tumors remodel the structure-function relationship of single alveoli and capillaries in the peritumor environment. We modeled nodular and infiltrative metastatic tumors using murine breast cancer cell lines MCa-M3C-H2B-dendra2 and E0771-H2B-dendra2, respectively (**Fig. 2a, b**). The nodular phenotype tumors appeared to both "push" into the lung tissue and bulge out of the pleural surface of the lung, while the infiltrative phenotype appeared to replace the existing lung tissue and was located superficially on the pleural surface (**Extended Data Fig. 13**). Upon probing the mechanics of local alveoli, we observed that alveoli filled with nodular tumors in the range of 100-200 μm in diameter (**Fig. 2a**) had impaired respiratory function, as they lacked the ability to change volume, which is needed to participate in gas exchange during breathing. Interestingly, these alveoli remained maximally dilated across all quasi-static alveolar pressures, indicating that the nodular cancer cells fill the entire airspace, distending the alveoli open to their maximum volume. Additionally, functional impairment extended up to 1-2 alveoli into the peritumoral region (**Extended Data Fig. 14**). Larger nodules on the scale of 1-2 mm in diameter caused alveoli to become stretched and compacted up to 200 μm away from the tumor boundary (**Extended Data Fig. 12**) but maintain larger diameters at larger distances. While we have the ability to study very large nodules where the entire lung surface is replaced by tumors (**Extended Data Fig. 14**), we chose to focus on smaller nodular tumors to study the local remodeling dynamics when tumors are initially established in the lung. In contrast to the nodular phenotype, the infiltrative phenotype tumors did not compromise alveolar respiratory function either intratumorally or peritumorally, and the alveoli functioned similarly to normal ones far away from the tumor (**Fig. 2b**), suggesting it merely takes over the existing structure of the lung without drastically altering the alveolar function. In a carcinogen-induced model of primary lung cancer, early-stage tumors presented with a nodular-like phenotype. However, the peritumoral alveoli presented as emphysematous, as microscopy revealed that multiple alveoli had coalesced into a single large alveolus near the lesions (**Fig. 2c**). These emphysema-like alveoli were almost twice as large as alveoli far from the tumor and were not as responsive to applied increases in quasi-static alveolar pressure (**Fig. 2c**). This indicated that, despite not being directly filled with cancer cells, these alveoli still had reduced functionality compared to unaffected alveoli in the same lung.

Structural remodeling of the extracellular matrix (ECM) by tumors is known to be strongly correlated to progression and invasion of tumors[27,28]. To investigate whether lung structure is remodeled by breast cancer metastases, we investigated the collagen structure of nodular and infiltrative metastatic tumors using two-photon second-harmonic generation (SHG) microscopy. Analysis of the collagen structure showed that established nodules remodel the local extracellular matrix in the tumor region, causing collagen fibers to become stretched (**Fig. 2d**) in comparison to the wavy collagen structures in the healthy lung. These straightened fibers indicate that the walls of the alveoli adjacent to nodular tumors are under tension (stretched) independent of the breathing cycle (**Extended Data Fig. 12**), such that alveoli cannot expand or contract, and thus cannot

participate in gas exchange. In contrast, collagen fibers surrounding infiltrative tumor patches retained the same characteristic waviness seen in healthy tissue, implying that the structure-function of the alveoli remained unaffected in infiltrative tumor growth. We also assessed alveolar function by computing the strain in the walls of single alveoli using an image registration algorithm, which we adapted and validated for lung microscopy (**Extended Data Fig. 15-17**). Reduced strain in the septal walls during quasi-static ventilation indicates reduced alveolar functionality. In comparing the strain maps between the three different tumor types, the drastic structural remodeling by nodular metastatic breast cancer caused the most severe dysfunction in the surrounding alveoli, followed by the primary cancer nodules, and infiltrative metastatic breast cancer barely impacted local alveolar strain (**Fig. 2e**). In addition to impacting alveolar function, remodeling of lung collagen by nodular tumors has implications for long-term tumor progression, and has been linked to modulating immune behavior in the tumor microenvironment[29].

Next, we studied how mechanical interactions between metastatic cancer cells and the lung tissue may be bi-directional at different stages of lung metastasis. We found that single cancer cells sequestered inside lung capillaries do not impact alveolar strain, but instead experience deformation themselves (**Fig. 2f**). When arrested inside capillaries (confirmed by observing that the cell volume excludes the vascular lumen; **Extended Data Fig. 18**), the single cancer cells experience substantial strain and have lower circularity at all alveolar pressures in comparison to cells in larger arterioles and venules (**Fig. 2g**). It has been previously suggested that cancer cells experience high, cyclic mechanical forces in lung capillaries, and this has contributed to tumorigenesis in *in vitro*[30]. However, we directly show that single cancer cells experience deformation and changes in circularity in response to alveolar pressure within the complex 3-D vascular architecture in a functional lung, similar to what we previously reported for cell-sized polyacrylamide beads of predetermined, uniform stiffness[31]. Next, we aimed to find the smallest number of cells needed for a metastatic nodule to begin disrupting local alveolar respiratory function. We found that nodules larger than 7-10 cells in diameter (approximately the size of one inflated alveolus) was the critical size needed to cause a reduction in the strain of local alveoli for the nodular metastasis phenotype (**Fig. 2h**). This can be attributed again to prevalent remodeling by the cancer bulk[32-35] which stretches the collagen fibers and in turn prevents alveolar septal walls from responding to changing air pressure. Interestingly, the interactions between cancer cells and alveoli are bi-directional: although single cancer cells sequestered in capillaries are deformed across the breathing cycle, clusters larger than ten cells dampen or eliminate alveolar functionality.

Given that nodular tumors dramatically remodeled alveolar respiratory function, we next investigated whether capillary function was affected by studying the remodeled intra- and peritumor capillary structure-function in nodular cancer. The external controllable perfusion unit was used to deliver a bolus of fluorescent Cascade blue dextran (10 kDa) under constant 15 cmH_2O pressure-controlled flow (approximate median vascular pressure at the mouse pulmonary artery[36]), creating a flow of ~1 ml/min into the lung perfused with RPMI cell culture media inside the crystal ribcage. Time lapse imaging of the dye transport showed its exclusion from the tumor bulk and peritumor up to ~100 μm (approximately two alveoli) away from the tumor, indicating that remodeling of native blood vessels near and inside the tumor causes them to lose circulatory function (**Fig. 2i**). The capillary remodeling reduced the intensity of the dye in the tumor in comparison to the capillaries far from the tumor and trended towards longer dye arrival times inside tumors than in the peritumor region and surrounding functional capillary bed, far from the tumor (**Fig. 2j**). We observed such disruption of capillary function even in the presence of

dispersed single cancer cells before the formation of established tumors (**Extended Data Fig. 19, Extended Data Movie 8**). Additionally, we found that the dynamics of dye transport in the *ex vivo* lungs were similar whether the perfusion medium was RPMI cell culture medium, as previously reported in studies of *ex vivo* lung perfusion[37], or whole blood (**Extended Data Fig. 20**), indicating that perfusion dynamics for flow conditions of ~1 ml/min in the crystal ribcage are not significantly altered by changes in perfusate viscosity and presence of blood cells.

As convective flow through capillaries was insufficient to perfuse the tumor vasculature, we investigated the rate of passive diffusion in established nodular lung tumors. A smaller molecular weight fluorescent tracer (CBhydrazide, 550 Da), similar in size to small-molecule drugs, was perfused in a controlled manner until background fluorescence reached steady state. Continuous imaging of the tumors as small as 150 μm for over 60 minutes demonstrated a noticeable diffusion process into the tumor bulk (**Fig. 2k**). By fitting a mathematical model based on the diffusion equation to the rate of increase in fluorescence intensity inside the tumor (see Methods), we were able to estimate the diffusion coefficient of nodular tumors, a key parameter determining the rate of the drug and nutrient delivery to the core of the tumor, to be 3.25 $\mu m^2/s$, consistent with what is reported in melanoma tumors[38].

Overall, we have utilized the crystal ribcage to probe alveolar and vascular dynamics in the vicinity of lung tumors from whole lobe to single cell scale. We have used this capability to probe the remodeling of structure-function relationships at the single alveolus scale in different growth pattern phenotypes. Additionally, we have identified the earliest stage of tumorigenesis when alveolar structure-function and circulatory function begins to be compromised.

Figure 2

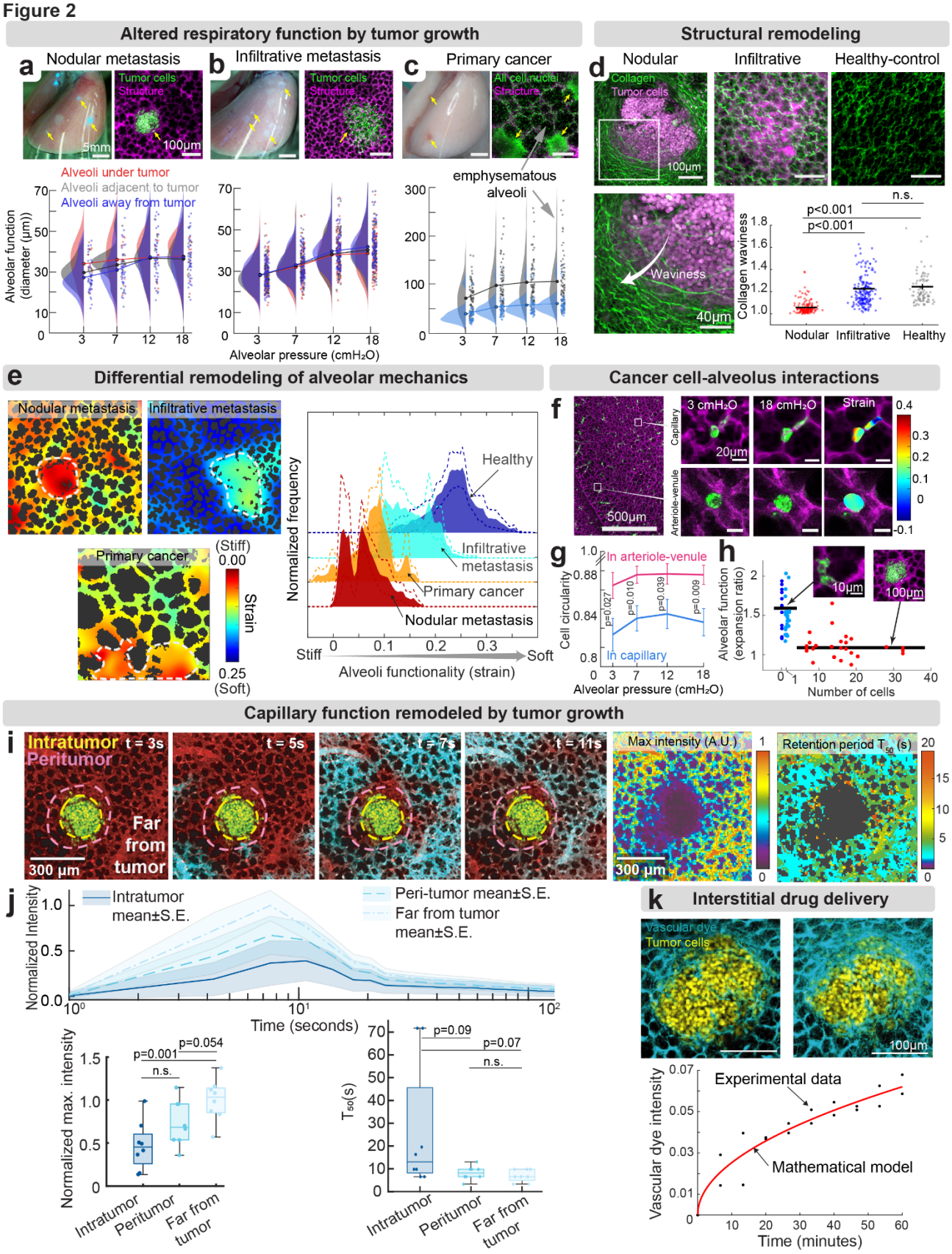
Altered respiratory function by tumor growth
Structural remodeling
a Nodular metastasis
b Infiltrative metastasis
c Primary cancer
d Nodular
Infiltrative
Healthy-control
Tumor cells
Structure
All cell nuclei
Collagen
5mm
100μm
Alveoli under tumor
Alveoli adjacent to tumor
Alveoli away from tumor
emphysematous alveoli
Alveolar function (diameter (μm))
Alveolar pressure (cmH₂O)
Waviness
40μm
Collagen waviness
p<0.001
n.s.
e Differential remodeling of alveolar mechanics
Cancer cell-alveolus interactions
Nodular metastasis
Infiltrative metastasis
Primary cancer
(Stiff) 0.00
0.25 (Soft)
Strain
Normalized frequency
Healthy
Infiltrative metastasis
Primary cancer
Nodular metastasis
Stiff
Soft
Alveoli functionality (strain)
f
3 cmH₂O
18 cmH₂O
Strain
Capillary
Arteriole-venule
20μm
500μm
g
In arteriole-venule
In capillary
Cell circularity
p=0.027
p=0.010
p=0.039
p=0.009
Alveolar pressure (cmH₂O)
h
Alveolar function (expansion ratio)
10μm
100μm
Number of cells
Capillary function remodeled by tumor growth
i
Intratumor
Peritumor
t = 3s
t = 5s
t = 7s
t = 11s
Far from tumor
300 μm
Max intensity (A.U.)
Retention period T50 (s)
j
Intratumor mean±S.E.
Peri-tumor mean±S.E.
Far from tumor mean±S.E.
Normalized Intensity
Time (seconds)
Normalized max. intensity
p=0.001
p=0.054
n.s.
T50(s)
p=0.09
p=0.07
n.s.
Intratumor
Peritumor
Far from tumor
k Interstitial drug delivery
Vascular dye
Tumor cells
100μm
Vascular dye intensity
Experimental data
Mathematical model
Time (minutes)

FIGURE 2 | Multi-scale analysis of structure-function changes in different lung cancer models. Imaging tumors (yellow arrow) from whole organ to alveolar-scale and quantification of alveolar function as the diameter at each quas-static pressure for **(a)** representative nodular metastasis (green) surrounded by semi-functional alveoli (magenta) and alveoli quantified for m = 4 ROI from n = 3 mice, **(b)** infiltrative metastasis (green) surrounded by nearly fully functional alveoli (magenta) and alveoli quantified for m = 4 ROI from n = 3 mice, and **(c)** primary lung cancer nodules with adjacent emphysematous alveoli quantified for m = 3 ROI from n = 3 mice. Alveolar diameter is quantified in intratumoral, peritumoral, and regions far from the tumor, and presented as a distribution of the raw data at each pressure point, with lines drawn to connect the mean of the data for each alveolar pressure. **(d)** Surrounding structural changes were imaged using two-photon microscopy to quantify the collagen architecture by second harmonic generation imaging of m = 7 ROI each for nodular (n = 3 mice) and infiltrative (n = 2 mice) cancer, and m = 4 ROI from n = 1 mouse for healthy-control mouse presented with a scatter and mean line of the data for k >100 fibers in each case. **(e)** Altered alveolar functions compared in all three models by comparing the representative alveolar scale heatmap of strain between the lung at pressures of 12 and 7 cmH_2O and an overall comparison of the strain phenotypes from the same distribution of mice used to measure the alveolar diameter. **(f)** Representative strain field that arrested cancer cells experience across the respiration cycle during quasi-static inflation in capillaries vs arterioles/venules. **(g)**. Bulk comparison of circularity of cancer cells tracked at different pressures taken from n = 30 cells in arterioles/venules and n = 40 cells in capillaries where the mean ± SEM is presented and significance is tested between cells in each group at each pressure. (**h**) Alveolar function plotted against cancer nodules of different sizes to show that alveolar functionality decreases with increasing tumor size, with individual nodules represented by scatterplot points, and the mean alveolar expansion ratio for nodules =< 1 cell and >2 cells, out of a total population of n = 60 nodules. **(i)** Real-time imaging of the circulatory function through perfusion of a bolus of Cascade Blue-dextran (10kDa) fluorescent dye (cyan) into lungs perfused with RPMI medium at the capillary level, and its alteration by nodular tumor, during 15 cmH_2O of pressure-controlled flow. **(j)** The remodeled capillary function in the vicinity of nodular tumor was studied by quantifying the distribution and retention of the dye bolus delivered in the vicinity of a tumor nodule (see Methods) for m = 4 ROI from n = 5 healthy mice and m = 8 ROI from n = 4 tumor bearing mice. **(k)** Passive diffusion of a small molecule fluorophore (Cascade Blue Hydrazide, 0.5 kDa, cyan) into the bulk of a nodular tumor is mapped, and the diffusion coefficient of the tumor was estimated by fitting a mathematical model based on Fick's law of diffusion (see Methods). Boxplots present median with 25th and 75th percentiles, whiskers are the maximum and minimum data points not considered outliers. Comparison between groups performed with two-tailed Student's t-test for significance < 0.05.

Multiscale remodeling of respiratory and circulatory functions in pneumonia

Given the significance of pneumonia as one of leading global burdens of disease[39], even prior to the COVID-19 global crisis, we probed the impact of infection and acute injury on lung respiratory and circulatory functions at whole lobe down to single alveolus and single capillary scales. We induced pneumonia infection by instillation of bacterial pneumonia *S. pneumoniae* serotype 3 (Sp3) into the left bronchus of MRP8-mTmG reporter mice in which MRP8+ cells (neutrophil dominant[40]) express green fluorescent protein (GFP) in the cell membrane. Lungs with resulting infections in the left lobe were excised 24-36 hours post infection for microscopy in the crystal ribcage. Imaging the whole lung showed that the hepatized left apex (classic presentation of this disease), was densely packed with MRP8+ neutrophils at both the whole lobe and alveolar scales (**Fig. 3a, b**). The alveolus-level analysis of the respiratory function demonstrated substantial heterogeneities (**Fig. 3b, Extended Data Fig. 21**). We examined the functionality of alveoli over the range of quasi-static applied alveolar pressures (3-18 cmH_2O) as previously reported in whole-lung pressure-volume curves characterized for the mouse[18,41,42]. Further analysis revealed that the diameters of pneumonia-infected alveoli largely remained constant and were similar in size to healthy alveoli imaged at an alveolar pressure of 7 cmH_2O (**Fig. 3c**), indicating that infected alveoli lose the ability to expand and contract in response to changes in alveolar pressure applied at the trachea, due both to neutrophil recruitment and influx of liquid into the alveolar airspace (pulmonary edema), likely as a result of compromised local vascular integrity. We independently

visualized neutrophil recruitment and pulmonary edema in infected alveoli at single alveolus resolution (**Extended Data Fig. 22**), by injecting Evans blue into the tail vein of MRP8+ reporter mice *in vivo*, to label the native serum albumin. In this way, any edema developed *in vivo* during pneumonia infection would be visible by eye (**Fig. 1e**) and would be fluorescently labeled for confocal microscopy (**Extended Data Fig. 23).** Importantly, we found that regions with high neutrophil recruitment closely match pulmonary edema labeled with Evans blue (**Extended Data Fig. 22**). In comparison to disease-free alveoli, the inflammatory response to infection causes a decrease in strain (corresponding to reduced function) at the lobar and alveolar scales, and at the alveolar level, the strain was heterogeneous (**Fig. 3d**). This reduction in respiratory function is due partially to filling of the alveoli with incompressible liquid, raising local surface tension in comparison to healthy tissue (**Fig. 3e**).

Given the importance of systemic drug delivery as a treatment for infection, we next asked whether the recruitment of immune cells and edema in pneumonia affects capillary function. We perfused a bolus of fluorescent tracer (CBhydrazide dye, 550 Da) through the pulmonary vasculature and in real-time mapped the intravascular delivery of the perfusate in areas with partially collapsed alveoli. We found spatial heterogeneities of the fluorescent intensity (representative of a therapeutic drug; **Fig. 3f, Extended Data Movie 9**) in addition to heterogeneities in the arrival and clearance of the perfusate near the infected regions (**Fig. 3g, h**), representing the retention of the drug. Quantification of transport dynamics revealed that the time course of the arrival of a fluorescent tracer in the vasculature was similar for healthy and infected tissue. However, the tracer did not clear away from the infected tissue as quickly as in healthy tissue (**Fig. 3f, g**). In particular, the duration of high fluorescence lasted longer in tissue infected with pneumonia or adjacent to infection than in healthy tissue (**Fig. 3h**). Slow clearance of dye from infected tissue indicates that local vascular function is likely compromised in the injured alveoli, causing the fluorescent tracer to leak into the interstitial space from the vascular space such that it cannot be easily cleared by continuous perfusion (**Fig. 3g, h**). Additionally, vascular dynamics were slower in the injured region in comparison to healthy tissue, suggesting that the dye was likely transported by diffusion rather than convection in the injured tissue (**Fig 3f-i**). While it is unlikely that the infected tissue is totally isolated from the rest of the lung circulation, given that both healthy tissue and injured tissue experienced a comparable maximum fluorescence intensity upon the initial arrival of the fluorescent tracer in the vasculature (**Fig. 3i**), the leakiness of vessels in pneumonia potentially allowed the dye to be delivered faster (represented by time to reach its maximum intensity) than in metastatic tumors (**Extended Data Fig. 24**).

Overall, we demonstrated that lung respiratory and circulation function is remodeled in pneumonia at the whole organ and single alveolus scales. This remodeling influences respiratory and circulatory functions of the lung, which in turn affect (i) delivery of oxygen, nutrient, and therapeutics, and (ii) trafficking, recruitment, and clearance of immune cells with direct impact on the disease progression and treatment response. Using the crystal ribcage, we are now capable of studying multiscale respiration-circulation dynamics to gain understanding both whole organ and alveolus-level dynamics in pneumonia, and probing delivery of therapeutics.

Figure 3

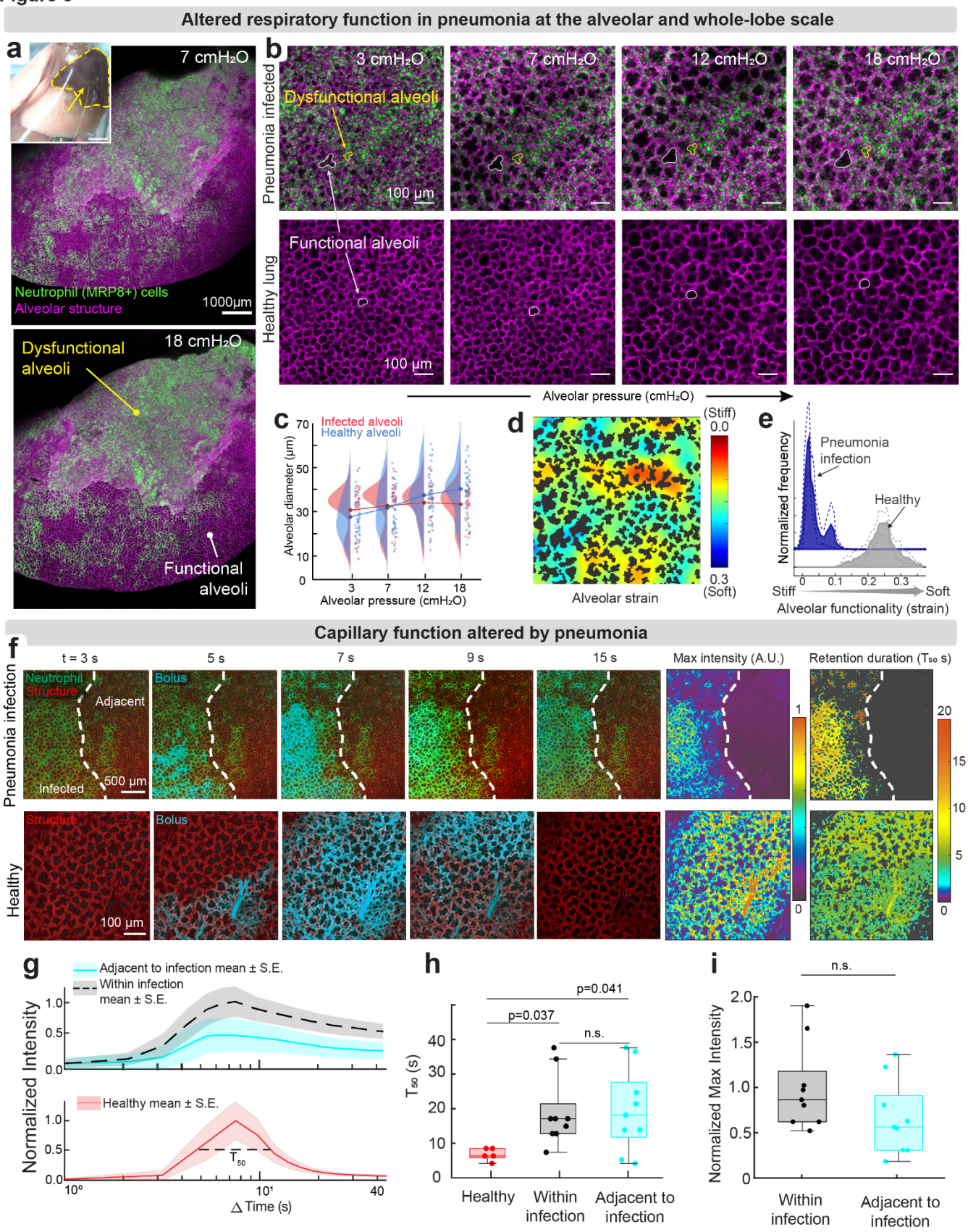
Altered respiratory function in pneumonia at the alveolar and whole-lobe scale
a
7 cmH₂O
Neutrophil (MRP8+) cells
Alveolar structure
1000μm
Dysfunctional alveoli
18 cmH₂O
Functional alveoli
b
3 cmH₂O
7 cmH₂O
12 cmH₂O
18 cmH₂O
Pneumonia infected
Dysfunctional alveoli
100 μm
Healthy lung
Functional alveoli
100 μm
Alveolar pressure (cmH₂O)
c
Infected alveoli
Healthy alveoli
Alveolar diameter (μm)
Alveolar pressure (cmH₂O)
d
(Stiff)
0.0
0.3
(Soft)
Alveolar strain
e
Pneumonia infection
Healthy
Normalized frequency
Stiff
Soft
Alveolar functionality (strain)
Capillary function altered by pneumonia
f
t = 3 s
5 s
7 s
9 s
15 s
Max intensity (A.U.)
Retention duration (T₅₀ s)
Pneumonia infection
Neutrophil
Structure
Adjacent
Infected
500 μm
Bolus
Healthy
Structure
Bolus
100 μm
g
Adjacent to infection mean ± S.E.
Within infection mean ± S.E.
Healthy mean ± S.E.
Normalized Intensity
T₅₀
Δ Time (s)
h
p=0.041
p=0.037
n.s.
T₅₀ (s)
Healthy
Within infection
Adjacent to infection
i
n.s.
Normalized Max Intensity
Within infection
Adjacent to infection

FIGURE 3 | Impairment of alveolar respiratory and circulatory functions in pneumonia. (**a**) Entire left lobe imaged via confocal microscopy at 7 and 18 cmH_2O quasi-static alveolar pressure before navigating to smaller regions of interest to study alveolar scale functionality. (**b**). Representative images of alveolar deformation in a pneumonia-infected mouse versus a healthy mouse in response to alveolar pressure changes. Yellow outlines of single alveoli show that functional alveoli increase in size as alveolar pressure increases, while infected alveoli (marked by neutrophil infiltration) are unresponsive to applied increases in air pressure. (**c**) Alveolar functionality assessed as diameter-pressure curves for infected and healthy alveoli during quasi-static ventilation for m = 6 ROI from n = 4 mice presented as a distribution of the data connected by a line at the mean of each group. (**d**) Representative spatial strain map of alveolar scale strain show that lung tissue strain is reduced in areas filled with neutrophils recruited in pneumonia. (**e**) Strain reduction in alveoli filled with neutrophils show that alveolar function is severely impaired in pneumonia compared to healthy alveoli (same distribution of mice as in alveolar diameter quantification). (**f**) Capillary function in the pneumonia infected regions is compared against healthy lung by comparing the distribution and retention of a bolus of Cascade Blue-dextran (10 kDa) in RPMI medium perfused into the lung under 15 cmH_2O pressure-controlled flow at an alveolar pressure of 7 cmH_2O. (**g**) Time course of fluorescence intensity in infected capillaries, capillaries adjacent to infection, and healthy capillaries in response to perfusion of a fluorescent bolus into the lung. (**h**) After perfusing the Cascade Blue-dextran bolus into the lung, quantification of the time duration when fluorescence intensity in the capillary bed was greater than 50% of the maximum intensity, a metric of the tendency for dye to be retained in the capillary bed for m = 4 ROI from n = 5 healthy mice and m = 9 ROI from n = 4 pneumonia mice. (**i**) Maximum fluorescence intensity in healthy and infection-adjacent capillaries after delivery of the dye bolus, for m = 4 ROI from n = 5 healthy mice and m = 9 ROI from n = 4 pneumonia mice. Boxplots present median with 25th and 75th percentiles, whiskers are the maximum and minimum data points not considered outliers. Comparison between groups performed with two-tailed Student's t-test for significance < 0.05.

Neutrophils are reversibly mechano-responsive to vascular pressure

While we observed that inflammation and recruitment of immune cells alter the alveolar and capillary functions, we endeavored to see if the relationship was mutual, i.e., whether the immune cell activity was also altered by changes in alveolar or capillary pressure. Neutrophil recruitment from pulmonary capillaries has differing rules, mechanisms, and constraints than from the systemic post-capillary venules, which have been previously reviewed[43-46]. In particular, the primary site of neutrophil emigration in the pneumonic lung is in the pulmonary capillaries rather than post capillary venules, as is characteristic of other tissues. Intravital microscopy has previously visualized neutrophil migration in the lung through implanted windows on the mouse ribcage[46,47]. However, these approaches do not provide controllability of alveolar and capillary pressures. Using the crystal ribcage, we tracked single neutrophils as they migrate long distances in the lung in real-time while modulating physiologically relevant alveolar and vascular pressures and preserving the air-liquid interface to probe the effects of breathing and circulation dynamics on pulmonary immunity.

We observed dramatic and reversible changes in neutrophil migration speed in response to an applied increase in vascular pressure in mouse models of lipopolysaccharide (LPS) injury and in bacterial pneumonia. In a lobar LPS model of acute injury in MRP8-mTmG mice[48,49] (**Fig. 4a, Extended Data Fig. 25**), we traced the paths of single neutrophils migrating within the injured alveoli in real-time (**Fig. 4b**) while increasing vascular pressure from 0 to 15 cmH_2O. It has been previously reported that the mean arterial pressure in the catheterized *in situ* resting mouse is 13-20 cmH_2O[50-52], and the left atrial pressure is approximately 5.4 cmH_2O[53]. We chose to apply a constant vascular pressure across the capillary bed up to 15 cmH_2O[37,54] as an approximation of the pressure drop between the pulmonary artery and left atrium. We found that neutrophils migrated longer distances (**Fig. 4b**) and nearly twice as fast (**Fig. 4c**) over a five-minute period at 15 cmH_2O compared to zero vascular pressure. This change in speed was also reversible, as neutrophil speed

responded to repeated step-changes in vascular pressure (**Extended Data Fig. 26, Extended Data Movie 10**). We maintained zero-flow conditions to decouple the effects of vascular flow and shear forces on immune cells[55]. We also measured the persistence (ratio of net cell displacement to total path length) of neutrophils while varying vascular pressure and found that it remained unaffected by changing pressure, implying that neutrophils migrate in random directions within the injury area, instead of moving with specific direction as would happen due to vascular flow during active circulation. Due to this lack of vascular flow, we believe it is unlikely that soluble chemokines (the majority of which are bound to proteoglycans) redistribute quickly enough to play a major role in our observed changes in migration speed. Notably, because effects of pressure on neutrophil emigration were similar whether we applied a series of descending or ascending pressure changes (**Extended Data Fig. 26**), we suspect that redistribution of chemokines seems unlikely to be responsible for the relationships here described. Additionally, the geometric and biophysical constraints posed by the lung capillaries largely prevent neutrophil rolling upon endothelial cells, meaning that selectin binding is likely not a strong contributor to the differences in migration speed we observe here[43-46]. So, our results suggest that, within the complex environment of the lung capillary bed, neutrophils either directly respond to changes in vascular pressure or they are indirectly influenced by other factors that change with vascular pressure, such as vascular morphology, the surface density of adhesion molecules and chemokines on the luminal surface of endothelial cells, or alteration in cell junctions in responses to stretch[56-59].

To confirm the mechano-responsive behavior of neutrophils in an independent model, we induced bacterial pneumonia (Sp3) in the left lobe of MRP8-mTmG mice to model infection and found that neutrophils recruited into the capillaries, interstitium and alveolar air space. Imaging infected alveoli (**Fig. 4e**) and tracing migration path lengths (**Fig. 4f**) revealed that neutrophils located in the vascular and interstitial space also migrated a great deal compared to intra-alveolar neutrophils. The neutrophils in the vasculature and interstitium moved almost twice as fast when vascular pressure was increased to 15 cmH_2O similar to LPS-induced injury, while neutrophils located in the intra-alveolar space maintained their low speed of migration regardless of vascular pressure changes (**Fig. 4g**). The persistence of neutrophils in the pneumonia model was also independent of changes in vascular pressure (**Fig. 4h**). We concurrently found that neutrophil speed did not change in response to alveolar pressure (**Fig. 4i**). Lastly, we observed that neutrophils dramatically changed shape and speed while migrating in the lung capillaries. We found that migration speed was directly correlated to cell aspect ratio and inversely related to circularity (**Fig. 4j, Extended Data Movie 11**) implying that they become more elliptical when moving faster.

Overall, we have used the crystal ribcage to combine the benefits of *in vitro* systems that study neutrophil migration in a highly controlled environment with the cellular diversity and complexity of the whole tissue present in *in vivo* disease models. Using this platform, we have probed the mechano-immunity of neutrophil through precise control of the physiological environment, which can be extended to other immune cell types[60].

Figure 4 Neutrophil mechano-responsiveness to vascular pressure

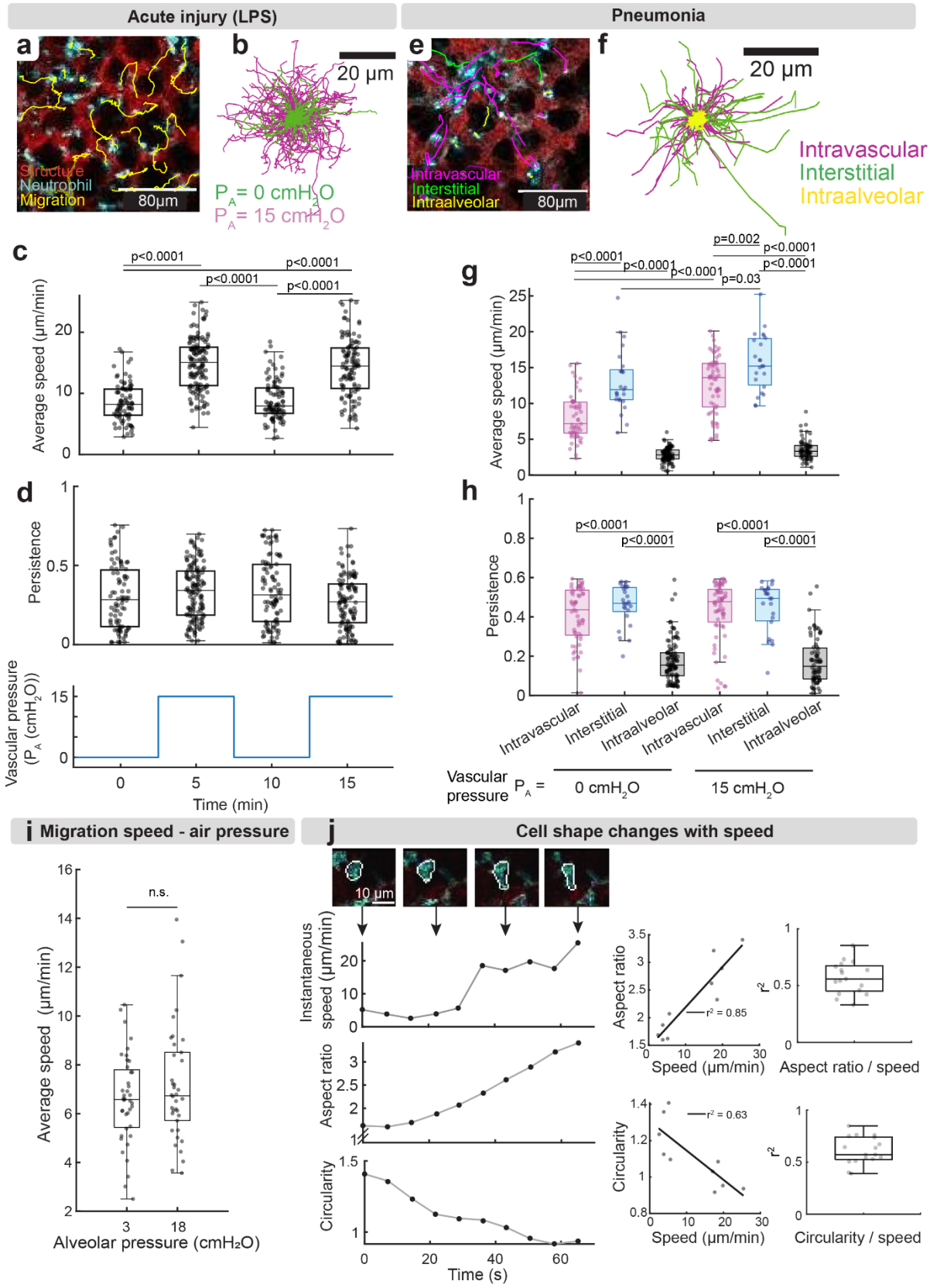

FIGURE 4 | Neutrophil migration is reversibly mechano-responsive to vascular pressure. (**a**) Representative image of neutrophil migration with cell trajectories (yellow) in the LPS model of acute lung injury. (**b**) Neutrophil migration map of paths travelled by single neutrophils over a 5-minute imaging interval. (**c**) Neutrophil average speed increases with vascular pressure and is reversible in LPS-damaged lungs (n = 3 mice), for a constant alveolar pressure of 7 cmH_2O. (**d**) Persistence directionality of neutrophil migration in LPS-damaged lungs. (**e**) Representative traced neutrophil migration in intra-alveolar (yellow), interstitial (green), and intravascular (magenta) spaces in Sp3 pneumonia lungs at a pulmonary artery pressure (PA) of 15 cmH_2O and a constant alveolar pressure of 7 cmH_2O. (**f**) Neutrophil migration map for 15 cmH_2O hydrostatic perfusion pressures and a constant alveolar pressure of 7 cmH_2O in pneumonia lungs for 5 minutes. (**g**) Neutrophil average speed and (**h**) persistence in intra-alveolar, interstitial, and intravascular spaces under 0 or 15 cmH_2O hydrostatic perfusion pressures in pneumonia lungs (n = 3 mice), for a constant alveolar pressure of 7 cmH_2O. (**i**) Neutrophil average speed in pneumonia lungs under quasi-static alveolar pressures (P_{alv}) of 3 versus 18 cmH_2O (n = 2 mice). (**j**) Representative changes in single neutrophil speed, aspect ratio, circularity of the same neutrophil with its respective aspect ratio vs. speed and circularity vs. speed linear regressions, and the regression coefficient of determination of aspect ratio vs. speed and circularity vs. speed of a population of neutrophils (m = 27 cells from n = 3 mice). Boxplots present median with 25th and 75th percentiles, whiskers are the maximum and minimum data points not considered outliers. Comparison between groups performed with two-tailed Student's t-test for significance < 0.05.

Respiration-circulation coupling is disrupted in lung injury

Lung respiration and circulation dynamics are strongly coupled. Assessments of respiration-circulation function at the whole organ level have shown that there is a delicate coupling between the two that regulates the diameter of large blood vessels, which in turn determines pulmonary vascular resistance[61]. However, to our knowledge respiration-circulation coupling has not been characterized at the alveolar-capillary level in real-time. The crystal ribcage enables both imaging and tracking of single capillaries during precisely controlled physiological ventilation and circulation conditions to probe the coupling between these two functions of the lung in health and disease. Taking advantage of these unique capabilities, we quantified the effect of respiration-circulation coupling on the distension of capillaries and arterioles/venules in healthy lungs by simultaneously varying quasi-static alveolar and vascular pressure across a range of physiologically relevant pressures (**Fig. 5a**, **Extended Data Fig. 27**). We found in arterioles-venules that increasing quasi-static alveolar pressure over the entire normal inspiratory pressure range from 3 cmH_2O to 18 cmH_2O caused vascular diameter (inclusive of wall thickness and lumen width) to first increase and then decrease, creating a "bell shaped" curve across the applied vascular pressure range. This interesting pressure response implies that there is an optimum alveolar pressure (between 7-12 cmH_2O) that maximizes arteriole/venule diameter for an intermediate intracapillary blood pressure, resulting in a minimized vascular resistance (**Fig. 5b**). This finding is consistent with previous literature that has established arterioles and venules as the dominant direct regulators of blood pressure[62]. At an intermediate respiratory pressure, the reduced vascular resistance in arterioles and venules may mean that blood cells are rapidly trafficked into or out of the capillary bed. Simultaneously, single capillaries in healthy lung also displayed respiration-circulation coupling. Capillary diameter increased dramatically with increasing vascular pressure (**Fig. 5c**). However, the average diameter trended towards monotonically decreasing when increasing alveolar pressure higher than 7 cmH_2O, for intermediate vascular pressures only (**Fig. 5c**). This indicates that alveolar pressures near 7 cmH_2O would also minimize vascular resistance in capillaries, but that respiration in general does not dominate over vascular pressure in determining capillary diameter.

Acute injury is known to significantly remodel the structure of the lung parenchyma. Having characterized respiration-circulation coupling in the uninjured lung, we next probed whether acute injury (modeled by LPS administration) would remodel respiration-circulation function in addition to tissue structure. Acute injury after LPS was characterized by the presence of a large and inflamed capillary bed at the lung surface (**Fig. 5d**), and reduced size of alveoli across the full breathing cycle. Analysis of capillary diameter with changing alveolar and vascular pressure in the injured area revealed that respiration-circulation coupling is lost in injured capillaries. Increasing vascular pressure did little to increase vascular diameter and increasing air pressure did not consistently reduce vascular diameter, as it had in healthy capillaries (**Fig. 5e**). Thus, the presence of acute injury disrupted the ability of the lung to respond to changes in alveolar and blood pressure, and properly modulate vascular diameter, which could lead to a reduction in local flow and loss of oxygen transport.

The altered respiration-circulation coupling described above may provide insight into neutrophils' mechano-responsiveness to pressure. We observed that populations of neutrophils recruited to a lung infected with bacterial pneumonia migrated faster with increasing vascular pressure (**Fig. 5f**), which was accompanied by an increase in capillary diameter (**Fig. 5g**). However, increasing alveolar pressure in pneumonia lungs did not result in a change in neutrophil speed (**Fig. 5h**), which also did not change the capillary diameters (**Fig. 5i**). This correlation may suggest that changes in vascular diameter and the resulting tensional stresses on the luminal surface of the vasculature are responsible for the changes in neutrophil migration speed, potentially by facilitating binding of neutrophils to the endothelial wall during rolling adhesion[63].

We have used the crystal ribcage to demonstrate that respiration and circulation are coupled at the capillary level in addition to being coupled in upstream, larger vessels. Additionally, we show that the inflammation caused by acute injury remodels the lung parenchyma and disrupts this coupling. Lastly, we have observed that neutrophil migration patterns are correlated with changes in vascular pressure, which are in turn related to changes in vascular diameter, which may give insight into a potential mechanism for neutrophil pressure-responsiveness in the functional lung.

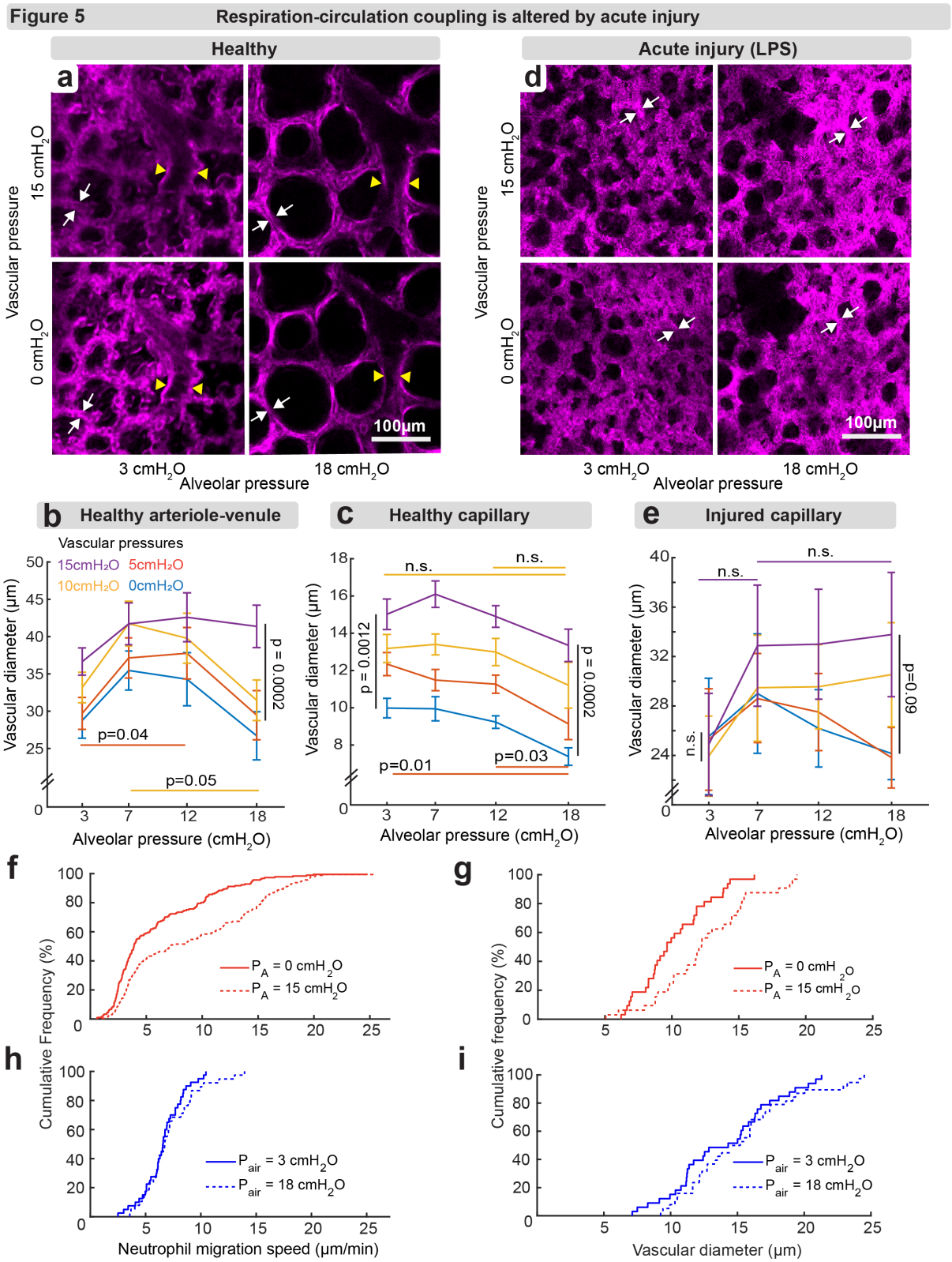

FIGURE 5 | Respiration-circulation coupling in healthy lungs and its disruption by acute injury. (**a**) Representative image of structural changes in the lung associated with variable quasi-static alveolar and vascular pressures, with measurements of diameter changes in single lung capillaries (white arrows) and large arterioles (yellow

arrows), which can be tracked in the crystal ribcage across normal respiration-circulation parameters. Respiration-circulation coupling trends can be observed by measuring the vascular diameter in response to changing pressures of (**b**) large, heathy arterioles and venules (m = 15 ROI from n = 3 mice) and (**c**) healthy capillaries (m = 19 ROI from n = 4 mice). (**d**) Representative images of the injured lung after challenge with LPS, showing that single capillaries (white arrows) affected by acute injury (LPS) become inflamed and distend differently for the same pressure range. (**e**) Capillaries acutely injured after LPS challenge become non-responsive to changes in alveolar and vascular pressure (m = 16 ROI from n = 4 mice). All traces presented as mean ± S.E.M. and p-value determined by testing groups using two-tailed Student's t-test for significance < 0.05. (**f**) Neutrophils migrate at faster speeds as vascular pressure measured at the pulmonary artery (PA) increases (n = 2 mice), potentially associated to the increases in vascular diameter (**g**; n = 2 mice). (**h**) Increasing alveolar air pressure does not cause neutrophils to migrate faster (n = 2 mice), and (**i**) similarly changing air pressure has little effect on vascular diameter (n = 2 mice).

Discussion

We have developed the crystal ribcage and demonstrated its capabilities for probing lung function or dysfunction across nearly the entire surface at the whole-organ, alveolar and cellular scales in real time. Where previous methods are (i) unable to resolve micro-scale features (MRI, CT), (ii) lack temporal dynamics and disrupt the native air-liquid interface (histology), and (iii) compromise respiratory motion (intravital microscopy[1,3]), the crystal ribcage enables imaging of respiratory and circulatory functions down to cellular scale, and preserves the native 3-D and complex architecture and cellular diversity of the lung. We have applied the crystal ribcage to a wide array of pulmonary diseases such as cancer (primary and metastatic), pneumonia, emphysema, and fibrosis (**Fig. 1**). In cancer, we found (i) differential remodeling of alveolar function in nodular vs infiltrative (co-optive) growth pattern, (ii) the earliest stages of tumorigenesis that compromises alveolar respiratory function, and (iii) reduced capillary function around a nodular tumor (**Fig. 2**). In pneumonia, we mapped the spatial heterogeneity of alveolar function at the lobe and alveolar scales and revealed how respiratory and circulatory functions of alveoli and capillaries are altered by inflammation (**Fig. 3**). By modulating vascular pressure in the lung, we found that neutrophils are strongly and reversibly mechano-responsive to vascular pressure in a mouse model of pneumonia and acute lung injury (**Fig. 4**). While more work needs to be done to understand the precise mechanisms that underly neutrophil response to changes in vascular pressure, the capabilities of the crystal ribcage provide enormous opportunity for understanding cause-and-effect in pulmonary disease pathogenesis. Lastly, we demonstrated that respiration and circulation are tightly coupled at the capillary level and found that this coupling is eliminated in acute injury (**Fig. 5**). To better assess the impact of inflammation on blood flow in the capillaries, the crystal ribcage can be used with faster imaging capabilities and higher magnification power to visualize single capillary lumens (**Extended Data Fig. 28**) and future studies will utilize this capability to analyze how respiration-circulation coupling modulates red blood cell trafficking at the capillary level, and whether capillaries become blocked by the presence of immune cells during inflammation, which could cause redistribute flow to other areas.

To further extend our analysis of the effect of acute injury on local respiration and circulation function, we demonstrated the capability of the crystal ribcage to probe lung functionality after surgery. We resected a small portion of tissue from the lung surface and found that the whole lobe was unable to maintain an applied alveolar pressure, as air bubbles could be seen leaking from the incision cite inside the crystal ribcage (**Extended Data Fig. 29, Extended Data Movie 12).** Similarly, we labeled vascular flow through the lung with a bolus of fluorescent dye and observed

that the dye began to leak out of the lung at the incision site. In the clinic, cauterization of the margins of resected lung tissue is often used to prevent air leaks and hemorrhage. We next cauterized a small portion of the lung and observed that vascular flow is faster in the cauterized region, by imaging the transport of a fluorescent dye. Additionally, the cauterized region had a shorter duration of fluorescent intensity than the surrounding tissue (**Extended Data Fig. 30, Extended Data Movie 13**). This implies that cauterization does not fully eliminate vascular function but may compromise local vascular integrity such that diffusion of small molecules into the interstitium is elevated in the injured tissue. Lastly, we explored how introducing a solid phase blockage into the lung would acutely disrupt respiratory and circulatory function. We injected a small volume of fluorescently labelled agarose gel into the sub-pleura of the lung and observed that alveoli in the vicinity of the gel did not change size in response to quasi-static inflation, implying that local respiration was arrested (**Extended Data Fig. 31** and **Extended Data Movie 14**). Additionally, the distribution of a fluorescent bolus of vascular dye across the tissue surface revealed that blood flow was excluded from the gel region, indicating that, local and acute disruptions of the lung structure results in substantial loss of functionality, in addition to the more systemic perturbations introduced in **Fig. 5**.

While the crystal ribcage supports probing of several lung diseases with parenchymal presentation, deeper imaging could expand the capabilities of our platform. Currently, optical imaging of functional lungs is depth-limited due to the diffraction of light at the air-liquid interfaces of the alveoli present in the air-filled lung alveoli[7,8], a limitation that is not related to any property of the crystal ribcage itself. Imaging healthy lungs in the crystal ribcage using laser confocal microscopy, two-photon microscopy, and optical coherence tomography, we can resolve single alveolar structure up to one to two alveoli (50-100μm) deep into the tissue, equivalent to imaging the tissue through a coverslip. When the number of air-liquid interfaces are reduced by flooding the lung with liquid as in pulmonary edema or liquid ventilation strategies, or by a solid phase tissue as in lung tumors, the use of optical coherence tomography enables imaging up to 500 μm deep inside the crystal ribcage, due to reduced light scattering overall (**Extended Data Figs. 12a and 32**). Additionally, in our present work we have probed the lung respiration mechanics under quasi-static conditions to decouple the effects of tissue viscoelasticity and bulk liquid flow from equilibrium elasticity and constant vascular pressure changes. While we have presented limited data using the available dynamic imaging modalities, we had to compromise signal resolution for speed and would be unable to determine the pressure at the alveoli. By using ultrafast volumetric imaging techniques, such as light sheet microscopy (e.g., SCAPE[64]), the crystal ribcage can resolve respiration and circulation dynamics at the "speed of life", i.e. at physiologically relevant respiration and circulation time scales to study the dynamic coupling between circulation and respiration, fast cell-cell communications such as calcium signaling, and quantify viscoelastic properties and energy dissipation at the alveolar level, all in a functioning lung. Additionally, recent optical imaging approaches[65] to measure partial oxygen pressure could be leveraged to study gas exchange in single alveoli via the crystal ribcage, which would provide the experimental evidence needed to better inform our understanding of gas transport mechanisms in deep alveoli[19].

The first iteration of the crystal ribcage, presented here, was designed for the mouse lung to take advantage of the wide range of transgenic and reporter mice available for modeling pulmonary diseases. However, mice models cannot be used to study the effects of gravity on lung function or on lung pathology, such as in ARDS patients[66], and certain diseases such as SARS-CoV-2 are

challenging to accurately model in mice. In future work, we will take advantage of the scalability of our fabrication process to develop the rigid crystal ribcage for large animals like pig and transplant-rejected human lungs[12] to probe diseases and therapeutics in a more clinically relevant setting. We also aim to incorporate crosstalk between other organs and the lung in our model, when relevant to normal or pathophysiology. We have imaged other functioning organs such as the pulsing of the heart atrium on the ventral surface of the crystal ribcage in response to elevated vascular pressure (**Extended Data Fig. 33, Extended Data Movie 15**). Such experiments will allow further probing of circulation-respiration coupling in diseases such as pulmonary hypertension or arrhythmia in the future. Additionally, disease models in this study were developed in the *in vivo* mouse on the order of days-weeks, and we probed the underlying physiology and pathology of these diseases for 4-6 hours *ex vivo* inside the crystal ribcage. This is a sufficient timescale for studying dynamic events such respiration function, immune cell migration, and circulation dynamics. However, recent studies have maintained human lungs up to 24 hours *ex vivo* [67] , pig lungs up to 3 days[68] and rats up to 7 days[69]. Utilizing these advances[70], we will adapt the crystal ribcage to maintain lung viability for multi-day studies of disease dynamics. Specifically, given that the crystal ribcage enables real-time imaging of lung injury and at the single alveolus level, our platform can be used to design strategies for improving human donor lung preservation over time and push the duration of lung viability *ex vivo*, with impacts on lung transplantation research[71].

Overall, the crystal ribcage uniquely combines the precise perturbation and intervention capabilities of *in vitro* lung-on-chip models[8,16] with the multiscale and high spatiotemporal imaging of the whole, functional lung in health and disease. This transformative platform opens the "black box "of the lung for probing the dynamics of pulmonary pathogenesis down to the single cell, with potential for discovery of novel mechanisms and targets relevant not only to disease, but also to lung transplantation, development, and aging.

Acknowledgements: We thank the Neurophotonics Center at Boston University for their generous support and access to their facility. Adam Coats from the Hoffman lab at the University of Iowa provided the μCT image data sets used to fabricate the crystal ribcage. The research reported in this publication was supported by the Boston University Micro and Nano Imaging Facility and the Office of the Director, National Institutes of Health of the National Institutes of Health under award Number S10OD024993, and L.S. acknowledges support from the National Heart, Lung, and Blood Institute Grant 1F30HL168952-01. This material is also based upon work supported by the National Science Foundation, and G.N.G acknowledges support from the NSF Graduate Research Fellowship, Grant No. 2234657. The content is solely the responsibility of the authors and does not necessarily represent the official views of the National Institute of Health. Any opinion, findings, and conclusions or recommendations expressed in this material are those of the authors and do not necessarily reflect the views of the National Science Foundation.

Funding: H.T.N. discloses support for the research described in this study from the National Institutes of Health R21EB031332 and DP2HL168562, Beckman Young Investigator Award, Johnson & Johnson Lung Cancer Initiative, Boston University Center for Multiscale and Translational Mechanobiology, and Dean's Catalyst Award, and the American Cancer Society Institutional Fund at Boston University.

Author contributions: R.B., G.N.G. and H.T.N. conceived the project and wrote the manuscript; R.B. developed and validated the crystal ribcages and external devices suite, established transgenic mouse colonies, analyzed alveolar function, strain maps and collagen waviness; G.N.G. conducted the lung extraction and imaging, generated experimental mice, cultured cancer cells, and analyzed circulatory function data; L.S. analyzed perfusion, vascular transport, and neutrophil mechano-responsiveness data; D.S. analyzed alveolar and capillary function data, and maintained animal colony; R.L. developed registration and strain analysis algorithm; J.M. developed custom hardware for crystal ribcage and analyzed alveolar function data; C.E. developed the deformable crystal ribcage; B.E.H. generated the lobar pneumonia mouse model; J.L. and A.A.R. generated the fibrosis model; A.A.R. performed the histology and staining for fibrotic lungs; J.C.B. generated primary cancer mice, K.R. analyzed alveolar function data and cultured cancer cells; S. Zheng cultured cancer cells; S. Zhang fabricated fluorescent polyacrylamide beads; J.J. assisted in surgical techniques for *in situ* lung imaging; R.P. generated LPS induction model; K.T. provided transgenic MPR8-Cre^{+} mouse; S.M., G.L., J.P.M. and B.S. contributed to discussion on crucial aspects of the project; H.T.N. supervised the project and provided guidance on experimental design, data collection, data interpretation, and writing of the manuscript.

Competing interests: We have received research funding from Johnson & Johnson Lung Cancer Initiative at Boston University. The funding has supported the development of the lung cancer model described in the manuscript.

Data Availability: A demonstration data set has been deposited in a Zenodo repository[72] and are available from DOI: doi.org/10.5281/zenodo.7939072. Additional microscopy data is available on request from the corresponding author.

Code availability: The source code and algorithms used in this study have been deposited in a Zenodo repository[72] and are available from DOI: doi.org/10.5281/zenodo.7939072 licensed under the CC BY 4.0 for use in research.

References

1 Entenberg, D. *et al.* A permanent window for the murine lung enables high-resolution imaging of cancer metastasis. *Nat Methods* **15**, 73-80 (2018). https://doi.org:10.1038/nmeth.4511

2 Headley, M. B. *et al.* Visualization of immediate immune responses to pioneer metastatic cells in the lung. *Nature* **531**, 513-517 (2016). https://doi.org:10.1038/nature16985

3 Looney, M. R. *et al.* Stabilized imaging of immune surveillance in the mouse lung. *Nat Methods* **8**, 91-96 (2011). https://doi.org:10.1038/nmeth.1543

4 Ueki, H., Wang, I. H., Zhao, D., Gunzer, M. & Kawaoka, Y. Multicolor two-photon imaging of in vivo cellular pathophysiology upon influenza virus infection using the two-photon IMPRESS. *Nat Protoc* **15**, 1041-1065 (2020). https://doi.org:10.1038/s41596-019-0275-y

5 Westphalen, K. *et al.* Sessile alveolar macrophages communicate with alveolar epithelium to modulate immunity. *Nature* **506**, 503-506 (2014). https://doi.org:10.1038/nature12902

6 Borriello, L. *et al.* Primary tumor associated macrophages activate programs of invasion and dormancy in disseminating tumor cells. *Nat Commun* **13**, 626 (2022). https://doi.org:10.1038/s41467-022-28076-3

7 Lefrancais, E. *et al.* The lung is a site of platelet biogenesis and a reservoir for haematopoietic progenitors. *Nature* **544**, 105-109 (2017). https://doi.org:10.1038/nature21706

8 Hassell, B. A. *et al.* Human Organ Chip Models Recapitulate Orthotopic Lung Cancer Growth, Therapeutic Responses, and Tumor Dormancy In Vitro. *Cell Rep* **21**, 508-516 (2017). https://doi.org:10.1016/j.celrep.2017.09.043

9 Haudebourg, A. F. *et al.* Respiratory Mechanics of COVID-19- versus Non-COVID-19-associated Acute Respiratory Distress Syndrome. *Am J Respir Crit Care Med* **202**, 287-290 (2020). https://doi.org:10.1164/rccm.202004-1226LE

10 Lederer, D. J. & Martinez, F. J. Idiopathic Pulmonary Fibrosis. *N Engl J Med* **378**, 1811-1823 (2018). https://doi.org:10.1056/NEJMra1705751

11 Suki, B. *et al.* Emphysema and mechanical stress-induced lung remodeling. *Physiology (Bethesda)* **28**, 404-413 (2013). https://doi.org:10.1152/physiol.00041.2013

12 Hozain, A. E. *et al.* Xenogeneic cross-circulation for extracorporeal recovery of injured human lungs. *Nat Med* **26**, 1102-1113 (2020). https://doi.org:10.1038/s41591-020-0971-8

13 Hozain, A. E. *et al.* Multiday maintenance of extracorporeal lungs using cross-circulation with conscious swine. *J Thorac Cardiovasc Surg* **159**, 1640-1653 e1618 (2020). https://doi.org:10.1016/j.jtcvs.2019.09.121

14 Vrselja, Z. *et al.* Restoration of brain circulation and cellular functions hours post-mortem. *Nature* **568**, 336-343 (2019). https://doi.org:10.1038/s41586-019-1099-1

15 Eshmuminov, D. *et al.* An integrated perfusion machine preserves injured human livers for 1 week. *Nat Biotechnol* **38**, 189-198 (2020). https://doi.org:10.1038/s41587-019-0374-x

16 Huh, D. *et al.* Reconstituting organ-level lung functions on a chip. *Science* **328**, 1662-1668 (2010). https://doi.org:10.1126/science.1188302

17 Hall, J. E. *Guyton and hall textbook of medical physiology*. 14. edn, (Elsevier, 2020).

18 Limjunyawong, N., Fallica, J., Horton, M. R. & Mitzner, W. Measurement of the pressure-volume curve in mouse lungs. *J Vis Exp*, 52376 (2015). https://doi.org:10.3791/52376
19 Butler, J. P. & Tsuda, A. Transport of gases between the environment and alveoli--theoretical foundations. *Compr Physiol* **1**, 1301-1316 (2011). https://doi.org:10.1002/cphy.c090016
20 Banerji, R., Grifno, G. N. & Nia, H. T. Design and development of a novel Crystal ribcage for probing real-time lung function at cellular resolution in health and disease. *Protocol Exchange on Research Square* (2023).
21 Collaborators, G. B. D. R. T. C. Global, regional, and national burden of respiratory tract cancers and associated risk factors from 1990 to 2019: a systematic analysis for the Global Burden of Disease Study 2019. *Lancet Respir Med* **9**, 1030-1049 (2021). https://doi.org:10.1016/S2213-2600(21)00164-8
22 Stella, G. M., Kolling, S., Benvenuti, S. & Bortolotto, C. Lung-Seeking Metastases. *Cancers (Basel)* **11** (2019). https://doi.org:10.3390/cancers11071010
23 Seano, G. *et al.* Solid stress in brain tumours causes neuronal loss and neurological dysfunction and can be reversed by lithium. *Nat Biomed Eng* **3**, 230-245 (2019). https://doi.org:10.1038/s41551-018-0334-7
24 Donnem, T. *et al.* Non-angiogenic tumours and their influence on cancer biology. *Nat Rev Cancer* **18**, 323-336 (2018). https://doi.org:10.1038/nrc.2018.14
25 Griveau, A. *et al.* A Glial Signature and Wnt7 Signaling Regulate Glioma-Vascular Interactions and Tumor Microenvironment. *Cancer Cell* **33**, 874-889 e877 (2018). https://doi.org:10.1016/j.ccell.2018.03.020
26 Zhang, S. *et al.* The peritumor microenvironment: physics and immunity. *Trends Cancer* (2023). https://doi.org:10.1016/j.trecan.2023.04.004
27 Conklin, M. W. *et al.* Aligned collagen is a prognostic signature for survival in human breast carcinoma. *Am J Pathol* **178**, 1221-1232 (2011). https://doi.org:10.1016/j.ajpath.2010.11.076
28 Provenzano, P. P. *et al.* Collagen reorganization at the tumor-stromal interface facilitates local invasion. *BMC Med* **4**, 38 (2006). https://doi.org:10.1186/1741-7015-4-38
29 Garcia-Mendoza, M. G. *et al.* Neutrophils drive accelerated tumor progression in the collagen-dense mammary tumor microenvironment. *Breast Cancer Res* **18**, 49 (2016). https://doi.org:10.1186/s13058-016-0703-7
30 Baskaran, J. P. *et al.* Cell shape, and not 2D migration, predicts extracellular matrix-driven 3D cell invasion in breast cancer. *APL Bioeng* **4**, 026105 (2020). https://doi.org:10.1063/1.5143779
31 Zhang, S. *et al.* In vivo multiscale measurements of solid stresses in tumors reveal scale-dependent stress transmission. *Nature Biomedical Engineering* **In press** (2023). https://doi.org:10.21203/rs.3.rs-1697924/v1
32 Nia, H. T. *et al.* Quantifying solid stress and elastic energy from excised or in situ tumors. *Nat Protoc* **13**, 1091-1105 (2018). https://doi.org:10.1038/nprot.2018.020
33 Nia, H. T. *et al.* In vivo compression and imaging in mouse brain to measure the effects of solid stress. *Nat Protoc* **15**, 2321-2340 (2020). https://doi.org:10.1038/s41596-020-0328-2
34 Nia, H. T. *et al.* Solid stress and elastic energy as measures of tumour mechanopathology. *Nat Biomed Eng* **1** (2016). https://doi.org:10.1038/s41551-016-0004

35 Nia, H. T., Munn, L. L. & Jain, R. K. Physical traits of cancer. *Science* **370** (2020). https://doi.org:10.1126/science.aaz0868
36 Thibault, H. B. *et al.* Noninvasive assessment of murine pulmonary arterial pressure: validation and application to models of pulmonary hypertension. *Circ Cardiovasc Imaging* **3**, 157-163 (2010). https://doi.org:10.1161/CIRCIMAGING.109.887109
37 Vanderpool, R. R. & Chesler, N. C. Characterization of the isolated, ventilated, and instrumented mouse lung perfused with pulsatile flow. *J Vis Exp* (2011). https://doi.org:10.3791/2690
38 Alexandrakis, G. *et al.* Two-photon fluorescence correlation microscopy reveals the two-phase nature of transport in tumors. *Nat Med* **10**, 203-207 (2004). https://doi.org:10.1038/nm981
39 Murdoch, D. R. & Howie, S. R. C. The global burden of lower respiratory infections: making progress, but we need to do better. *Lancet Infect Dis* **18**, 1162-1163 (2018). https://doi.org:10.1016/S1473-3099(18)30407-9
40 Passegue, E., Wagner, E. F. & Weissman, I. L. JunB deficiency leads to a myeloproliferative disorder arising from hematopoietic stem cells. *Cell* **119**, 431-443 (2004). https://doi.org:10.1016/j.cell.2004.10.010
41 Eckle, T., Fullbier, L., Grenz, A. & Eltzschig, H. K. Usefulness of pressure-controlled ventilation at high inspiratory pressures to induce acute lung injury in mice. *Am J Physiol Lung Cell Mol Physiol* **295**, L718-724 (2008). https://doi.org:10.1152/ajplung.90298.2008
42 Soutiere, S. E. & Mitzner, W. On defining total lung capacity in the mouse. *J Appl Physiol (1985)* **96**, 1658-1664 (2004). https://doi.org:10.1152/japplphysiol.01098.2003
43 Mizgerd, J. P. Molecular mechanisms of neutrophil recruitment elicited by bacteria in the lungs. *Semin Immunol* **14**, 123-132 (2002). https://doi.org:10.1006/smim.2001.0349
44 Mizgerd, J. P. Acute lower respiratory tract infection. *N Engl J Med* **358**, 716-727 (2008). https://doi.org:10.1056/NEJMra074111
45 Quinton, L. J. & Mizgerd, J. P. Dynamics of lung defense in pneumonia: resistance, resilience, and remodeling. *Annu Rev Physiol* **77**, 407-430 (2015). https://doi.org:10.1146/annurev-physiol-021014-071937
46 Quinton, L. J., Walkey, A. J. & Mizgerd, J. P. Integrative Physiology of Pneumonia. *Physiol Rev* **98**, 1417-1464 (2018). https://doi.org:10.1152/physrev.00032.2017
47 Lefrancais, E., Mallavia, B., Zhuo, H., Calfee, C. S. & Looney, M. R. Maladaptive role of neutrophil extracellular traps in pathogen-induced lung injury. *JCI Insight* **3** (2018). https://doi.org:10.1172/jci.insight.98178
48 Domscheit, H., Hegeman, M. A., Carvalho, N. & Spieth, P. M. Molecular Dynamics of Lipopolysaccharide-Induced Lung Injury in Rodents. *Front Physiol* **11**, 36 (2020). https://doi.org:10.3389/fphys.2020.00036
49 Mitchell, M. J., Lin, K. S. & King, M. R. Fluid shear stress increases neutrophil activation via platelet-activating factor. *Biophys J* **106**, 2243-2253 (2014). https://doi.org:10.1016/j.bpj.2014.04.001
50 Gomez-Arroyo, J. *et al.* A brief overview of mouse models of pulmonary arterial hypertension: problems and prospects. *Am J Physiol Lung Cell Mol Physiol* **302**, L977-991 (2012). https://doi.org:10.1152/ajplung.00362.2011
51 Vanderpool, R. R., Kim, A. R., Molthen, R. & Chesler, N. C. Effects of acute Rho kinase inhibition on chronic hypoxia-induced changes in proximal and distal pulmonary arterial

structure and function. *J Appl Physiol (1985)* **110**, 188-198 (2011). https://doi.org:10.1152/japplphysiol.00533.2010
52 Xiong, M. *et al.* Mouse model of experimental pulmonary hypertension: Lung angiogram and right heart catheterization. *Pulm Circ* **11**, 20458940211041512 (2021). https://doi.org:10.1177/20458940211041512
53 Friedrich, E. E. *et al.* Endothelial cell Piezo1 mediates pressure-induced lung vascular hyperpermeability via disruption of adherens junctions. *Proc Natl Acad Sci U S A* **116**, 12980-12985 (2019). https://doi.org:10.1073/pnas.1902165116
54 Tuchscherer, H. A., Vanderpool, R. R. & Chesler, N. C. Pulmonary vascular remodeling in isolated mouse lungs: effects on pulsatile pressure-flow relationships. *J Biomech* **40**, 993-1001 (2007). https://doi.org:10.1016/j.jbiomech.2006.03.023
55 Huse, M. Mechanical forces in the immune system. *Nat Rev Immunol* **17**, 679-690 (2017). https://doi.org:10.1038/nri.2017.74
56 Kelly, G. T. *et al.* Pulmonary Endothelial Mechanical Sensing and Signaling, a Story of Focal Adhesions and Integrins in Ventilator Induced Lung Injury. *Front Physiol* **10**, 511 (2019). https://doi.org:10.3389/fphys.2019.00511
57 Lai, Y. & Huang, Y. Mechanisms of Mechanical Force Induced Pulmonary Vascular Endothelial Hyperpermeability. *Front Physiol* **12**, 714064 (2021). https://doi.org:10.3389/fphys.2021.714064
58 Shiraishi, K. *et al.* Biophysical forces mediated by respiration maintain lung alveolar epithelial cell fate. *Cell* **186**, 1478-1492 e1415 (2023). https://doi.org:10.1016/j.cell.2023.02.010
59 Zhong, M. *et al.* Alveolar Stretch Activation of Endothelial Piezo1 Protects Adherens Junctions and Lung Vascular Barrier. *Am J Respir Cell Mol Biol* **62**, 168-177 (2020). https://doi.org:10.1165/rcmb.2019-0024OC
60 Jones, D. *et al.* Solid stress impairs lymphocyte infiltration into lymph-node metastases. *Nat Biomed Eng* **5**, 1426-1436 (2021). https://doi.org:10.1038/s41551-021-00766-1
61 Whipp, B. J. & Ward, S. A. Cardiopulmonary coupling during exercise. *J Exp Biol* **100**, 175-193 (1982). https://doi.org:10.1242/jeb.100.1.175
62 Mulvany, M. J. & Aalkjaer, C. Structure and function of small arteries. *Physiol Rev* **70**, 921-961 (1990). https://doi.org:10.1152/physrev.1990.70.4.921
63 Phillipson, M. & Kubes, P. The neutrophil in vascular inflammation. *Nat Med* **17**, 1381-1390 (2011). https://doi.org:10.1038/nm.2514
64 Voleti, V. *et al.* Real-time volumetric microscopy of in vivo dynamics and large-scale samples with SCAPE 2.0. *Nat Methods* **16**, 1054-1062 (2019). https://doi.org:10.1038/s41592-019-0579-4
65 Sakadzic, S. *et al.* Two-photon high-resolution measurement of partial pressure of oxygen in cerebral vasculature and tissue. *Nat Methods* **7**, 755-759 (2010). https://doi.org:10.1038/nmeth.1490
66 Guerin, C. *et al.* Prone positioning in severe acute respiratory distress syndrome. *N Engl J Med* **368**, 2159-2168 (2013). https://doi.org:10.1056/NEJMoa1214103
67 Cardenes, N. *et al.* Human ex vivo lung perfusion: a novel model to study human lung diseases. *Sci Rep* **11**, 490 (2021). https://doi.org:10.1038/s41598-020-79434-4
68 Ali, A. *et al.* Successful 3-day lung preservation using a cyclic normothermic ex vivo lung perfusion strategy. *EBioMedicine* **83**, 104210 (2022). https://doi.org:10.1016/j.ebiom.2022.104210

69 Petersen, T. H., Calle, E. A., Colehour, M. B. & Niklason, L. E. Bioreactor for the long-term culture of lung tissue. *Cell Transplant* **20**, 1117-1126 (2011). https://doi.org:10.3727/096368910X544933
70 Loor, G. *et al.* Prolonged EVLP Using OCS Lung: Cellular and Acellular Perfusates. *Transplantation* **101**, 2303-2311 (2017). https://doi.org:10.1097/TP.0000000000001616
71 Kesseli, S. J., Davis, R. P. & Hartwig, M. G. Commentary: Making lungs great again-introducing new modifications to the Toronto ex vivo lung perfusion protocol. *J Thorac Cardiovasc Surg* **161**, 1974-1975 (2021). https://doi.org:10.1016/j.jtcvs.2020.08.016
72 Banerji, R., Shi, L., LeBourdais, R. & Nia, H. T. Development and demonstration of software tools to complement the real-time cellular resolution imaging capabilities of the crystal ribcage (1.0.0). . *Zenodo* (2023). https://doi.org:10.5281/zenodo.7939073
73 Muzumdar, M. D., Tasic, B., Miyamichi, K., Li, L. & Luo, L. A global double-fluorescent Cre reporter mouse. *Genesis* **45**, 593-605 (2007). https://doi.org:10.1002/dvg.20335
74 Kassie, F., Matise, I., Negia, M., Upadhyaya, P. & Hecht, S. S. Dose-dependent inhibition of tobacco smoke carcinogen-induced lung tumorigenesis in A/J mice by indole-3-carbinol. *Cancer Prev Res (Phila)* **1**, 568-576 (2008). https://doi.org:10.1158/1940-6207.CAPR-08-0064
75 Mizgerd, J. P., Scott, M. L., Spieker, M. R. & Doerschuk, C. M. Functions of IkappaB proteins in inflammatory responses to Escherichia coli LPS in mouse lungs. *Am J Respir Cell Mol Biol* **27**, 575-582 (2002). https://doi.org:10.1165/rcmb.2002-0015OC
76 Barker, K. A. *et al.* Lung-resident memory B cells protect against bacterial pneumonia. *J Clin Invest* **131** (2021). https://doi.org:10.1172/JCI141810
77 Kitzerow, O., Zucker, I. H., Lisco, S. J. & Wang, H. J. Timeline of Multi-Organ Plasma Extravasation After Bleomycin-Induced Acute Lung Injury. *Front Physiol* **13**, 777072 (2022). https://doi.org:10.3389/fphys.2022.777072
78 Mammoto, A. *et al.* Control of lung vascular permeability and endotoxin-induced pulmonary oedema by changes in extracellular matrix mechanics. *Nat Commun* **4**, 1759 (2013). https://doi.org:10.1038/ncomms2774
79 Smith, P., Jeffers, L. A. & Koval, M. Measurement of Lung Vessel and Epithelial Permeability In Vivo with Evans Blue. *Methods Mol Biol* **2367**, 137-148 (2021). https://doi.org:10.1007/7651_2020_345
80 Caporarello, N. *et al.* Dysfunctional ERG signaling drives pulmonary vascular aging and persistent fibrosis. *Nat Commun* **13**, 4170 (2022). https://doi.org:10.1038/s41467-022-31890-4
81 Suki, B., Bartolak-Suki, E. & Rocco, P. R. M. Elastase-Induced Lung Emphysema Models in Mice. *Methods Mol Biol* **1639**, 67-75 (2017). https://doi.org:10.1007/978-1-4939-7163-3_7
82 Kizhakke Puliyakote, A. S. *et al.* Morphometric differences between central vs. surface acini in A/J mice using high-resolution micro-computed tomography. *J Appl Physiol (1985)* **121**, 115-122 (2016). https://doi.org:10.1152/japplphysiol.00317.2016
83 Thiesse, J. *et al.* Lung structure phenotype variation in inbred mouse strains revealed through in vivo micro-CT imaging. *J Appl Physiol (1985)* **109**, 1960-1968 (2010). https://doi.org:10.1152/japplphysiol.01322.2009
84 Vasilescu, D. M. *et al.* Stereological assessment of mouse lung parenchyma via nondestructive, multiscale micro-CT imaging validated by light microscopic histology. *J*

Appl Physiol (1985) **114**, 716-724 (2013). https://doi.org:10.1152/japplphysiol.00855.2012

85 Schulte, H., Muhlfeld, C. & Brandenberger, C. Age-Related Structural and Functional Changes in the Mouse Lung. *Front Physiol* **10**, 1466 (2019). https://doi.org:10.3389/fphys.2019.01466

86 Gokaltun, A., Kang, Y. B. A., Yarmush, M. L., Usta, O. B. & Asatekin, A. Simple Surface Modification of Poly(dimethylsiloxane) via Surface Segregating Smart Polymers for Biomicrofluidics. *Sci Rep* **9**, 7377 (2019). https://doi.org:10.1038/s41598-019-43625-5

87 Allen, M., Poggiali, D., Whitaker, K., Marshall, T. R. & Kievit, R. A. Raincloud plots: a multi-platform tool for robust data visualization. *Wellcome Open Res* **4**, 63 (2019). https://doi.org:10.12688/wellcomeopenres.15191.1

88 Heinrich, M. P., Jenkinson, M., Brady, M. & Schnabel, J. A. MRF-based deformable registration and ventilation estimation of lung CT. *IEEE Trans Med Imaging* **32**, 1239-1248 (2013). https://doi.org:10.1109/TMI.2013.2246577

Methods

Mice

Mice were housed and bred under pathogen–free conditions at the Boston University Animal Science Center. All experiments conformed to ethical principles and guidelines under protocols approved by the Boston University Institutional Animal Care and Use Committee. We used 6-12 week old male and female mice for the experimental procedures. Female FVB mice aged 6-8 weeks (JAX #001800, Jackson Labs, ME) were purchased. A breeding pair of transgenic B6.129(Cg)-Gt(ROSA)26Sortm4(ACTB-tdTomato,-EGFP)Luo/J (JAX #007676, Jackson lab, ME)[73], hereafter referred to as mTmG, was purchased to start a colony and was the primary source of all animals for the experiments. Male neutrophil reporter mice B6.Cg-Tg(S100A8-cre,-EGFP)1Ilw/J (JAX #021614)[40] were purchased from JAX and crossed with in-house homozygous mTmG females to breed MRP8-mTmG mice that were used for neutrophil migration dynamics. We used a 6-week SPC-GFP mouse (Jax #028356) to visualize alveolar epithelial type II cells.

Metastatic cancer model

E0771-H2B-dendra2 mouse cancer cells or MCa-M3C-H2B-dendra2 (both gifts from Rakesh Jain) were used to model breast cancer metastasis to the lung in mTmG and FVB mice, respectively. Cells were cultured in DMEM (Corning) plus 10% fetal bovine serum (Gibco) plus 1% penicillin/streptomycin (Gibco). Cells were harvested at ~80% confluency, washed twice with phosphate buffered saline (PBS), counted, and resuspended in DMEM prior to tail vein injection into mice at a concentration of 2 million per 300uL complete medium. All cell lines tested negative for mycoplasma (Mycoalert Plus Mycoplasma Detection Kit, Lonza, Allendale, NJ), and authenticated before use by IDEXX laboratories (North Grafton, MA). Mice injected with E0771-H2B-dendra2 were sacrificed on days 5-7 post injection for microscopy of mature nodules. Mice injected with MCa-M3C-H2B-dendra2 were sacrificed on days 10-14 for microscopy of mature nodules. For single cell deformation studies, E0771-H2B-dendra2 cells were plasma membrane labeled with 1,1'-Dioctadecyl-3,3,3',3'-Tetramethylindocarbocyanine, 4-Chlorobenzene Sulfonate Salt (DiD, Invitrogen) before imaging, then washed twice with complete cell culture medium and injected intracardiac into the mouse at a concentration of 6 million per 300uL solution. To ensure that single cells were sequestered inside of blood vessels for single cell deformation studies, we tail vein injected a 50 µL volume of bovine FITC-albumin (5 mg/ml, ThermoFisher Scientific, A23015) approximately 10 minutes before intracardiac injection of single cells to label the blood vessel lumens.

Primary cancer model

We induced tumorigenesis in 6-week female A/J mice as described previously[74]. Briefly, we treated the mice with a cocktail of Benzo[a]pyrene (BaP) (B1760, Millipore-Sigma, USA) (0.5 mg/dose) and 4-(Methylnitrosoamino)-1-(3-pyridinyl)-1-butanone (NNK) (78013, Millipore-Sigma) (0.41 mg/dose) were dissolved in cotton oil (C7767, Millipore-Sigma) and delivered to the back of the tongue using a metal 20G feeding tube. The mice were dosed twice per week for 4 weeks to give them a total of 8 doses and then sacrificed at 20 weeks to prepare the tissue for imaging in the crystal ribcage.

LPS acute inflammation model

mTmG mice were treated with 100 µg *Escherichia coli* (*E. coli,* serotype O55:B5, Sigma-Aldrich) lipopolysaccharide (LPS) diluted to 100 ug/60 µL in PBS via intratracheal injection using an

angio-catheter as previously described[75], to model acute injury. Mice were sacrificed 3-4 hours post induction for microscopy of the acutely injured tissue in the *ex vivo* lung.

Bacterial pneumonia model

We induced bacterial pneumonia in mice as previously described[76]. Briefly, *S. pneumoniae* serotype 3 (Sp3) (ATCC; Manassas, VA) was cultured on plates of BBL Trypticase Soy Agar with 5% sheep blood (BD Trypticase Soy Agar II) (BD Biosciences) in a 37°C humidified 5% CO2 environment for 10-11 hours and diluted in 0.9% sodium chloride to the desired optical density. Mice were anesthetized using a ketamine/xylazine cocktail (100 and 10 mg/kg, respectively) and approximately two million CFU in 50 µL were instilled into the left lung lobe via the left bronchus, accessed through the surgically exposed trachea. Mice were sacrificed 24-36 hours post induction for microscopy of the acutely injured tissue in the *ex vivo* lung.

Pulmonary edema visualization

Evans blue has historically been used as a visual marker for vascular leakage and pulmonary edema in rodent models of pulmonary diseases. We labeled pulmonary edema by injecting a mixture of 100 µL of 1.25 mg/ml heparin saline and 50 µl of a 10 mg/ml solution of Evans blue (Fisher Scientific), a far red fluorescent dye that binds serum albumin as previously reported[77-79], into the tail vein of mice infected with Sp3 pneumonia bacteria 3-4 hours in advance of excision of the lungs for microscopy inside the crystal ribcage. Even after pulmonary perfusion with unlabeled RPMI media, edematous regions of the lung retained the characteristic blue color and far-red fluorescence of Evans blue (**Fig. 1e, Extended Data Fig. 22, 23**)

Pulmonary fibrosis model

Bleomycin was delivered to the lungs to generate a model of pulmonary fibrosis as previously described[80]. Mice were anesthetized with ketamine/xylazine cocktail (100 and 10 mg/kg, respectively) and injected intraperitoneally. 1 U/Kg bleomycin (APP Pharmaceutical, LCC Schaumburg, IL, USA) was intratracheally delivered using a 30G insulin syringe. Mice were sacrificed for microscopy of fibrotic injuries 13-14 days after injection. Collagen remodeling in the fibrosis model was visualized using 2-photon second harmonic generated signal (SHG) and validated by Masson's trichrome, immune and col1a1 staining of the same spatial locations that were chosen for 2-photon imaging (**Extended Data Fig. 10, 11)**

Elastase induced emphysema model

COPD was induced in mTmG mice by digesting the elastase in the lung using porcine pancreatic elastase (PPE) (EC134 Elastin Product Company Inc., Owensville, MO). A previously published protocol was followed for single dose treatment[81], briefly 6 IU PPE was dissolved in 100 µL saline and delivered to the mouse (23-25 g). The solution was instilled at the back of the tongue after anesthetizing the mouse and suspending it vertically after which it was allowed to recover normally. Mice were sacrificed at 21 days from instillation to prepare the lung inside the crystal ribcage for imaging.

Lung preparation

Isolated mouse lungs were ventilated through a tracheal cannula for either quasi-static or dynamic ventilation and perfused through two cannulas inserted into the pulmonary artery (PA) and left atrium as previously described[37]. Perfusions included whole blood, cellular, or acellular media

containing fluorescent labels for vascular lumens and circulating cells. After cannulation, the lung-heart bloc was placed into the crystal ribcage for microscopy under controlled ventilation/circulation parameters. The lung was ventilated *ex vivo* using a (Kent Physiosuite Mouse ventilator, Kent Scientific) or held at static alveolar pressure using an air-filled vinyl tube submerged in a water column. Perfusion pressure was controlled using a 60 mL reservoir containing the perfusate medium (serum-free RPMI, Gibco) suspended at different hydrostatic heights above the height of the lung.

In situ lung imaging

Mice were anesthetized as described above and ventilated through a tracheal cannula. The mouse was sacrificed at this point ensuring the lungs did not collapse but maintain a positive end expiratory pressure (PEEP) of 5-7 cmH_2O. The skin and fascia were dissected away and then the intercostal muscles between the ribs was carefully separated under a stereomicroscope till the underlying ribcage pleura was visible. A 2mm x 3mm retaining clamp was inserted in the cleared section to prevent the leftover tissue strands blocking the opening. The PEEP on the lung was altered to confirm that the lung-maintained contact with the internal pleural membrane and that the lung was responsive to pressure changes. The mouse chest carcass was angled upwards for imaging.

Lung microscopy

Prepared *ex vivo* lungs inside the crystal ribcage were imaged under quasi-static inflation conditions or during dynamic ventilation using an inverted laser-scanning confocal microscope (Olympus FV 3000) under objective magnifications of 1.25x, 10x, and 60x, with environmental temperature control set to 37°C using Fluoview acquisition software. The confocal microscope was used with a resonant scanning mirror to increase the imaging speed up to 15 framer per second (FPS) for imaging the dynamically ventilated lung, which increases speed by compromising some of the image resolution. Additionally, lungs were imaged using an upright Nikon fluorescent stereomicroscope, a ThorLabs upright optical coherence tomography probe with a 10x objective and an upright Bruker two-photon microscope equipped with a 16x water immersion objective. Microscopy data was visualized and processed using FIJI and MATLAB2021b.

Histological staining for fibrosis evaluation

Lungs were perfused with 10 mL of sterile cold PBS to remove blood then inflated with 4% Paraformaldehyde (PFA). The trachea was clogged with a thread and lungs were fixed in 4% PFA for 24 h at 24 °C. Fixed lungs were washed in 1x PBS three times 5 min at each interval at 24 °C. Fixed lungs were dehydrated in 50%, 70%, 85%, 95% and 2x 100% ethanol, cleared in 3x Histo-Clear (a xylene substitute, National Diagnostics) and embedded in paraffin. Formalin-fixed paraffin-embedded (FFPE) tissues were cut to serial sections (5 µm). FFPE sections were deparaffinized using a standard protocol of Histo-Clear and alcohol gradients. Masson's trichrome staining was performed by using a commercially available kit (HT15-1KT,Sigma-Aldrich). Hematoxylin and Eosin (H&E) staining was performed using Harris Hematoxylin solution (Thermo Scientific) and Eosin-Y solution (Thermo Scientific). After dehydration in 70%, 95%, and 100% ethanol series and clearance with Histo-Clear, the stained slides were mounted and imaged using Olympus BH-2 light microscope (Olympus).

Immunofluorescence staining for fibrosis samples
FFPE sections were deparaffinized using a standard protocol of Histo-Clear and alcohol gradients. Antigen retrieval was performed by boiling the slides in citrate buffer (10 mM citric acid, 0.05% Tween-20, pH 6.0) for 20 minutes, and then, the slides were allowed to cool at 24 °C for at least 30 min. The slides were washed with PBS and permeabilized with 0.2% Triton-X for 15 minutes. Following blocking in 5% normal donkey serum in PBS containing 0.2% Triton-X for 2 hours at 24 °C. The slides were incubated with an antibody against COL1A1 (rabbit, 1:200, Cell signaling Technology, #72026T) followed by a fluorescence-conjugated secondary antibody (Alexa Fluor 555, ThermoFisher Scientific #A-31572, MA, USA, 1:1000 dilution) and DAPI (Thermo Fisher Scientific #62248, Waltham, MA, USA, 1:1000 dilution) to counterstain nuclei. Stained slides were mounted with Aqua-Poly/Mount (Polysciences, Warrington, PA, USA) and imaged using Olympus CKX53 inverted microscope (Olympus).

Mouse ribcage 3-D object creation
Previously recorded pressure controlled μCT scans of C57B/6 and AJ mice chest cavities were obtained from the Hoffman group at the University of Iowa[82-84]. FVB mouse chest scans were performed at the Boston University Micro-CT imaging facility. These scans were segmented in MATLAB (v. R2019b Mathworks, Natick MA) using a custom algorithm and user defined regions of interest to obtain a coarse 3D object that represented the mouse chest cavity including a small section of the trachea. This coarse 3D binary object was refined and re-meshed in Meshmixer (Autodesk) to remove any sharp edges and make a stereolithography (STL) object. The Meshmixer files were imported into Solidworks 2019 (Dassault systems, France) to add registration features prior to 3D printing. The model was made age-specific by scaling the binary object by mouse lung volume reported by age[85] (**Extended Data Fig. 1**). The final STL file was printed using FormLabs (Somerville, MA) clear resin on a Form3 printer and additionally post-cured for 30 minutes. The final 3D printed insert was washed and polished to remove any layer lines and obtain a high gloss finish on the surface.

Semi-flexible ribcage fabrication
The 3D printed lung insert was used to make a negative mold by embedding it in a soft silicone-based elastomer called Ecoflex 00-30 (Smooth-On Inc, Macungie PA) under vacuum for 5 hours. Post curing the 3D insert was removed to obtain a smooth exact negative mold. The internal surface of the mold was coated with a thin layer of Polymethyldisiloxane (PDMS) to completely seal it from air and make the internal geometry rigid. The negative space was slowly filled with a casting sugar solution that was kept liquid at ~140˚C. The sugar filled mold was degassed in the oven for over an hour to remove any trapped air bubbles in the sugar, cured by cooling over 2 hours at room temperature, and then gently removed by deforming the soft silicone mold. PDMS was mixed in a standard 10:1 monomer to crosslinker ratio and gradually poured over the sugar mold, completely covering the surface, and then set to partially cure at ~50˚C for 25-30 minutes. This was repeated five times after which it was left to cure for 12-18 hours at ~50˚C in a dehydrating oven. The cast PDMS was positioned in a 3D printed crystal ribcage support and attached with dabs of glue. The assembly was then left in lukewarm water for 2-3 hours to dissolve the cast sugar to obtain the PDMS crystal ribcage (**Extended Data Fig. 1**).

Rigid ribcage fabrication

The 3D printed insert was positioned over a miniature dental thermoforming device. A 0.7mm clear polystyrene sheet was fed into the device and allowed to heat before it was pulled over the 3D printed insert while applying a vacuum to remove any trapped air between the mold and the polystyrene. The heat and vacuum were turned off and the formed polystyrene was removed from over the mold using compressed air. This rigid crystal ribcage was fitted into a support neck and fused by friction welding and using cyanoacrylate glue (**Extended Data Fig. 1**).

Crystal ribcage surface treatment

Both rigid and deformable crystal ribcage surfaces have native hydrophobic surfaces which were engineered to be hydrophilic. The polystyrene surface was treated with oxygen plasma using a Harrick Plasma Cleaner, where the crystal ribcage was subjected to a vacuum of 800-900 mTorr and then plasma treatment at medium power for 2 minutes. The internal surface of the PDMS crystal ribcage was treated with a 1% PDMS-PEG Block Copolymer (DBE-712, Gelest Inc., Morrisville, PA) and allowed to cure to improve hydrophilicity as previously described [86].

Versatile microscopy arm

We developed two custom microscopy arms using commercially available photography brackets to allow both 3- and 6-degrees of freedom to orient the crystal ribcage with available upright (fluorescent stereomicroscope, multi-photon microscope, optical coherence tomography) or inverted microscopes (laser scanning confocal microscope) to place the desired region of interest (ROI) on the lung for imaging directly above or below the objective, and thus image any location on the lung from apex to base, on both the right and left lobes (**Extended Data Fig. 6**). For fine focusing, we use the microscopy arm in tandem with the microscope's XYZ stage controls to focus on the desired ROI with micron-scale precision. We successfully tested our mounting arm to image the lung surface with the above microscopes and with a wide range of objective power, ranging from 1.25x (lobe-scale), 10x (alveolar-scale), and 40x, and 60x (subcellular-scale) imaging of the same lung.

Ventilation pressure and flow sensor calibration

Ventilation pressure sensors SSDRRV100MDAA5 (Honeywell Inc.) were rated to measure between ±100 cmH_2O with a 0-5 V linearly scaled output. The pressure sensor was calibrated prior to every experiment with a simple water column between 0-10 cmH_2O and the calibration value was used to scale the raw voltage into pressure values in real-time. The flow sensor was calibrated one-time when it was assembled using a 3D printed constriction and SSDRRV010MDAA5 (Honeywell Inc.) differential ±10 cmH_2O linearly scaled pressure sensor. The obtained voltage-flow curve which was fitted to a reflected power curve to obtain the flow values in ml/min for a given change in resistance read across the sensor. All sensor readings were scaled to real units using an Arduino and custom MATLAB functions to display in real-time.

Perfusion pressure and flow sensor calibration

Perfusion was measured with 26PCAFG6G (Honeywell Inc.) that were rated between 0 to 1 PSI unamplified gauge pressure sensors. The pressure sensor was read into an HX711 analog to digital converter before being read on an onboard Arduino Uno. The scaled digital values were calibrated against a known water column between 0-10 cmH_2O prior to every experiment. The perfusion flow was measured using a small form factor Sensirion SLF-1300F liquid flow sensor. The sensor comes factory calibrated for DI water and 70% ethanol. It was calibrated for different perfusates

by linearly scaling the sensor reading with a known syringe pump driven flow prior to the experiment. All sensor readings were scaled to real units using an Arduino and custom MATLAB functions to display them in real-time.

Quasi-static alveolar diameter measurement

Microscopy images recorded with a 10x objective and an additional 1.5x optical zoom were loaded into FIJI-ImageJ and sum-wise projected in the z-direction for all pressure conditions. Alveoli common to all quasi-static or dynamic pressures were annotated prior to making measurements. The mean alveolar diameter was calculated by recording 2 length values between anatomical features that were diametrically opposite to each other. The mean lengths were recorded for all corresponding alveoli at different pressures. These measurements were compiled in MATLAB R2021b to make raincloud plots[87] and compute group-wise statistics.

Alveolar septum strain calculation

We used a previously published deformable registration algorithm, deedsBCV[88] to autonomously determine the displacement map between images of the lung tissue at different quasi-static inflation pressures, here alveolar pressures of 7 and 12 cmH_2O. We subsequently used a custom algorithm to compute the strain map (**Extended Data Fig. 15, 16**). While finite difference methods could also be applied to obtain the displacement gradient it is subject to noise which can obscure the signal. A cubic smoothing spline was used to approximate the displacement map and evaluate its gradient derivative to then calculate the canonical strain tensors (**Extended Data Fig. 17**) directly. This method gives us a displacement gradient continuous in its second derivatives which avoids obscuring the true signal in the noise. We first validated the obtained displacement maps by applying known displacements to images to register them and compute the strain. We then validated the effect of the smoothing spline on the original and target images to ensure accurate registration between them by using multiple kernel sizes to ensure that the final registered image matches the target image. The final strain computation algorithm was then validated for known synthetic displacement maps (**Extended Data Fig. 17**) to ensure that no fundamental errors existed between the mathematical ground truth and image-based strain estimation.

Dynamic alveolar diameter measurement

The 2-D image series of the lung were loaded in MATLAB R2022a and segmented by applying a global threshold to each image. The binarized images were analyzed using the built-in regionprops() function to obtain the equivalent diameter of each binarized segment. The equivalent diameter is the diameter of a circle with the same area as each binarized segment. Any equivalent diameters greater than 500 μm or less than 10 μm were ignored. The mean diameter of each image was plotted as a time series and the peaks of the curve were obtained to find when the cycle repeats. The total number of frames were linearly distributed to obtain a normalized ventilation cycle. Each cycle in each ROI was pooled to get a single mean alveolar diameter curve per ROI which was pooled together at the different respiratory rates to obtain the width at half-maximum of the ventilation cycle.

Collagen waviness quantification

The 3-D images of the tumor nodules were imaged with a Bruker 2-photon microscope with the laser excitation set at 920 nm. The dendra signal from cancer cells was collected through a 525/50 nm emission filter and the second harmonic generation collagen signal was collected through a

460/50 nm emission filter on separate channels. The speckle noise was removed from the 3-D stack using a 2-pixel median filter in MATLAB R2021b medfilt2() and manual traces were made along the collagen fibers between successive nodes. The total path length traced was divided by the end-end distance of the start and end points of the trace to determine the waviness index which was reported.

Single cell measurement

Microscopy images recorded with a 10x objective with a 4x zoom or 20x objective with 4x zoom were loaded into FIJI-ImageJ for all pressure conditions. Circularity of single cancer cells was computed using the built-in FIJI-ImageJ plugin for assessing cell circularity, which is computed as $Circularity = 4\pi \frac{area}{perimeter^2}$ The maximum plane of the cell was identified by a user and then a freehand trace of the shape of the cell was traced around the cell. Shape parameters including the maximum and minimum Feret diameters were reported by FIJI for every annotation and compiled in MATLAB R2021b to perform statistical comparisons between the Feret ratio (**Extended Data Fig. 18**). We confirmed that single cells were sequestered inside blood vessels by exclusion of FITC-albumin dye, which was injected into the mouse via the tail vein (50 µL of 10 mg/ml FITC-albumin in saline) prior to tail vein injection of singularized cancer cells.

Cancer nodule size estimation

We estimated the size of cancer nodules for the analysis reported in **Fig. 2h** by first assuming an average cell size of 10 µm and measuring the diameter of the cancer nodule in in the XY plane, from confocal microscopy images of nodule-bearing lungs in the crystal ribcage from confocal microscopy images (representative image in **Fig. 2a**). Then we estimated the size of the nodules in terms of cell number by dividing the diameter of the nodule by average cell size and report the estimated size against the functionality of local alveoli from the same image in **Fig. 2h.**

Perfusion and vascular transport imaging

Mouse lungs were perfused with serum-free RPMI at 37°C under a pressure-controlled flow of 15 cmH_2O, approximately 1 ml/min. To model small molecule drug transport, 50 µL of Cascade Blue dextran (10 kDa, Molecular Probes) or Cascade Blue hydrazide trisodium salt (500 Da, Invitrogen) were injected into the perfusion tubing upstream of the pulmonary artery cannula at a concentration of 10 mg/ml over approximately 1 second. Vascular dynamics were imaged over time using a laser-scanning confocal microscope (Olympus FV3000). Post-processing of vascular transport data was performed in MATLAB R2021b. Microscopy recording channels corresponding to impulse bolus injection were down sampled to a mesh grid with single pixel dimensions on the scale of a single alveolus (approximately 50 µm). Intratumor regions were segmented based on the presence of fluorescently labeled tumor cells. Within the extra-tumor regions, the peri-tumor region was segmented from regions far from the tumor based on a reduction of bolus intensity threshold. Sp3 infected areas were segmented based on the presence of fluorescently labeled neutrophils. For perfusion studies in lungs with surgical interventions, we used a microsurgical blade (AD Surgical, Sunnyvale CA) to pierce a hole approximately 250 µm into the pleural surface of the lung (**Extended Data Fig. 29**). For tissue cauterization to locally arrest ventilation, we used a small electrocautery pen (Lifeline Medical Inc., Brooksville FL) to generate burns on the pleural surface of the tissue approximately 1-2 mm in diameter. For both of these surgical interventions, we delivered a 50 µL bolus of Cascade Blue dextran as above to the lung during pulmonary perfusion and imaged the spatiotemporal distribution of the dye bolus in the cauterized versus

uninjured tissue (**Extended Data Fig. 30**). Cauterized regions were segmented based on an increased density of red fluorescent signal due to the use of mTmG reporter mice. For studies where agarose gel was injected into the lung to acutely remodel respiration and circulation function, we loaded approximately 20 µL of 2% agarose gel prepared in water and labeled with 0.1 mg/ml Evans blue dye (Fisher Scientific) into a 30G insulin syringe (Fisher Scientific) and injected it into the sub-pleural region of the lung, prior to placing the tissue inside the crystal ribcage. We imaged the spatiotemporal distribution of a bolus of Cascade Blue dextran in the lung vasculature during pulmonary perfusion near the gel using the same approach as above (**Extended Data Fig. 31**).

Perfusion and vascular transport data analysis

We extracted the mean fluorescent intensity across all pixels in the perfusion timelapse video, at each time frame for each ROI. Then, we normalized the mean fluorescent intensity curve of each ROI to that of the ROI containing the mean intensity curve with the highest peak, also called the maximum mean intensity. Multiple replicates for each ROI are combined to produce a final normalized mean intensity (solid line) and the respective standard error of the mean (shaded areas). The duration of dye intensity greater than 50% of the normalized maximum intensity was reported as T_{50}. The time from initial increase in pixel intensity time series to the normalized maximum intensity was calculated (T_{max}). Step bolus injections for tumor diffusion were processed in ImageJ to obtain dye intensity intratumor and normalized to baseline intensity measured within the vasculature.

Mathematical model of diffusion

Fick's second law of diffusion governs the spatiotemporal dynamics of diffusion of a particular solute through a given solvent. The law states that the time derivative of the concentration of solute at a specific location is proportional to the Laplacian of its concentration at the same position.

$$(1)\ \frac{\partial \phi}{\partial t} = D\Delta\phi$$

For a ball of radius a initially containing solute of constant concentration C_0 and bounded by a sphere perpetually maintained at constant concentration C_1, the concentration within the ball evolves, according to this law, as a function of radial distance and time:

$$(2)\ C(r,t) = C_1 + (C_1 - C_0)\frac{2a}{\pi r}\sum_{n=1}^{\infty}\frac{(-1)^n}{n} sin\,\frac{n\pi r}{a}\, exp\left(-\frac{Dn^2\pi^2 t}{a^2}\right)$$

where D is the diffusion coefficient of the solute through the solvent. By integrating this concentration over an equatorial cross section of finite thickness, we can determine the total mass of solute within this cross section as a function of time. This leads to the expression

$$(3)\ M(t) = \iiint_V C(r,t)dV$$

$$(4)\ M(t) = \iint_A C(r,t)LdA$$

$$(5)\ M(t) = \pi a^2 L[C_1 - 8(C_1 - C_0)\sum_{n\,\in\,\{2k-1\,|k\,\in\mathbb{N}\}}\frac{1}{(n\pi)^2}\, exp\,(-D(n\pi)^2 t/a^2)]$$

This last equation has a single unknown parameter, the diffusion coefficient.

In our experiments, if we assume that the intensity of the channel is directly proportional to the concentration, then we can take a unit change in intensity as our unit of concentration. It is then straightforward to compute this same quantity over a cross-section of the tumor from imaging data of the dye channel. This enables us to directly apply the previous model to the integral of the intensity of the dye channel inside the tumor.

By minimizing the squared error between the model and the dataset as a function of the diffusion coefficient, we finally recover the maximum likelihood estimate of the diffusion coefficient under the assumption of Gaussian noise.

Cell tracking for neutrophil migration

Post-processing of neutrophil migration data was performed in MATLAB2021b. Multi-channel recordings from microscopy were stabilized and single neutrophil centroids were computed per frame to obtain corresponding position and speed information. Persistence was calculated as the total displacement divided by contour length of the path. Where relevant, migration through the intravascular space was defined as movement confined within the vasculature, intra-alveolar as movement within alveolar spaces, and interstitial as those crossing between vascular and alveolar spaces. Neutrophil shape was segmented using an intensity threshold and the *regionprops* function was used to compute aspect ratio and circularity.

Statistical analyses

All experiments were performed at least twice in separate mice to generate biologically independent samples. Data are presented as mean ± standard error of the mean (S.E.M.). All statistics were calculated as a two-tailed Student's t-test to determine significance or p-values between groups of data. All p-values < 0.1 are reported on figures for the users to observe statistical trends of data. Statistical analyses were performed in MATLAB R2021b and R2022b.

Extended Data

Extended Data Movies

Movies are in the following Google Drive folder and are included in the online submission: https://drive.google.com/drive/folders/1TE0RRUuYl1keVg7bQ9KDGHC1T4BqGlYZ?usp=sharing

Extended Data Movie 1 | Functional *ex vivo* lung inside rigid polystyrene crystal ribcage

Extended Data Movie 2 | Functional *ex vivo* lung inside semi-deformable PDMS crystal ribcage

Extended Data Movie 3 | Imaging functional lung at different ventilation rates with laser scanning confocal microscope

Extended Data Movie 4 | Imaging functional lung at different scales with laser scanning confocal microscope

Extended Data Movie 5 | Crystal ribcage provides stable imaging surface for ventilated lung

Extended Data Movie 6 | Immune cell migration in functional alveoli imaged in real-time through crystal ribcage

Extended Data Movie 7 | Apex to base image of lung with several metastatic tumors at alveolar resolution using OCT through crystal ribcage

Extended Data Movie 8 | Metastatic cancer cells remodel capillary function

Extended Data Movie 9 | Real-time imaging of vascular transport at alveolar resolution in health and disease using crystal ribcage

Extended Data Movie 10 | Neutrophil migration speed increases with higher vascular pressure

Extended Data Movie 11 | Neutrophil extravasation and migration imaged through crystal ribcage

Extended Data Movie 12 | Air and perfusate leak from site of local excision in the lung

Extended Data Movie 13 | Disrupted capillary flow in locally cauterized lung imaged through the crystal ribcage.

Extended Data Movie 14 | Local agarose blockage in the alveoli disrupts surrounding vascular dynamics

Extended Data Movie 15 | Real-time imaging of spontaneous heart atrial pulsation in response to elevated pressure

Extended Data Figures

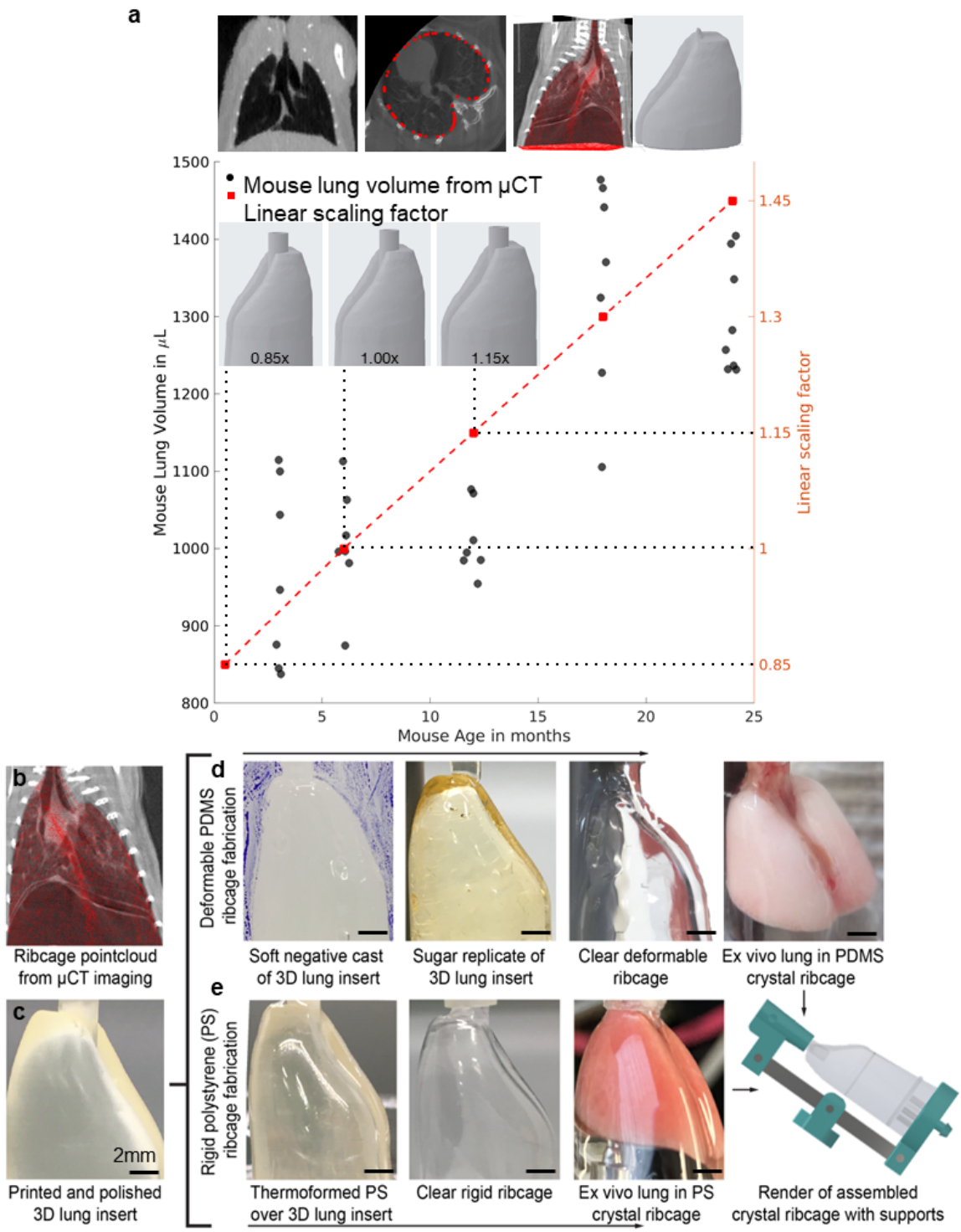

Extended Data Figure 1 | Mouse strain specific µCT informed 3D molds scaled by age and fabrication of crystal ribcages. (a) Recreating mouse ribcage geometry from µCT data, here shown for C57/B6 mice. Top: Sagittal view of mouse chest with fully inflated lung (dark region), distribution of axial control points to recapitulate ribcage cross-section and comparison of reconstructed geometry overlaid on sagittal and coronal µCT slices. Lung volume variation with

age was normalized against the mean volume at 3 months to construct a linear fit for scaling 3D lung inserts by age. (**b-e**) 3D printed models were used to make both PDMS and polystyrene crystal ribcages in two independent processes.

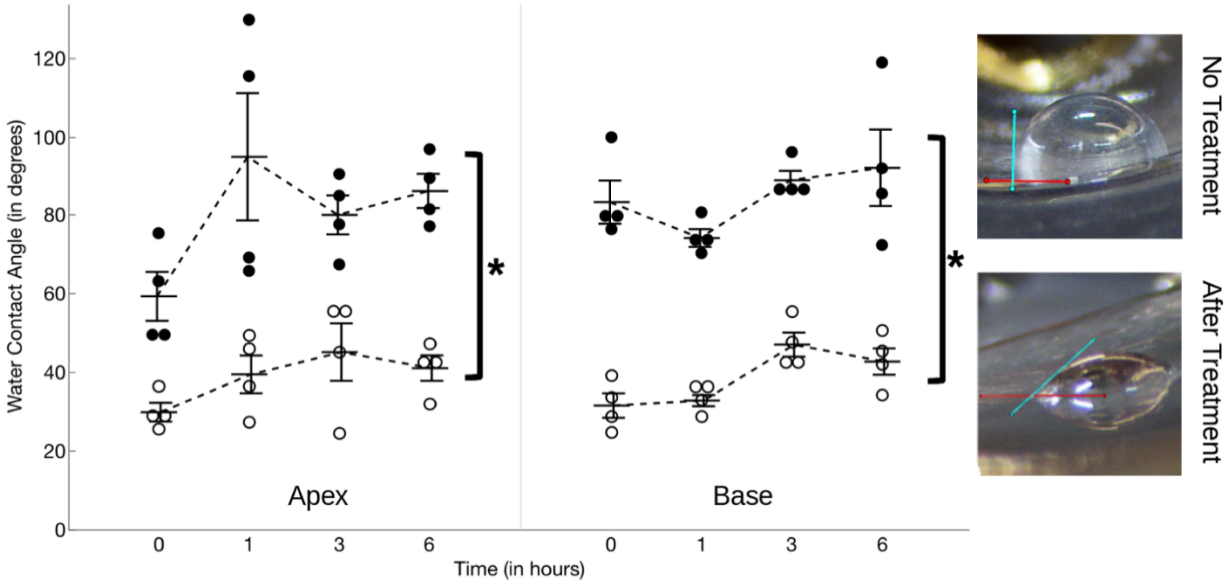

Extended Data Figure 2 | Engineered crystal ribcage surface retains hydrophilicity over entire surface for up to 6 hours. Hydrophilicity measured by the water contact angle of a droplet on a treated vs non-treated crystal ribcage surface. Smaller water contact angles are indicative of a hydrophilic surface. The scatter of the data is presented along with the mean ± S.E.M. traces. Comparison between groups performed with two-tailed Student's t-test for significance < 0.05.

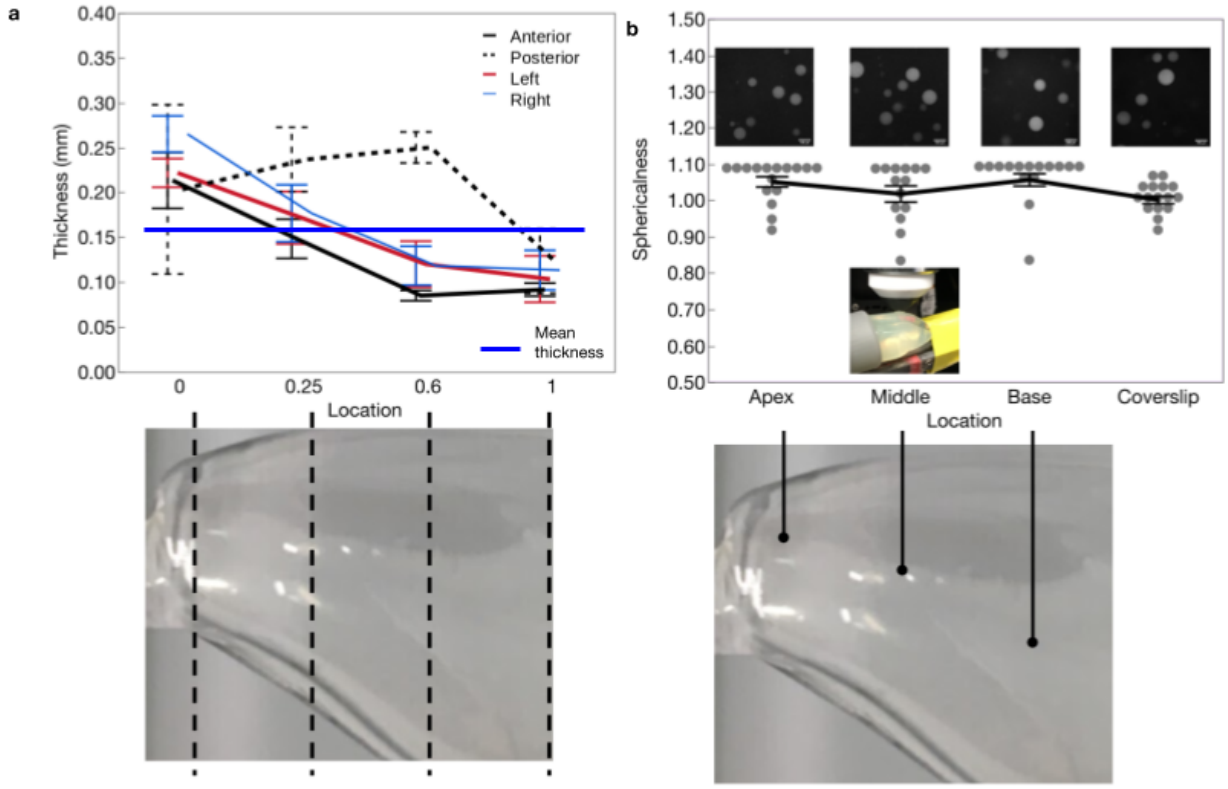

Extended Data Figure 3 | Crystal ribcage has little variation in thickness across its geometry (a) and presents no significant optical aberration over the surface when compared against a coverslip (b). Green-fluorescent polyacrylamide beads with diameters ranging from 40-100 µm were mixed with agarose to make a slurry and uniformly spread over the surface. The beads were imaged using 2-photon microscopy. The data is presented as the mean ± S.E.M. traces. Comparison between groups performed with two-tailed Student's t-test for significance < 0.05.

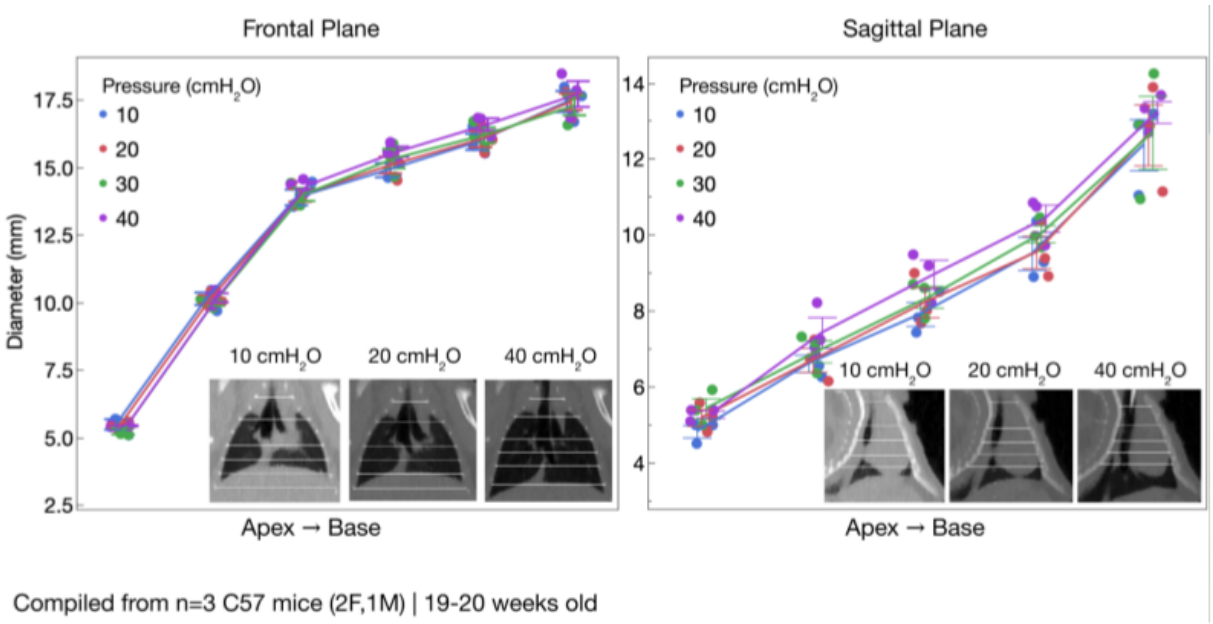

Extended Data Figure 4 | Native mouse ribcage does not show significant variation in diameter with changing PEEP across its anatomy. Previous µCT data used to define the mouse chest cavity was also used to quantify the expansion of the native mouse ribcage as a function of pressure and anatomical location during *in situ* ventilation. There was no significant difference between the ribcage diameter at tracheal pressures ranging from 10 cmH_2O to 40 cmH_2O in both the frontal and sagittal planes from the apex to the base of the ribcage. The increase in volume with increasing pressure was accommodated by the increasing length of the lung and not the width of the ribcage. This confirms that there was little contribution of the changing ribcage diameter to lung volume change during normal physiological conditions *in situ*. The scatter of the data is presented along with the mean ± S.E.M. traces. Comparison between groups performed with two-tailed Student's t-test for significance < 0.05.

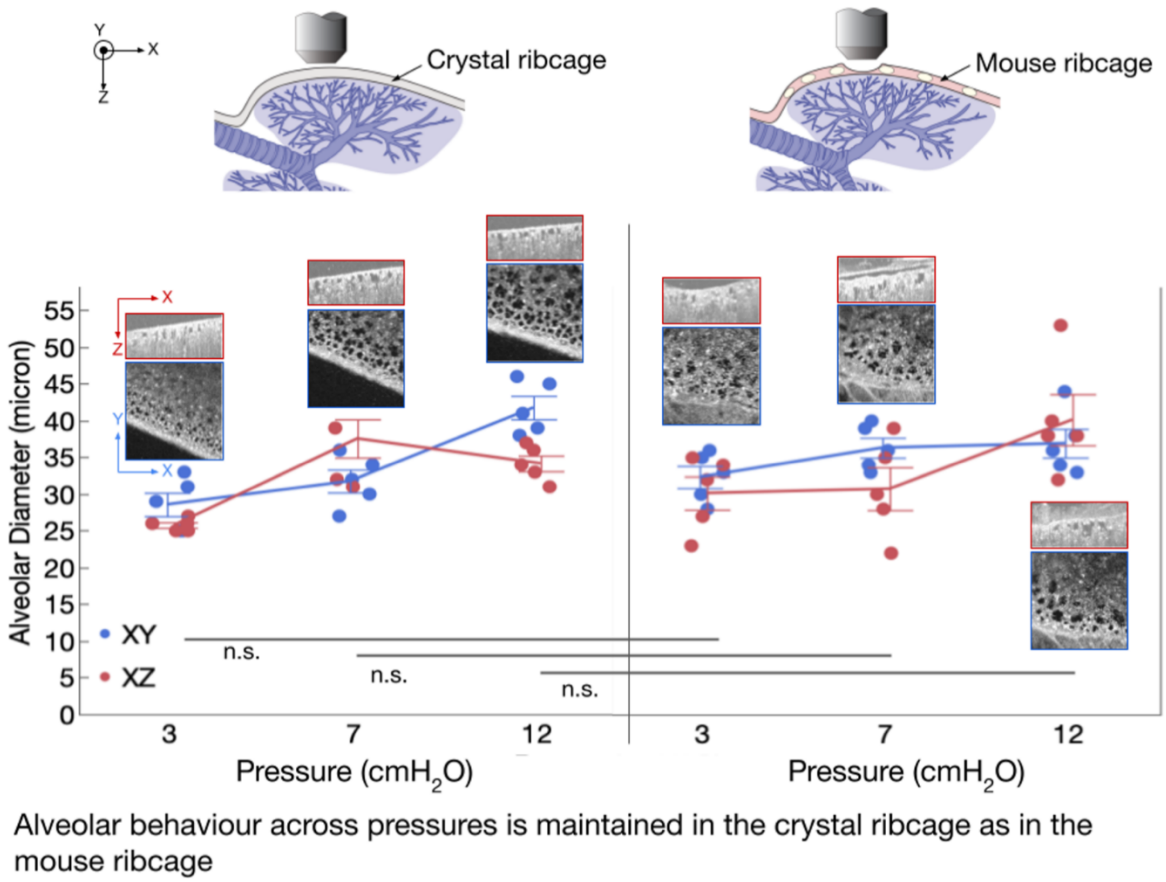

Extended Data Figure 5 | Alveolar function (diameter in µm) remains unchanged between crystal ribcage and mouse ribcage. A mouse ribcage was thinned down to make a window above the pleural sheath to image the functional lung using OCT, the same lung was then measured in the crystal ribcage for the same changes in pressure. There was no significant difference between alveoli function (measured as changing diameter) across the pressure range. The scatter of the data is presented along with the mean ± S.E.M. traces. Comparison between groups performed with two-tailed Student's t-test for significance < 0.05.

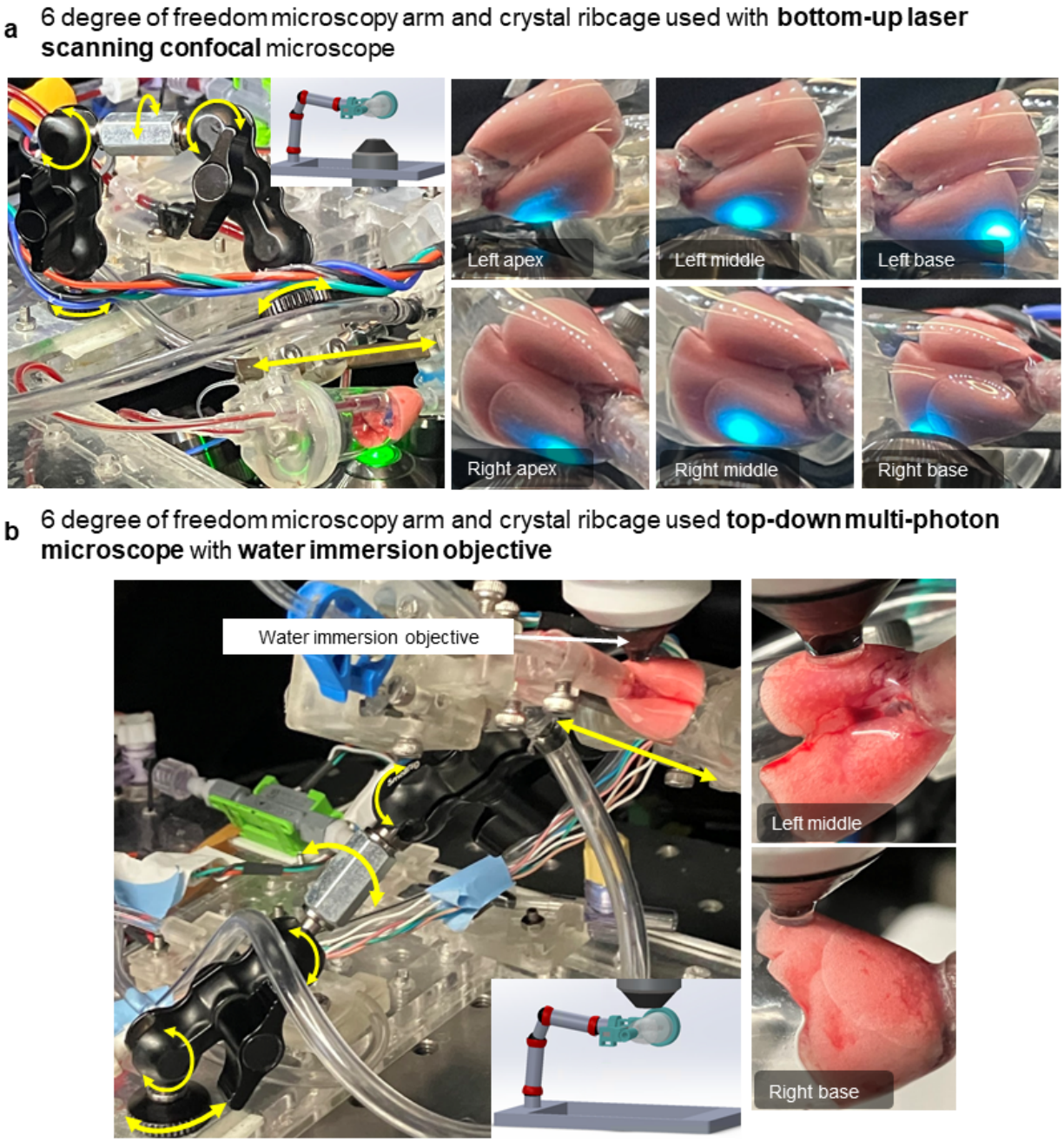

Extended Data Figure 6 | Experimental setup and 3D renders of the microscopy arms used to image different orientations of the crystal ribcage with upright and inverted microscope configurations. We successfully used the stage to image (**a**) with an inverted Olympus Fluoview 3000 laser scanning confocal microscope and (**b**) with upright microscopes like the ThorLabs optical coherence tomography probe and Bruker multi-photon microscope. The crystal ribcage is compatible with both air and water-immersion objective in both configurations.

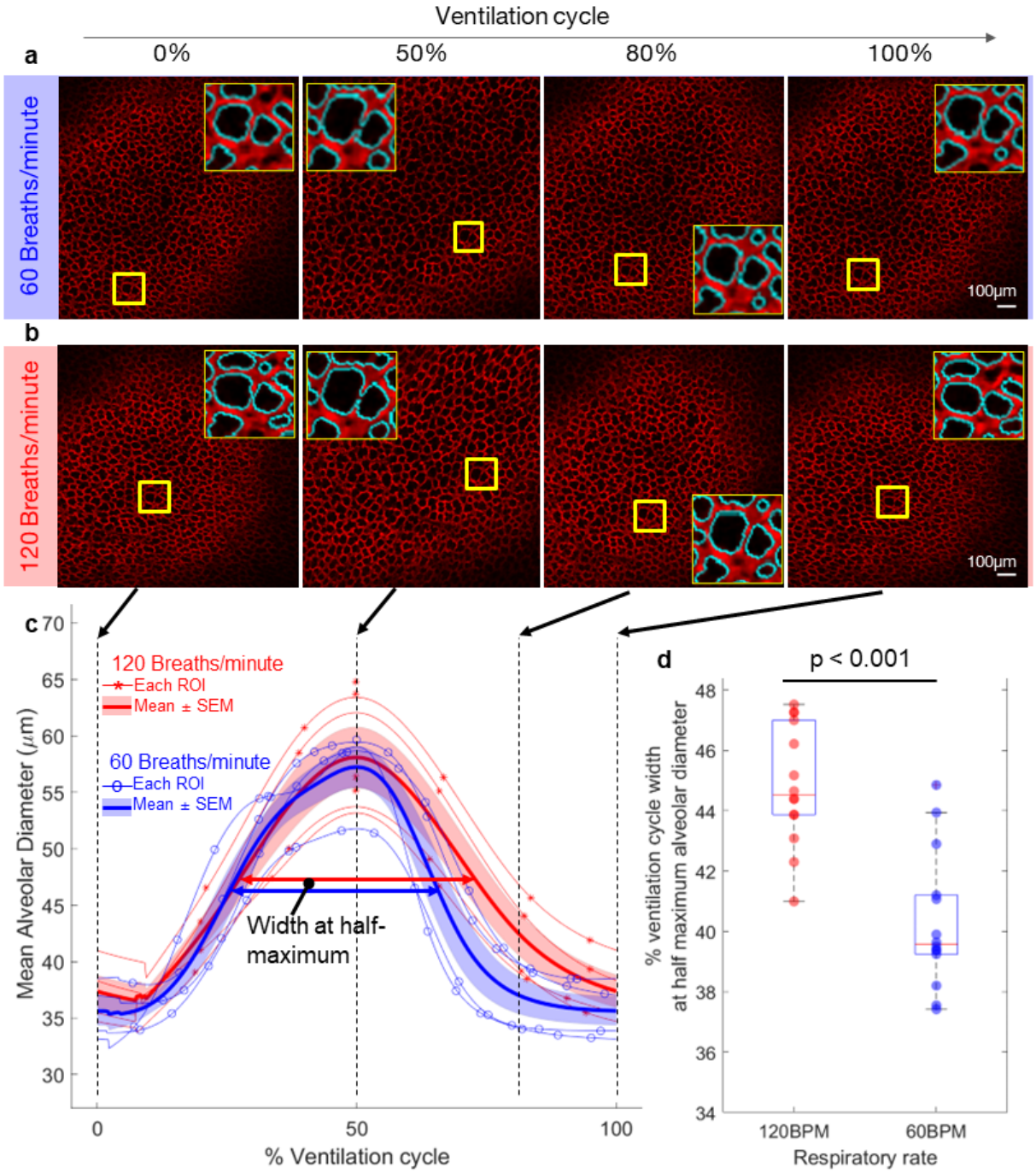

Extended Data Figure 7 | Dynamic ventilation of mouse lung shows alveoli remain at a larger diameter for longer duration at higher ventilation rate. Comparing the same region of the lungs ventilated at (**a**) 60 breaths/minute with (**b**) 120 breaths/minute by (**c**) the mean ± SEM alveolar diameter over m=4 ROI from n=2 mice with a normalized ventilation cycle. Blue traces in the inset images show the segmentation boundary drawn to quantify single alveoli. (**d**) The width of the normalized ventilation cycle is statistically larger ($p<0.05$, one sided t-test) at higher respiratory rate. Boxplots present median with 25th and 75th percentiles, whiskers are the maximum and minimum data points not considered outliers. Comparison between groups performed with two-tailed Student's t-test for significance < 0.05.

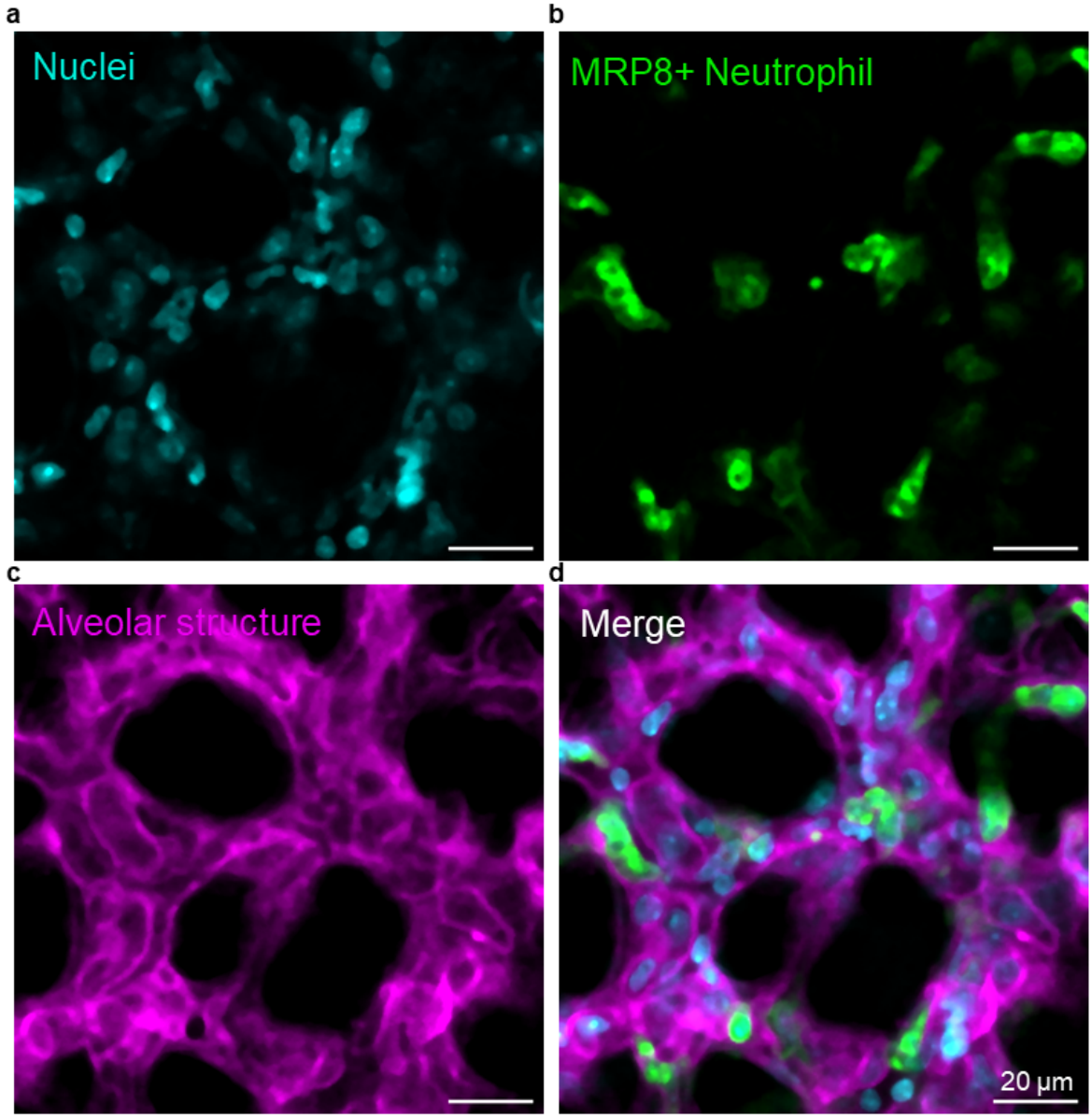

Extended Data Figure 8 | Single cell resolution imaging in the crystal ribcage at 60x magnification. (a) All cell nuclei in the lung labelled with Hoechst. (b) Neutrophils are labeled by membrane GFP through the use of mT-MRP8-mG reporter mice. (c) Functional alveoli labeled by membrane localized tdTomato+ cells through the use of mT-MRP8-mG reporter mice. (d) Merge of nuclei, neutrophil, and alveolar structural cells, imaged at 60x magnification with a water-immersion lens, on a laser scanning confocal microscope.

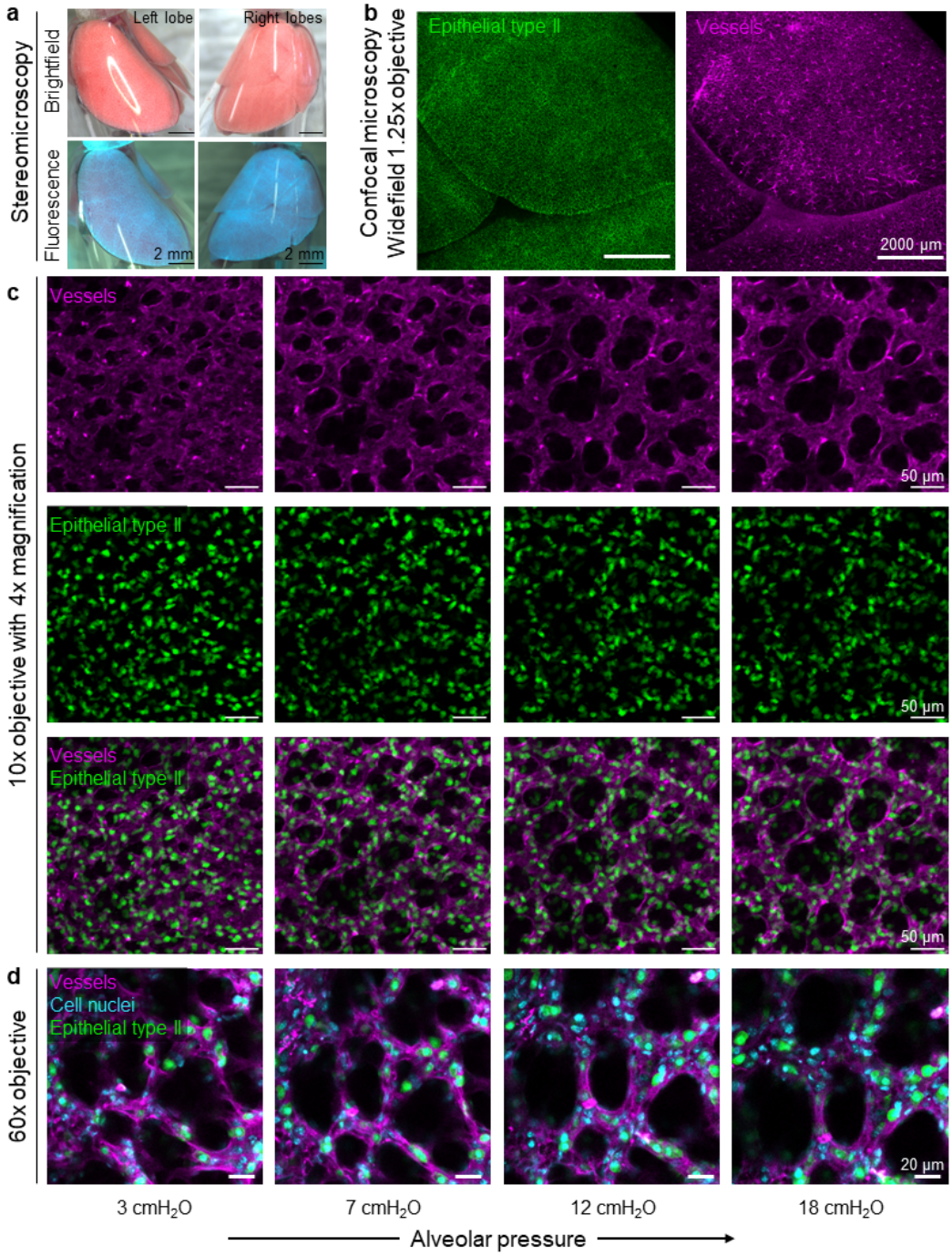

Extended Data Figure 9 | Resident alveolar type II cells, with GFP-labelled surfactant protein C (green) can be imaged inside the crystal ribcage. (a) Stereomicroscope fitted with a NightSea GFP filter to visualize the SPC-GFP distribution at the whole organ scale. (b) Confocal microscopy of the SPC-GFP population at the lobe scale on the right side of the lung at 1.25x magnification. Vessels are labeled by injection of 50 µL of 10 mg/ml Evans blue dye in saline *in vivo* prior to extraction of the lungs. (c) Confocal microscopy at the 10x magnification shows single SPC-GFP+ cells in the lung distal parenchyma. (d) Single cell nuclei and SPC-GFP signal in cell cytoplasm visible at single cell resolution using a 60x water immersion lens.

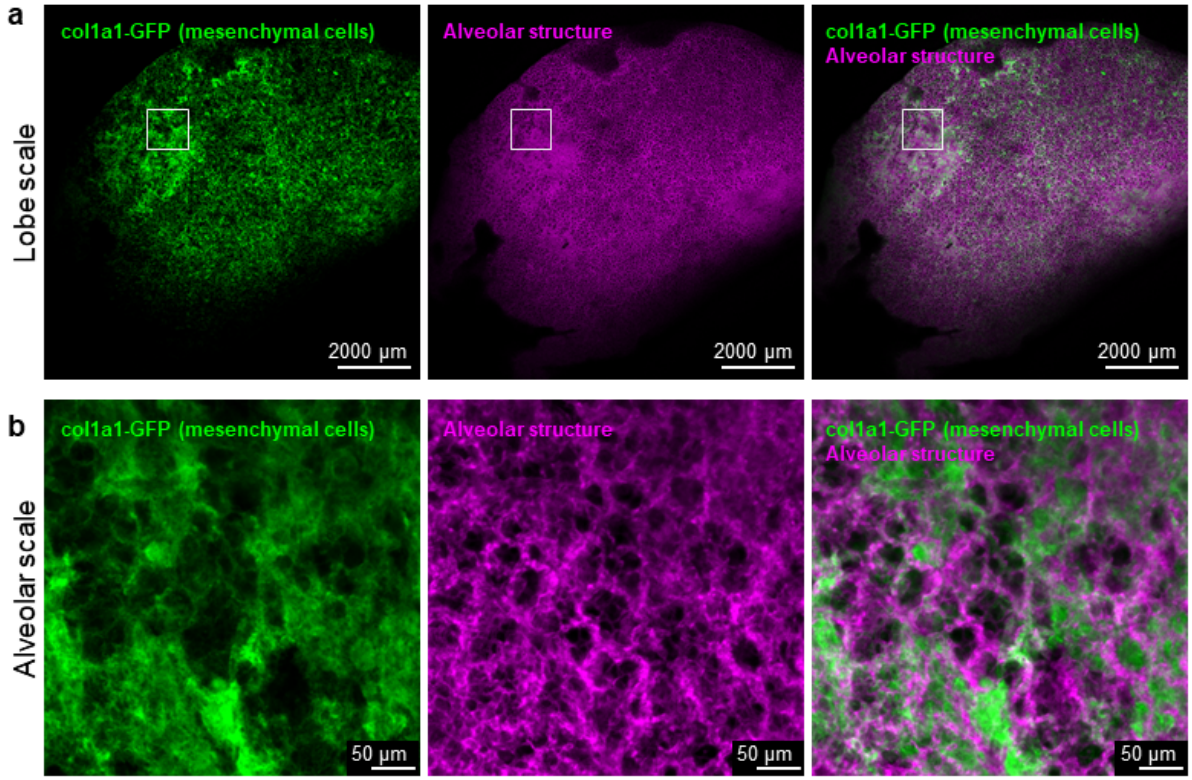

Extended Data Figure 10 | GFP fibroblasts colocalize with tdTomato lesions observed at lobe scale and then again on alveolar structure in tamoxifen treated col1a1-GFP labeled mesenchymal cells by confocal microscopy. We subsequently used the regional density in alveolar structure (membrane tdTomato) as a marker for fibrosis in mice that did not have the col1a1-GFP gene.

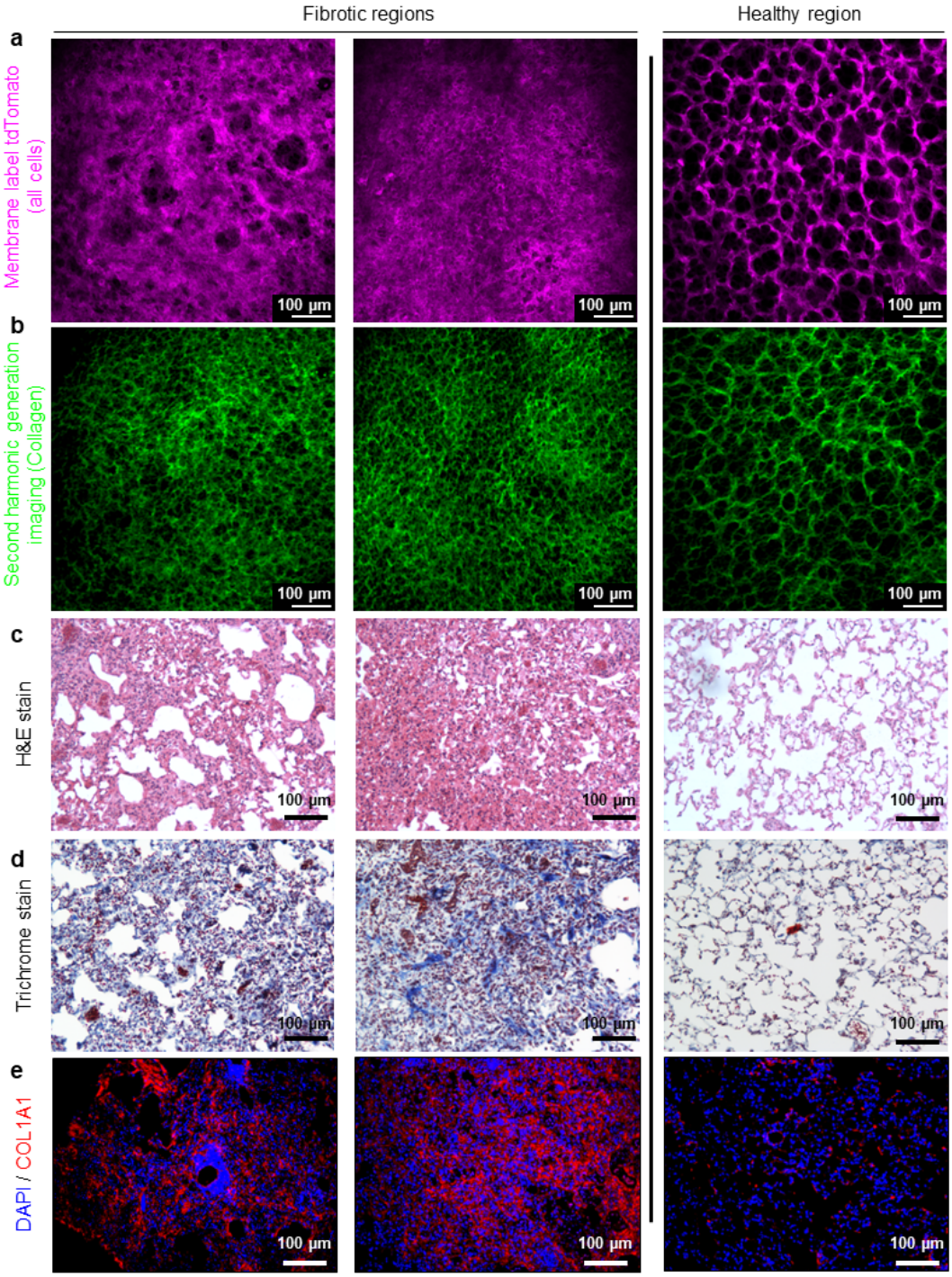

Extended Data Figure 11 | Fibrotic regions in mouse lung co-localized with increase in collagen deposition imaged using the crystal ribcage. Both fibrotic and healthy regions imaged using two-photon microscopy to image (**a**) membrane tdTomato for all cells and (**b**) second harmonic generation (SHG) signal to see associated collagen. Healthy regions in the same lung do not have increased collagen deposition. This was confirmed against (**c**) hematoxylin and eosin (H&E), (**d**) Masson's trichrome and (**e**) Collagen-I immunofluorescence staining of the same regions that were imaged with SHG signal in the fresh lung.

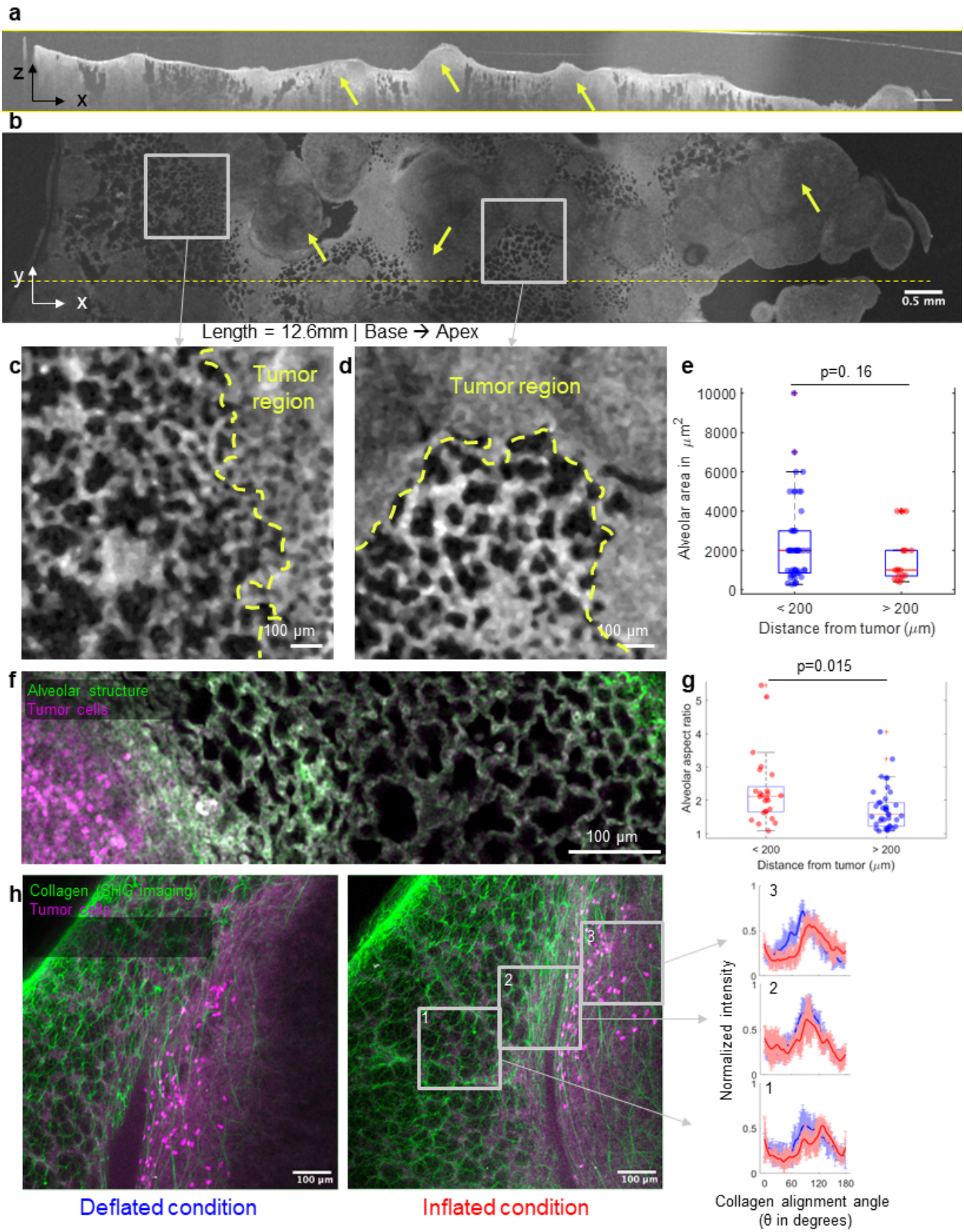
a
z
x
b
y
x
0.5 mm
Length = 12.6mm | Base → Apex
c
Tumor region
100 µm
d
Tumor region
100 µm
e
p=0. 16
Alveolar area in µm2
10000
8000
6000
4000
2000
0
< 200
> 200
Distance from tumor (µm)
f
Alveolar structure
Tumor cells
100 µm
g
p=0.015
Alveolar aspect ratio
5
4
3
2
1
< 200
> 200
Distance from tumor (µm)
h
Collagen (SHG imaging)
Tumor cells
100 µm
1
2
3
100 µm
Normalized intensity
0.5
0
0
60
120
180
Collagen alignment angle
(θ in degrees)
Deflated condition
Inflated condition

Extended Data Figure 12 | Large nodular tumors on a lung imaged through the crystal ribcage from the apex to base at alveolar resolution. (**a**) XZ- slice shows bulge of nodular tumor on the lung surface taken from the (**b**) XY- slice where the total volume was stitched together from 5 sections imaged with an OCT probe. (**c, d**) Alveoli have heterogenous deformation < 200 µm from the nodular tumors and more uniform >200 µm away. (**e**) Alveoli show more heterogeneity in area <200 µm from nodular tumor. (**f**) Another nodule imaged in the same lung with multi-photon microscopy shows (**g**) alveoli are more elliptical with greater aspect ratio closer (< 200 µm) to the nodule for n=25 alveoli <200 µm and n=38 alveoli >200 µm from tumor. (**h**) The collagen fibers adjacent to large tumors > 1mm (approximated from the arc imaged) show greater alignment when the lung is inflated. Boxplots present median with 25th and 75th percentiles, whiskers are the maximum and minimum data points not considered outliers. Comparison between groups performed with two-tailed Student's t-test for significance < 0.05.

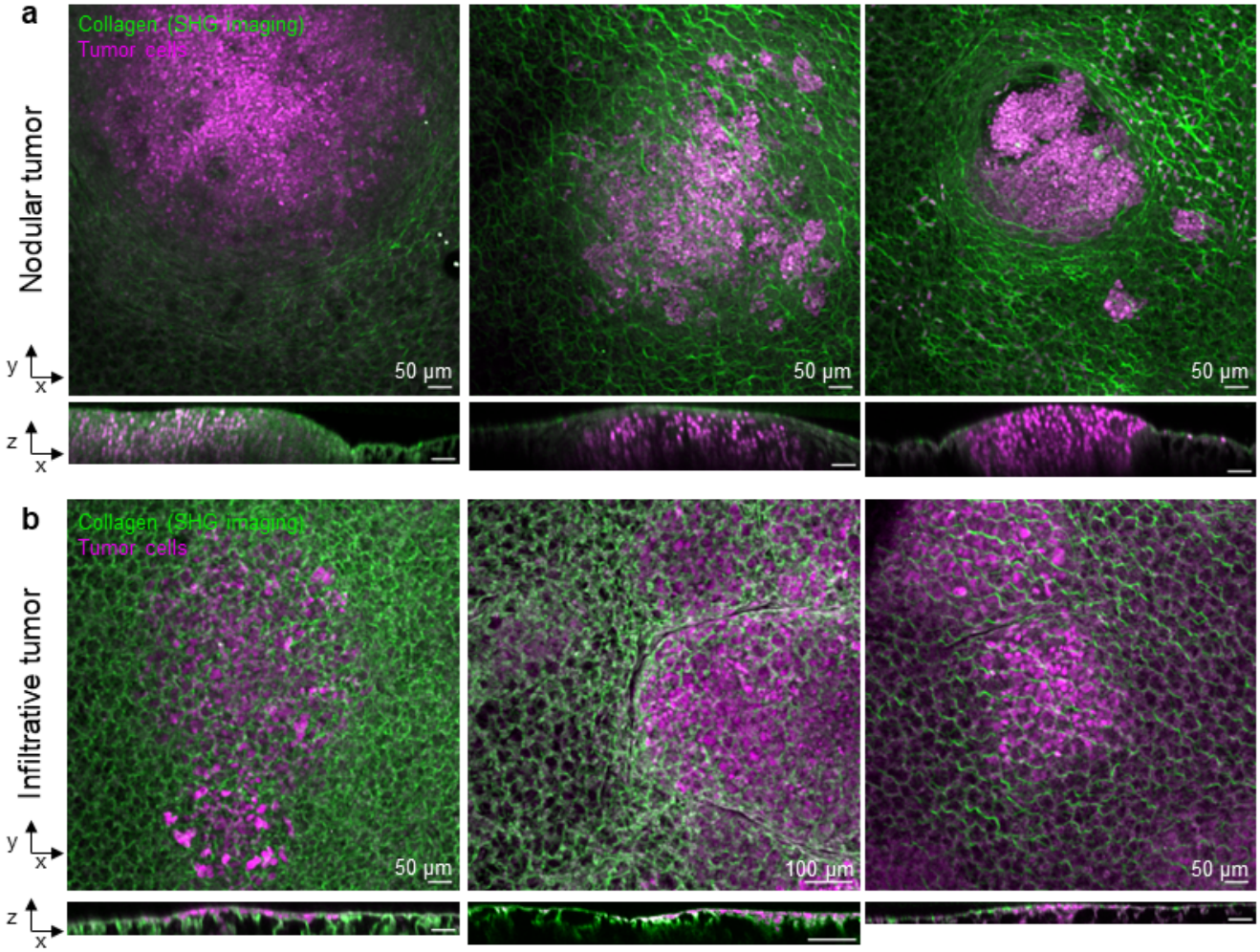

Extended Data Figure 13 | Orthogonal views comparing the spatial distribution of nodular and infiltrative tumors, for three separate instances of each phenotype. (**a**) Nodular tumors extended into the lung tissue to greater depths and bulge out of the pleural surface. (**b**) Infiltrative tumors are located more superficially on the pleural surface.

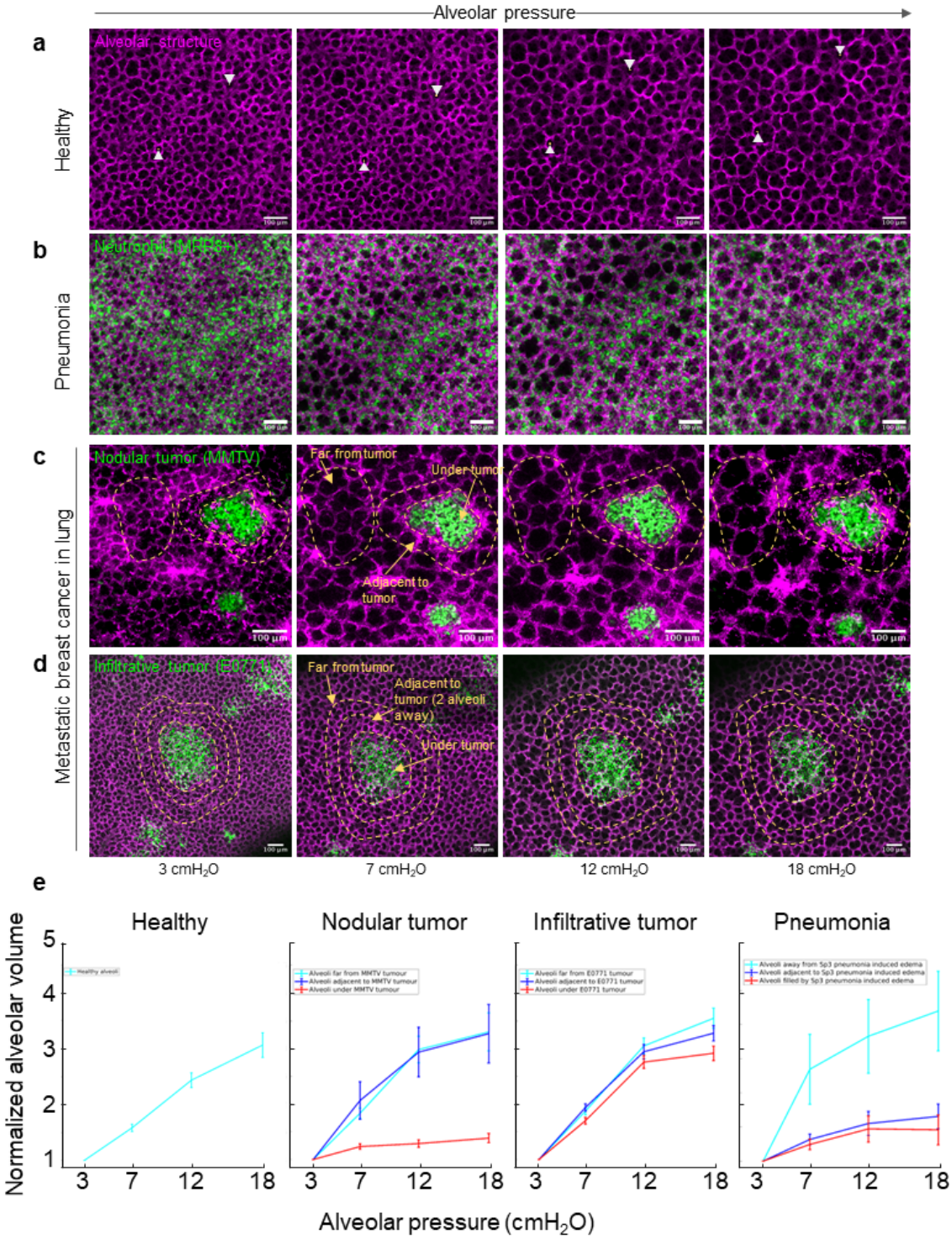

Extended Data Figure 14 | Tracking alveoli along different pressure values through the crystal ribcage. (**a**) Representative confocal microscopy images for healthy, (**b**) pneumonia, and both (**c**) nodular and (**d**) infiltrative metastatic breast cancer in lung**.** (**e**) Along with the normalized alveolar pressure-volume estimated from the alveolar diameter. n =15 alveoli quantified for each disease condition and group at each alveolar pressure and data presented as mean ± S.E.M.

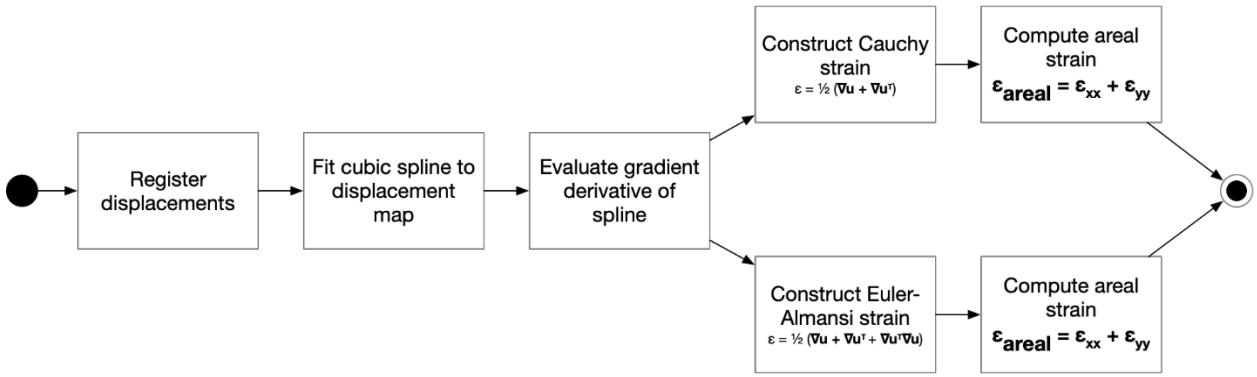

Extended Data Figure 15 | Strain computation workflow. Starting with image input to register the displacements, the displacement is smoothed by fitting a cubic spline which is subsequently evaluated to get a 3-D strain field from the image based 3-D displacement field.

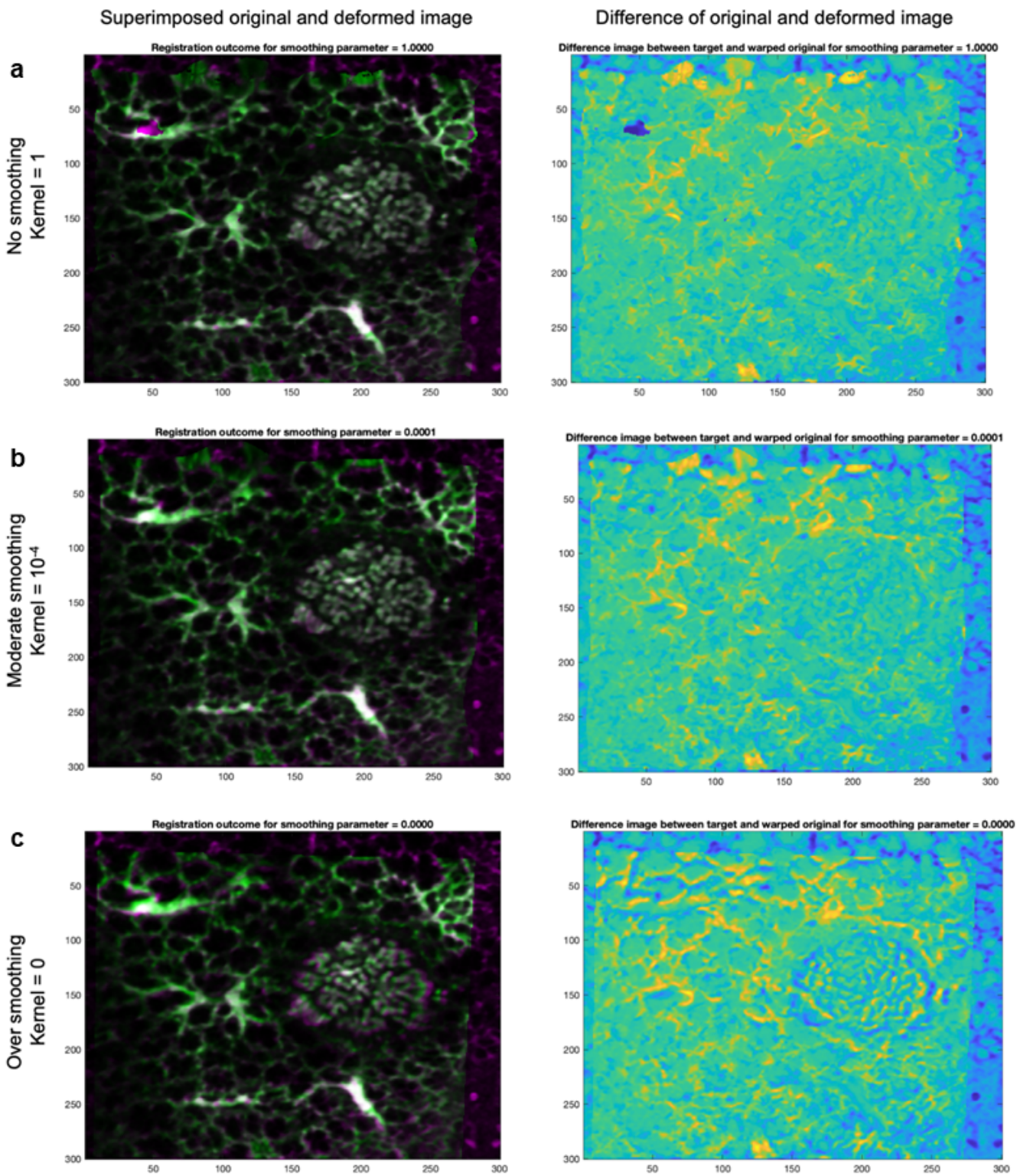

Extended Data Figure 16 | Validation of the effects of smoothing spline on registration quality, from images acquired through confocal microscopy. (**a**) Compared to the control / no smoothing condition with kernel = 1, (**b**) a kernel = 10^{-4} is a moderate smoothing kernel to preserve the registration integrity while (**c**) kernel = 0 (c) over-smooths the surface.

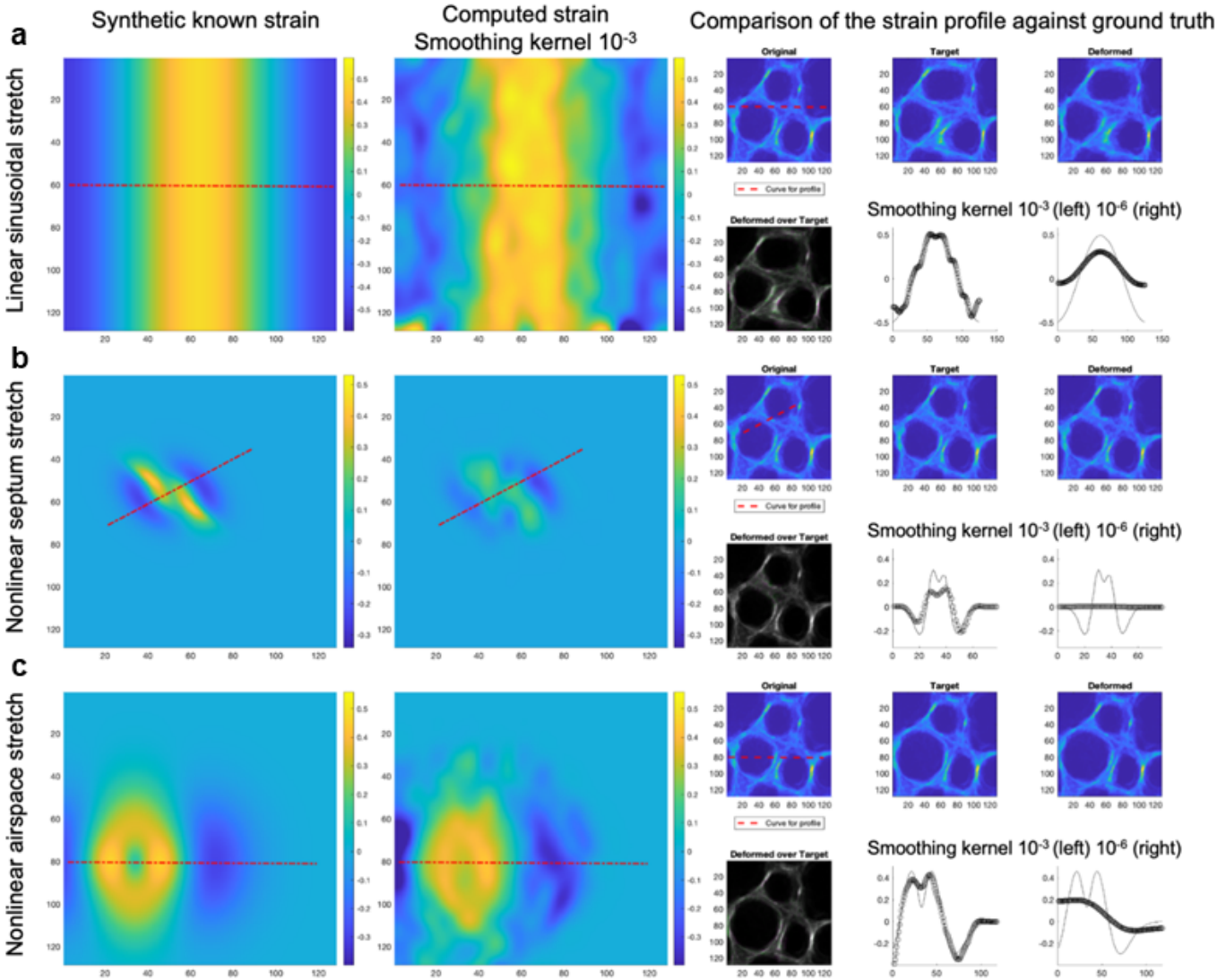

Extended Data Figure 17 | Validation of strain computation for known deformation fields, from images generated from confocal microscopy. (**a**) Computed strain was validated against known linear sinusoidal stretch, (**b**) nonlinear septum stretch, (**c**) and nonlinear airspace stretch-strain fields and shows high correspondence when smoothed with a moderate kernel, here 10^{-3}, as compared to a smaller kernel of 10^{-6} which does not capture the applied field.

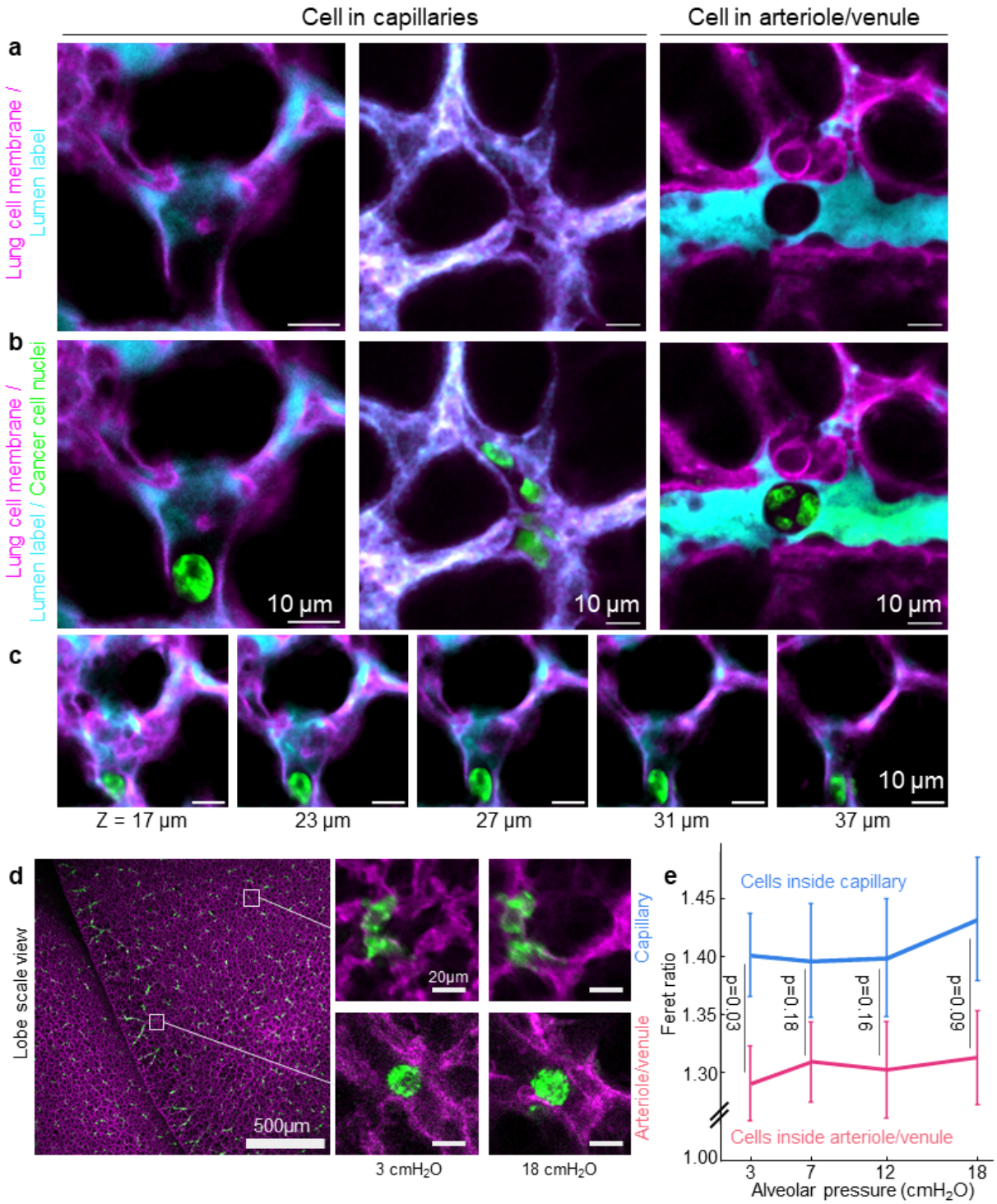

Extended Data Figure 18 | Single cell deformation in response to changing alveolar pressure. (**a**) Cell-scale confocal microscopy of the lung inside the crystal ribcage with a FITC-albumin vascular lumen label showed the shadow of the cancer cell (**b**) which was imaged in a separate channel and merged to show cancer cells stretched in capillaries compared to arterioles and venules. (**c**) XY- views of the cancer cell at different depths of confocal imaging to show the cell

is completely enclosed in the capillary. (**d, e**) Cells in capillaries quantified by the Feret ratio trended towards greater deformation in comparison to cells in larger arterioles-venules. Feret ratio quantified for n=40 cells in capillaries, n=30 cells in arteriole-venule at each alveolar pressure and data presented as mean ± S.E.M.

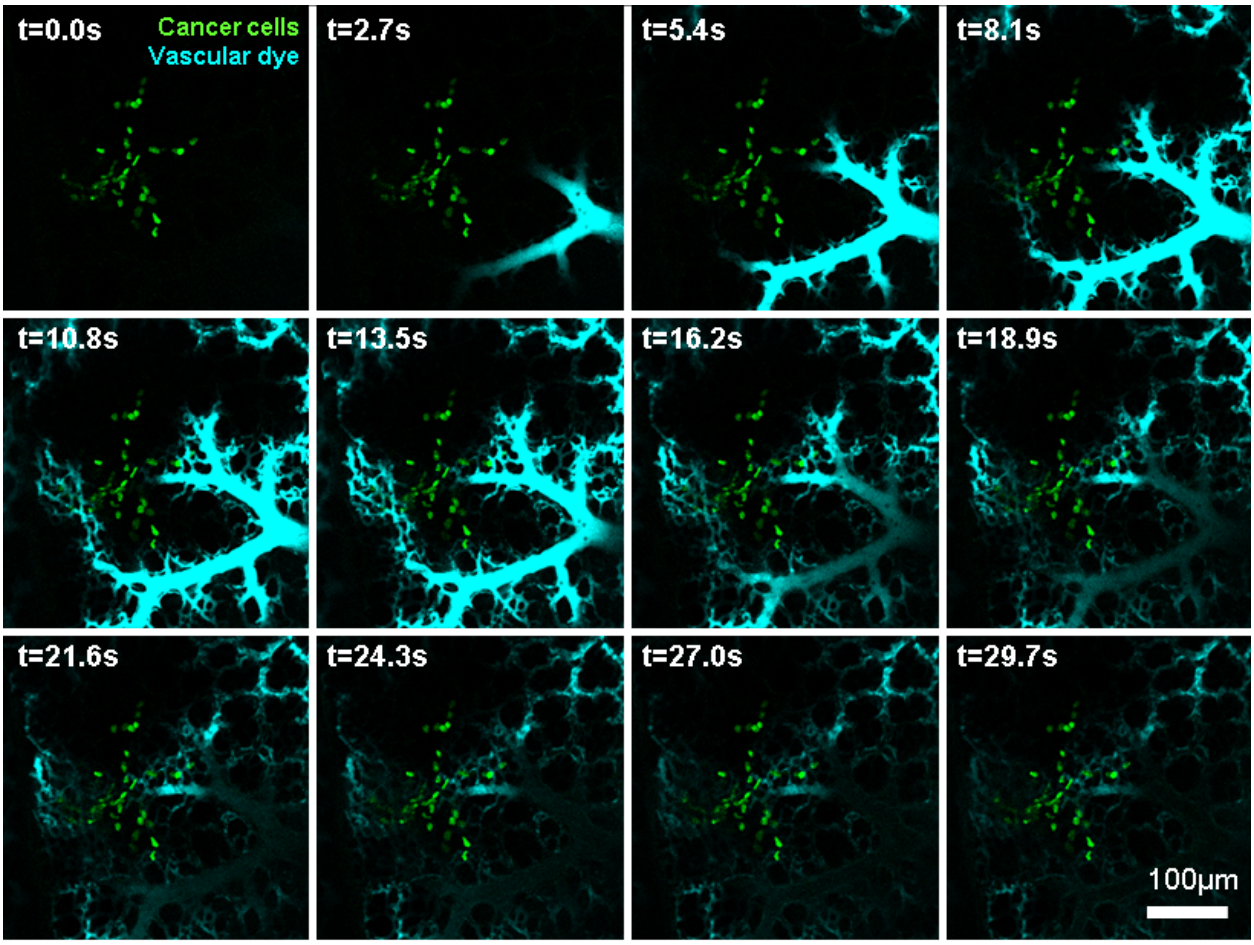

Extended Data Figure 19 | Metastatic cancer cells disrupt vascular dye distribution in capillaries. Capillary scale confocal microscopy imaging of single cancer cells that disrupt the distribution of dye observed over a time lapse imaging.

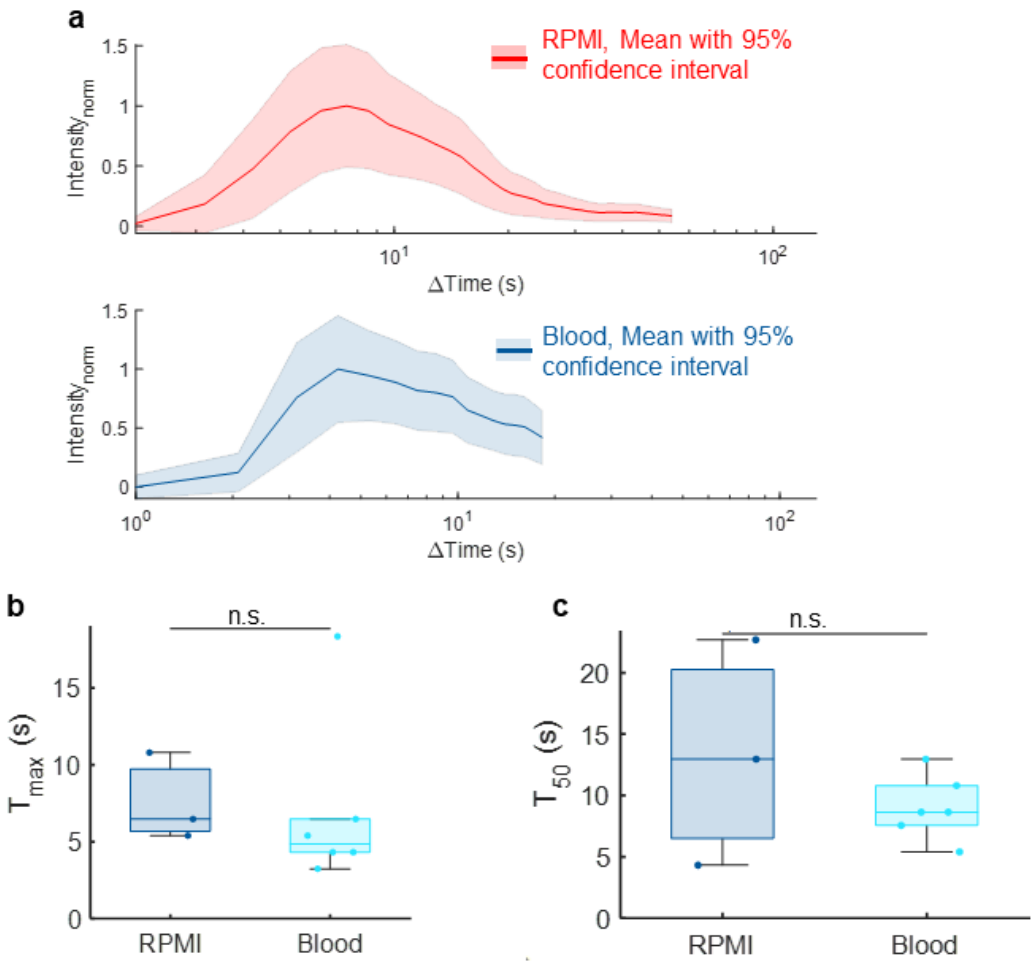

Extended Data Figure 20 | There is no significant effect of perfusate viscosity differences between RPMI media and whole mouse blood on vascular distribution of a fluorescent tracer. (**a**) The time-intensity distribution of the vascular dye in each RPMI and blood showed as the mean with the 95% confidence interval, (**b**) Comparison of the time at peak intensity. (**c**) The duration of the dye in the capillaries before clearing. Boxplots present median with 25th and 75th percentiles, whiskers are the maximum and minimum data points not considered outliers. Comparison between groups performed with two-tailed Student's t-test for significance < 0.05.

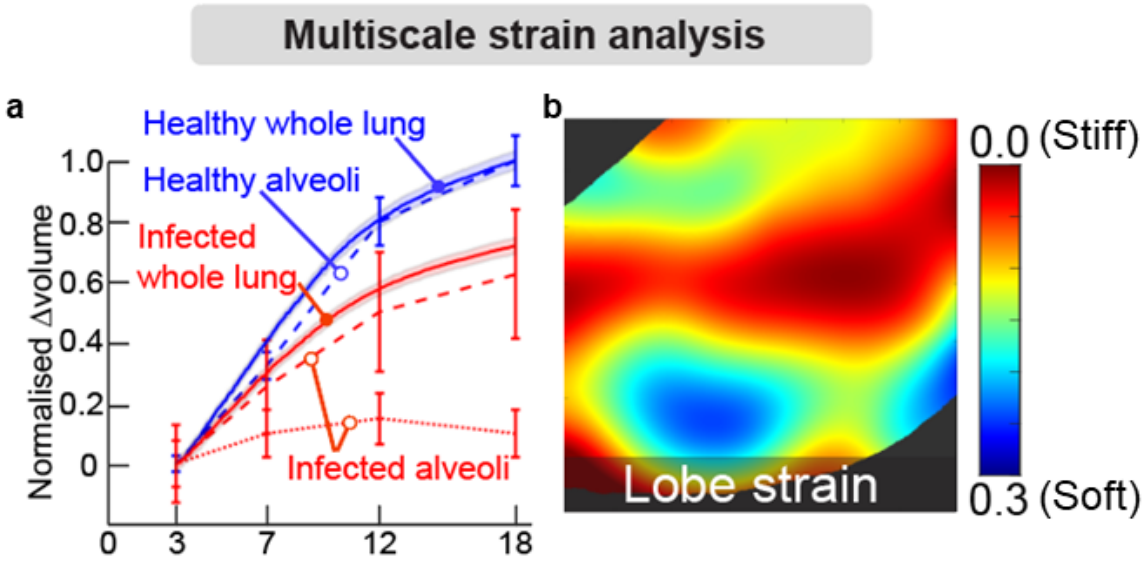

Extended Data Figure 21 | Multiscale strain analysis can be performed on the alveoli and whole lung using the crystal ribcage. (**a**) Comparing whole lung and alveolar level pressure-volume curves (mean ± SEM) for healthy and pneumonia infected regions, whole lung pressure-volume assessment of lung function under quasi-static ventilation does not account for heterogeneity in alveolar scale function and (**b**) understanding the lobe-level strain from confocal microscopy imaging.

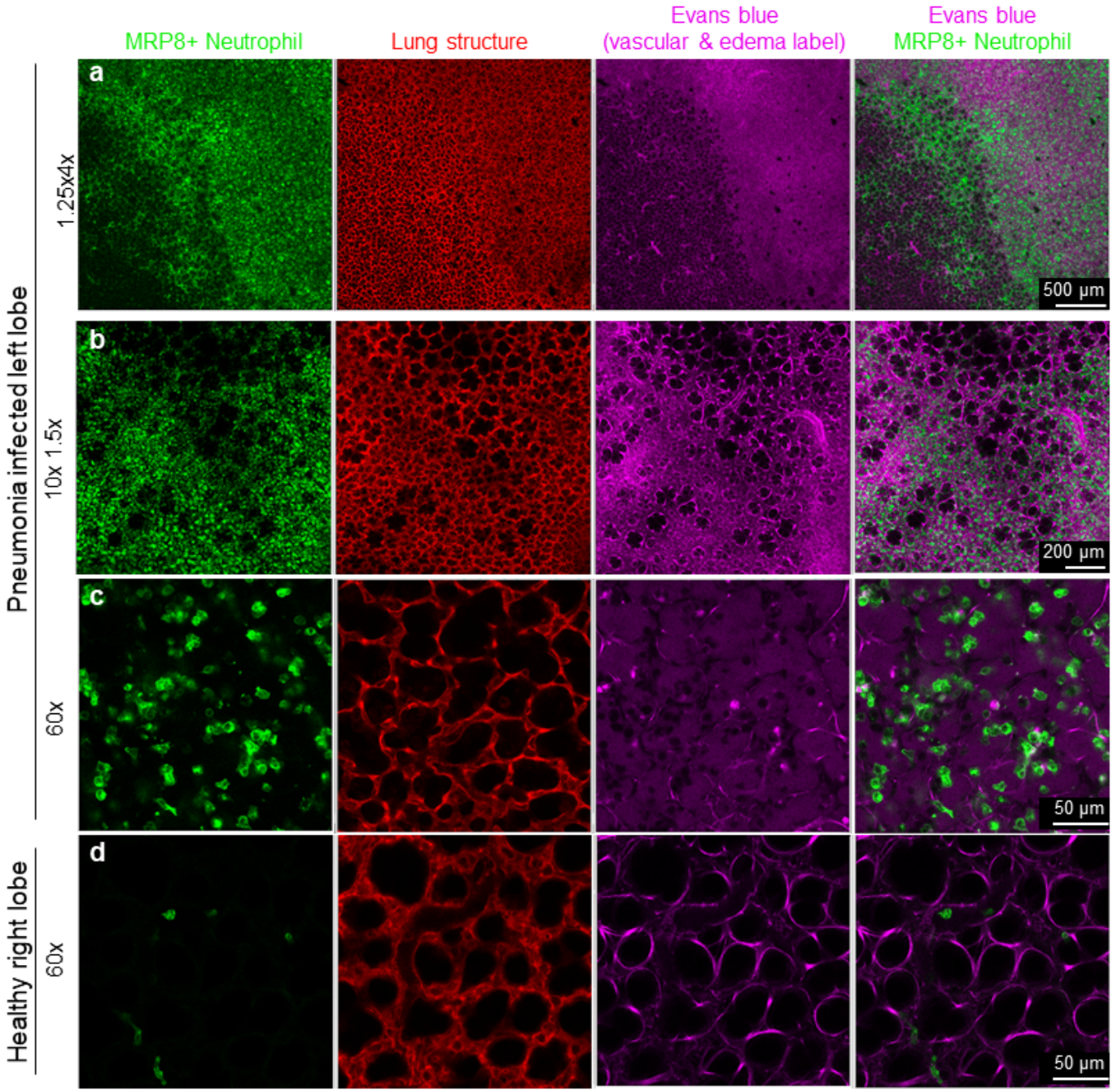

Extended Data Figure 22 | MRP8+ Neutrophil cells co-localized with edema in lungs after at 30 hours lobar pneumonia injury. Correlation of the edema label with neutrophil cells is imaged (**a**) using 1.25x, (**b**) 10x and (**c**) 60x objectives to confirm that all alveoli with neutrophils (green) are edematous (magenta). (**d**) The contralateral lobe was also imaged to show the absence of edema and neutrophils inside alveoli.

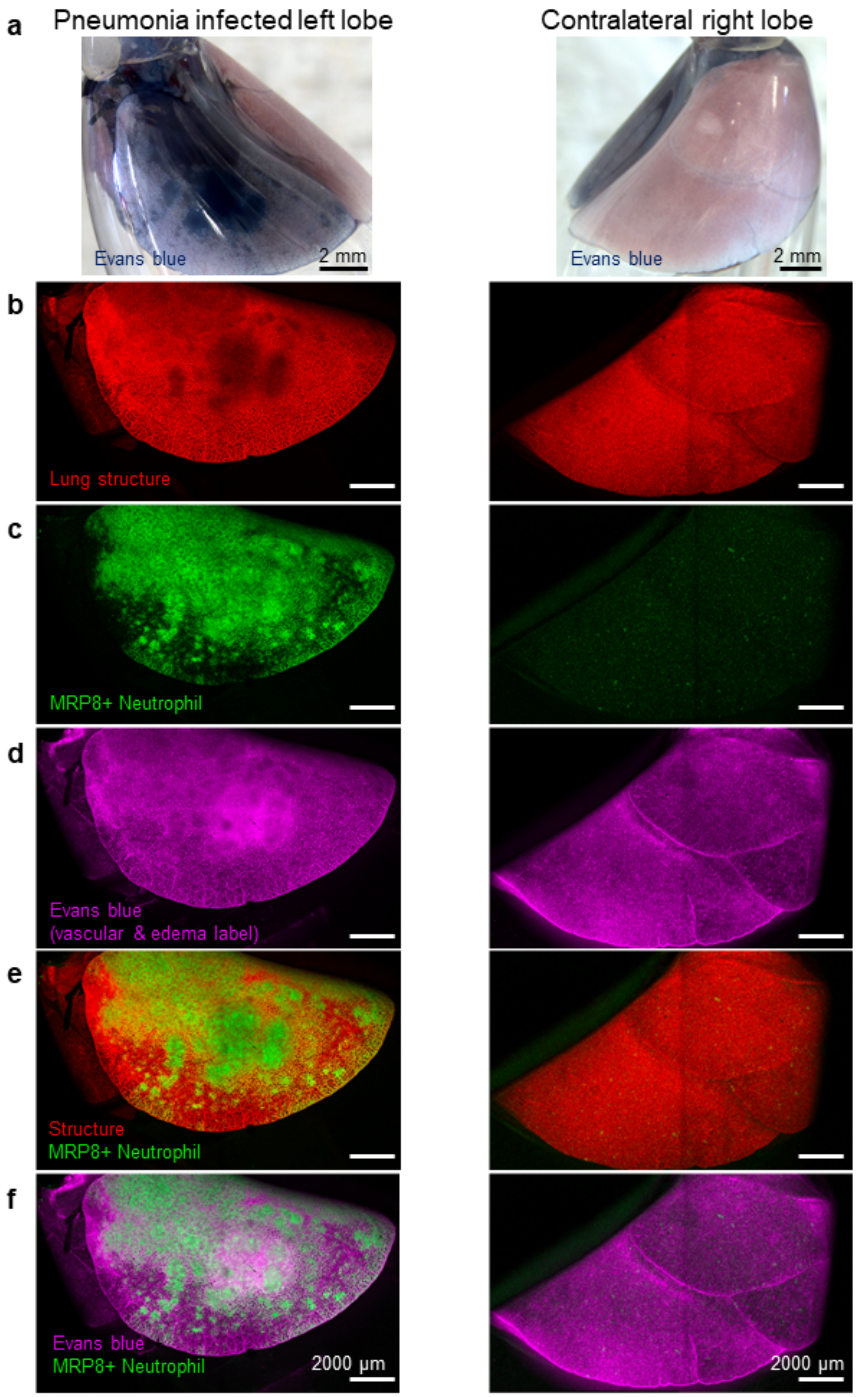

Extended Data Figure 23 | Distal lung surface can be imaged almost completely with the crystal ribcage.(**a**) At the whole lobe level, the pneumonia-infected left lobe and contralateral right lobe are imaged using a stereomicroscope, (**b**) and each separate fluorescent marker is labeled separately for each lobe using a laser scanning confocal with 1.25x objective to get the (**b**) tdTomato labelled lung structure, (**c**) MRP8+ neutrophils, (**d**) intravascular and edema label Evans blue (**e**), combined lung structure with neutrophils (**f**), and combined edema with neutrophils. Higher resolution images of a smaller region are presented in **Extended Data Fig. 22**

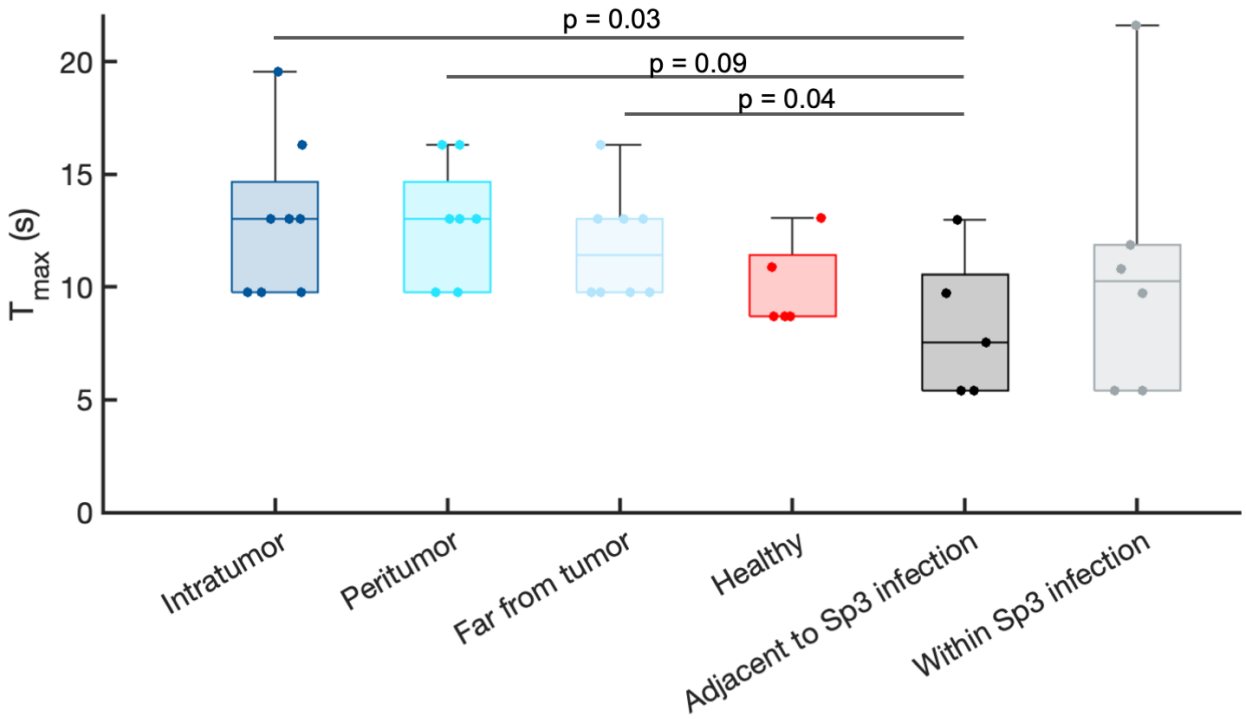

Extended Data Figure 24 | Capillary function is slowest in nodular tumor and fastest in pneumonia conditions. Time taken for dye to reach maximum intensity T_{max} is least in case of pneumonia (Sp3) infection where capillaries are leaky compared to nodular tumor cases, from imaging data acquired via confocal microscopy. Boxplots present median with 25th and 75th percentiles, whiskers are the maximum and minimum data points not considered outliers. Comparison between groups performed with two-tailed Student's t-test for significance < 0.05.

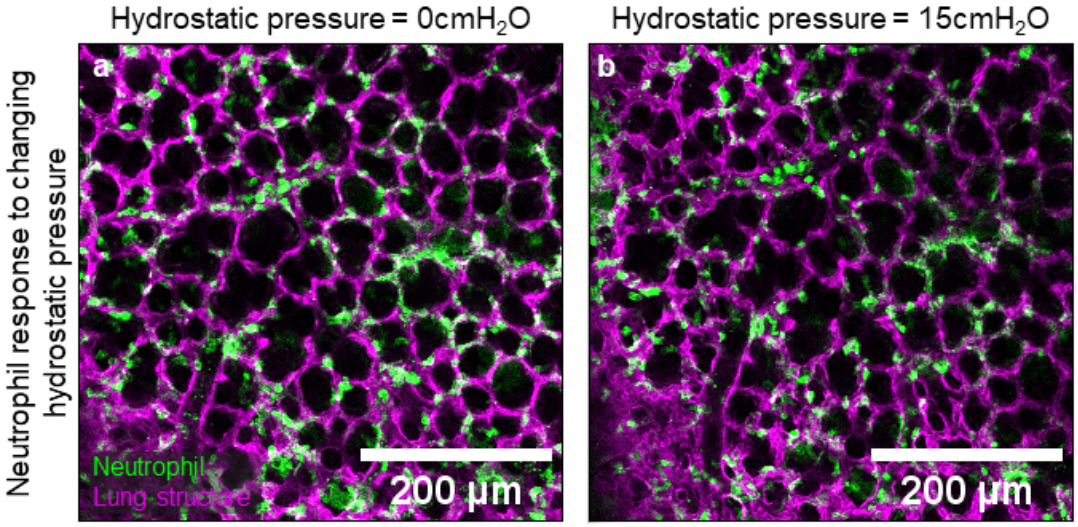

Extended Data Figure 25 | Heterogenous distribution of neutrophils (green) in an alveolar scale confocal microscopy image of LPS injured lungs. Alveolar pressure was held constant at 7 cmH_2O while hydrostatic vascular pressure was increased from (a) 0 cmH_2O to (b) 15 cmH_2O.

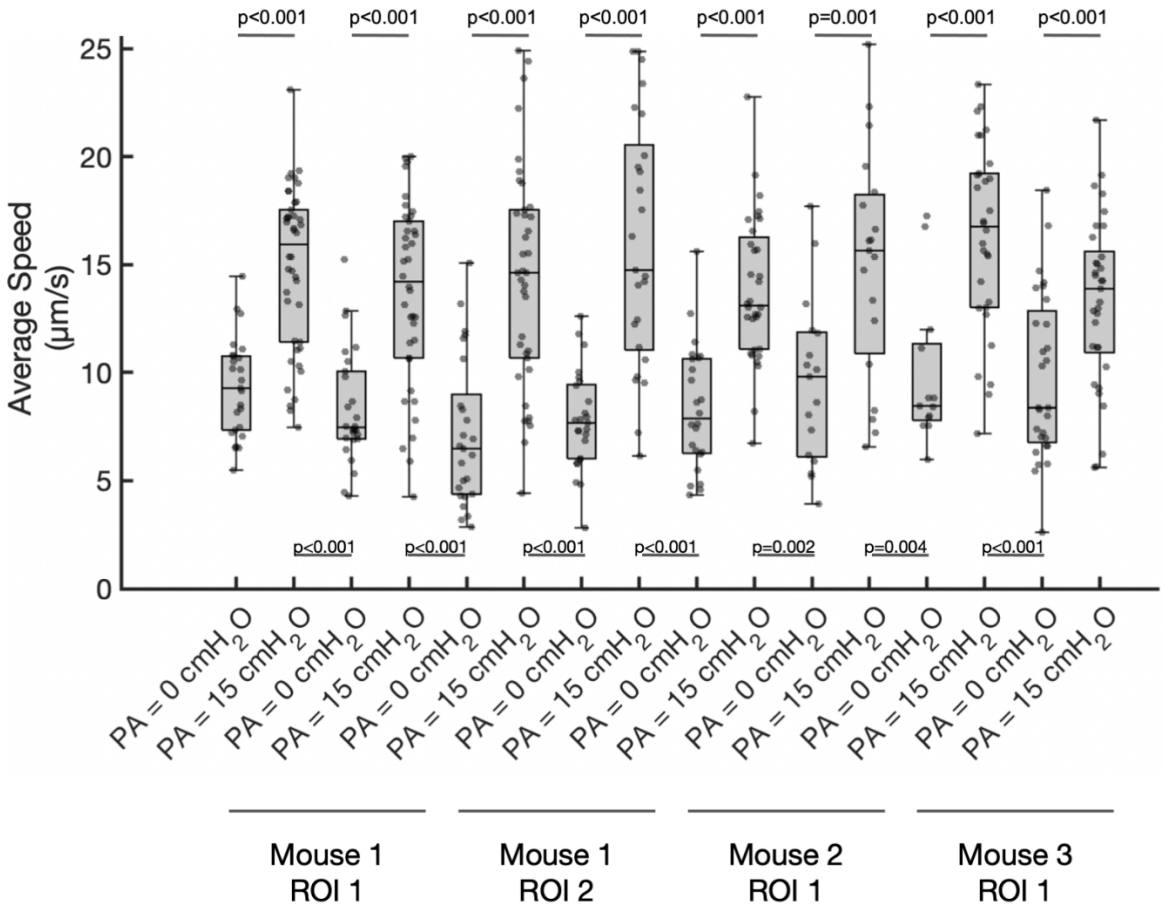

Extended Data Figure 26 | Neutrophil mechano-responsiveness demonstrated in acute lung injury (LPS). Hydrostatic pressure inside the capillaries (P_A) reversibly changed from 0 to 15 cmH_2O in m=4 ROI from n=3 mice, from confocal microscopy image data. Boxplots present median with 25th and 75th percentiles, whiskers are the maximum and minimum data points not considered outliers. Comparison between groups performed with two-tailed Student's t-test for significance < 0.05.

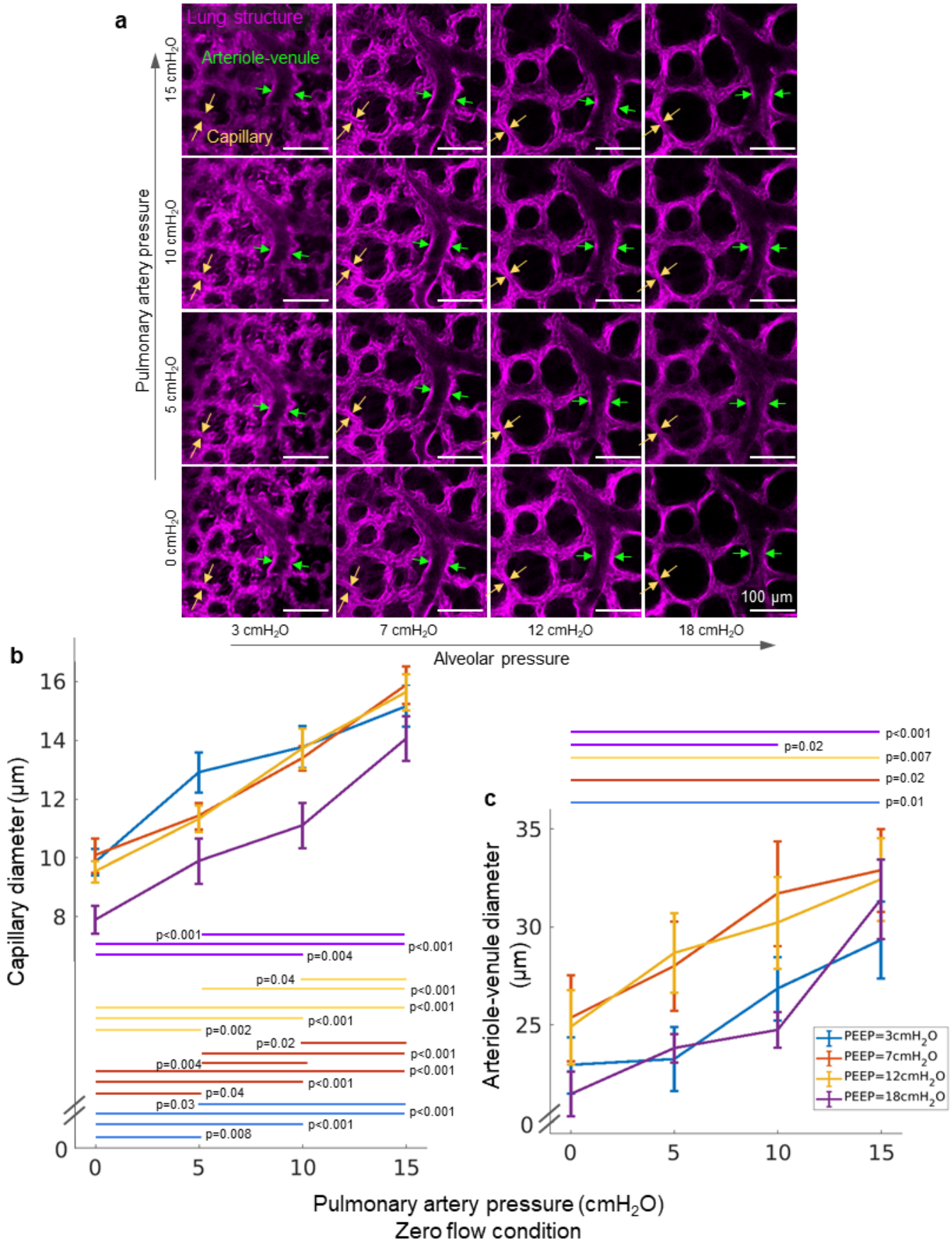
a
Lung structure
Arteriole-venule
Capillary
15 cmH2O
10 cmH2O
5 cmH2O
0 cmH2O
Pulmonary artery pressure
100 µm
3 cmH2O
7 cmH2O
12 cmH2O
18 cmH2O
Alveolar pressure
b
Capillary diameter (µm)
p<0.001
p=0.004
p=0.04
p<0.001
p<0.001
p<0.001
p=0.002
p=0.02
p<0.001
p=0.004
p<0.001
p<0.001
p=0.04
p=0.03
p<0.001
p<0.001
p=0.008
c
p<0.001
p=0.02
p=0.007
p=0.02
p=0.01
Arteriole-venule diameter (µm)
PEEP=3cmH2O
PEEP=7cmH2O
PEEP=12cmH2O
PEEP=18cmH2O
Pulmonary artery pressure (cmH2O)
Zero flow condition

Extended Data Figure 27 | Vessel distension vs vascular pressure. (**a**) Representative confocal microscopy images of arteriole-venules and capillaries imaged over the entire lung surface at different combinations of alveolar and vascular pressures. The changes in (**b**) capillary and (**c**) larger arteriole-venule diameter (reporting mean ± S.E.M. ad two-tailed t-test with alpha=0.05) with respect to pulmonary artery pressure in zero flow conditions. The vessel diameter significantly increased with increasing pressure for both micro- and medium sized vessels. However, arterioles and venules did not show a significant change in diameter when the pressure was initially increased from 0 to 5 cmH_2O across all PEEP conditions.

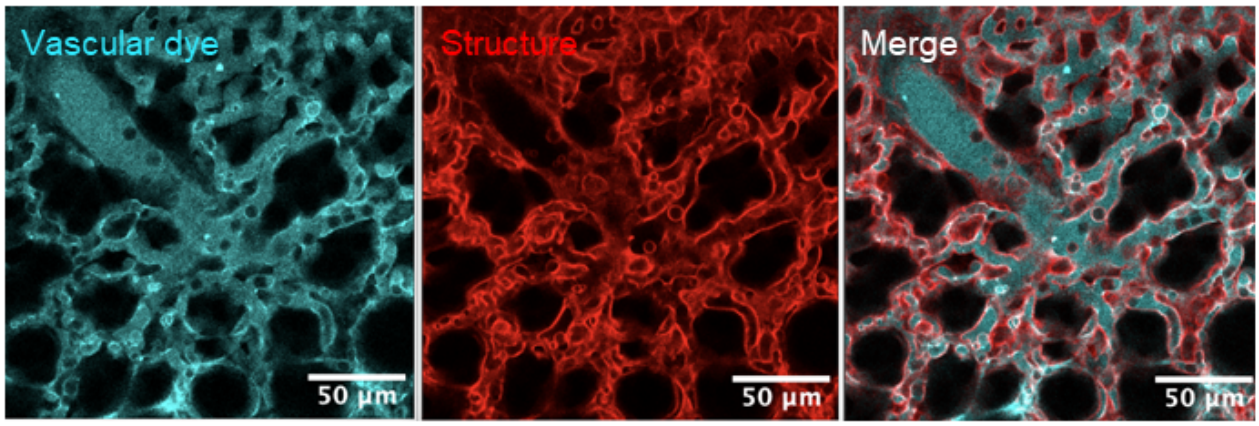

Extended Data Figure 28 | The crystal ribcage used to visualize individual lung capillary walls and perfused lumens at high magnification (60x). The lung was perfused with 50 µL of 10 mg/ml FITC-albumin dissolved in saline and injected *in vivo* through the mouse tail vein prior to excision of the lungs for high-resolution confocal microscopy.

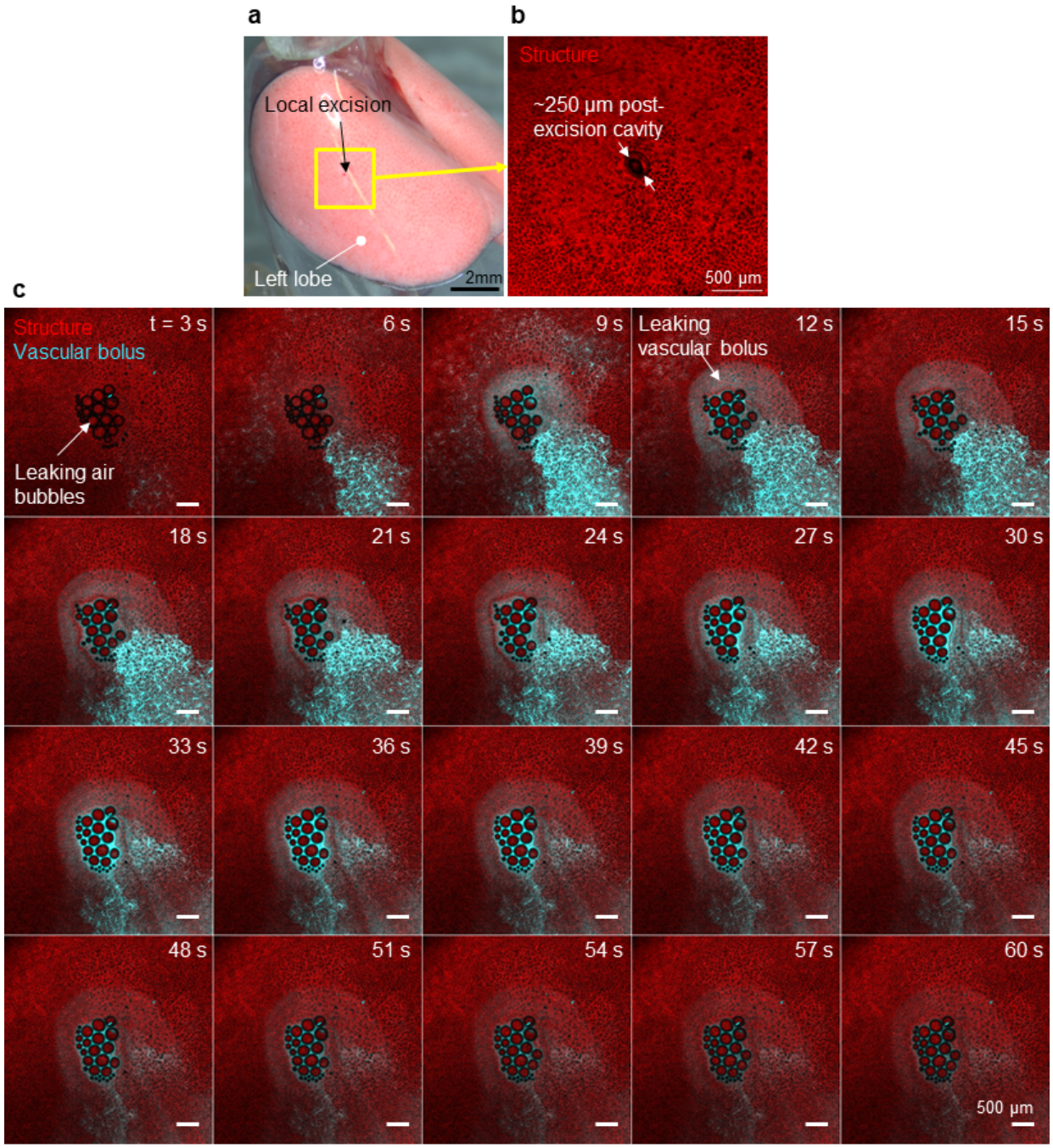

Extended Data Figure 29 | Air and vascular dye leak out of lobe at site of local excision. (**a**) Stereomicroscopy of the whole-lobe view of the lung, showing a local excision of tissue on the left lobe of a healthy mouse. (**b**) Confocal microscopy view of the excision site, where lung structure is fluorescently labeled with tdTomato through using mTmG reporter mice. (**c**) Timelapse imaging of vascular transport of a bolus of dye shows that air bubbles and dye leak out of the lung at the excision site due to the compromise of alveolar and vascular integrity.

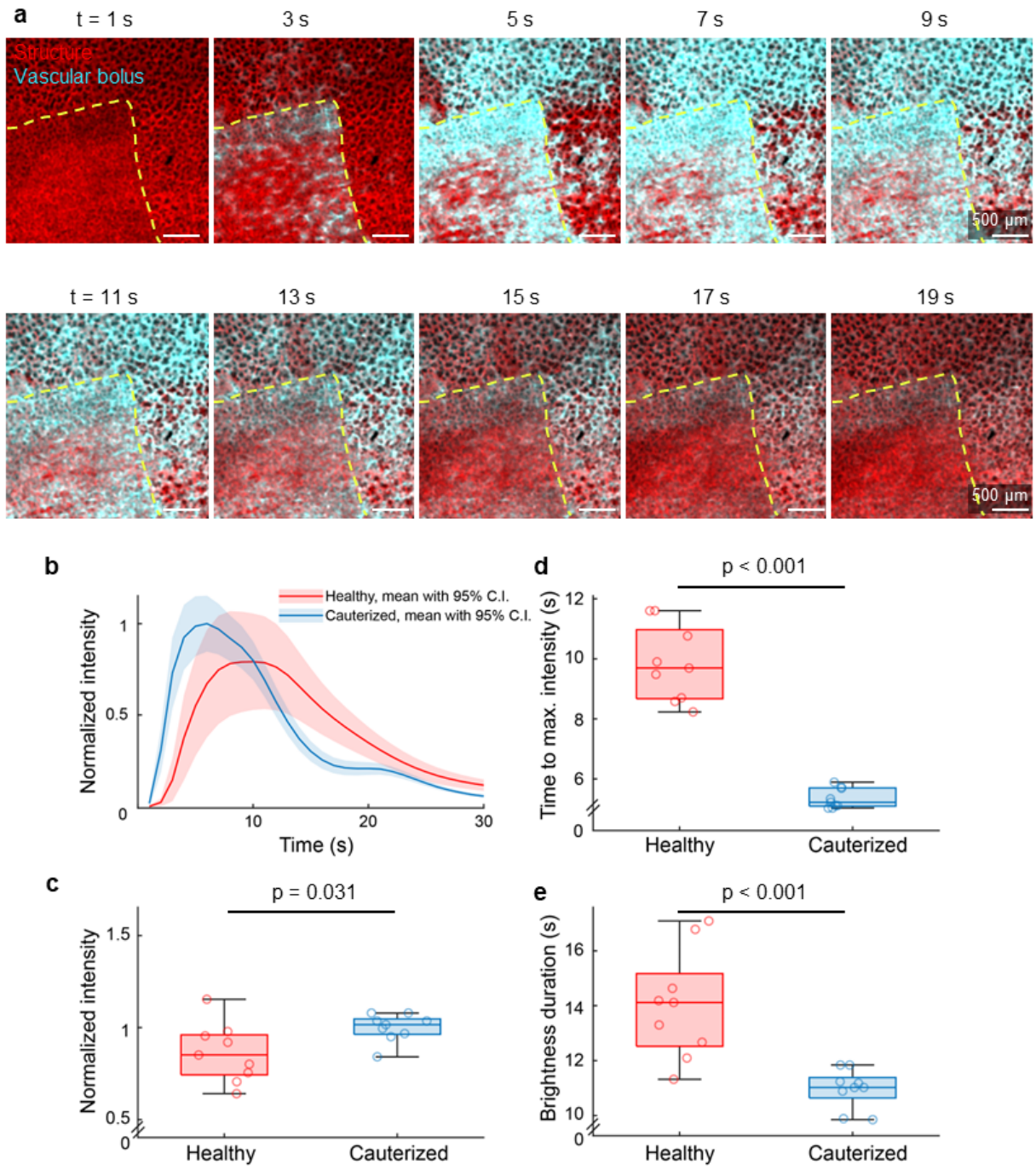

Extended Data Figure 30 | Local modulation of vascular dynamics by cauterizing the pleural lung surface. We used a laser scanning confocal (**a**) to image the arrival and clearance of vascular dye (10 mg/ml Cascade blue dextran) dissolved in RPMI delivered to the lung with a 1.25x objective in healthy and cauterized region. (**b**) The fluorescence intensity with respect to time for each healthy and cauterized area. (**c**) Comparison of the maximum fluorescence intensity within each region after delivery of the bolus. (**d**) Time to maximum intensity for each region after dye delivery. (**e**) Duration of brightness in each region. Boxplots show median of data and 25th and 75th quartiles as edges. Data outside these quartile ranges are indicated as hollow circles, quantified for m=9 ROI per condition from n=1 mouse.

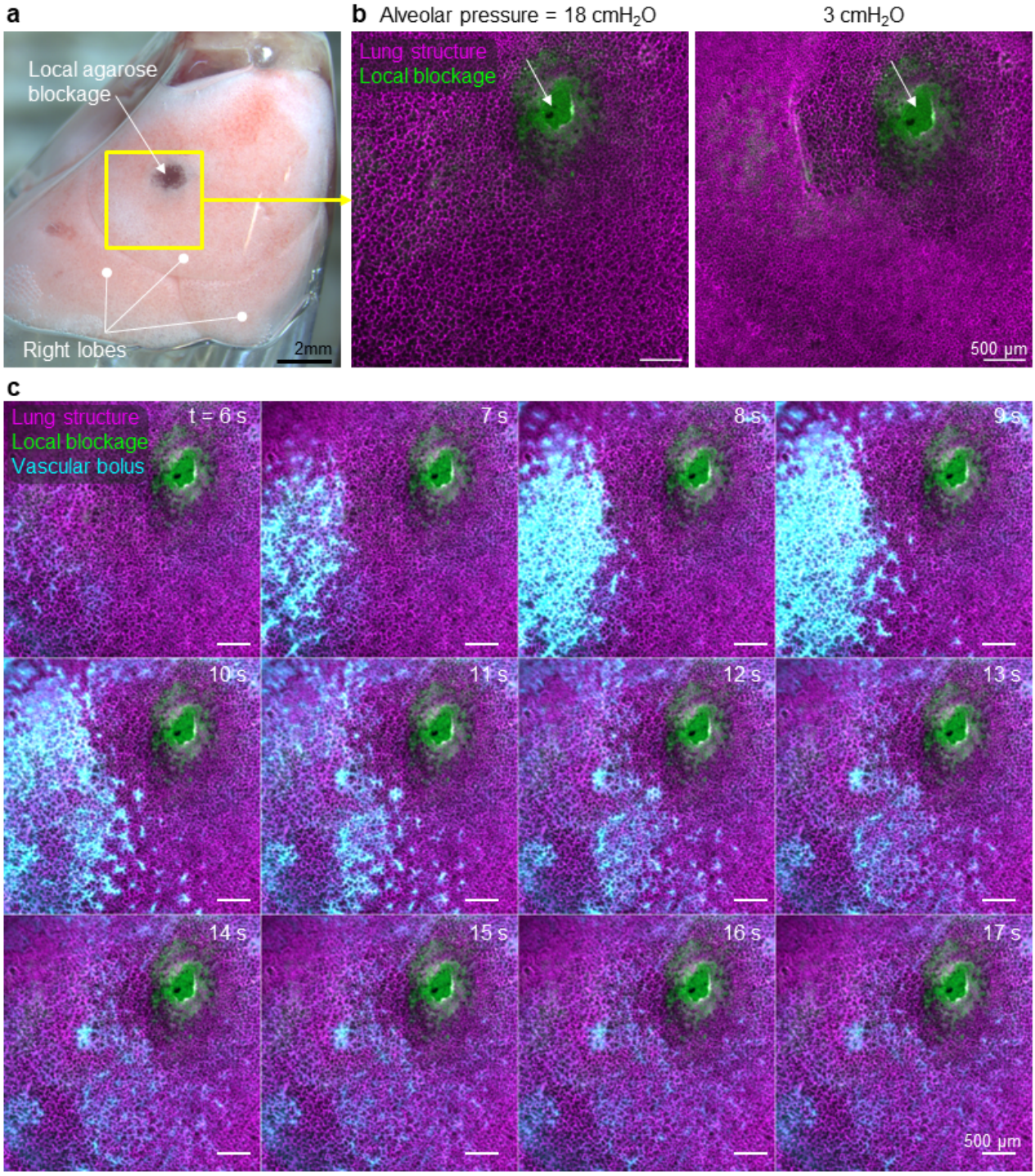

Extended Data Figure 31 | Local agarose blockage disrupts alveolar and vascular dynamics in the lung. (**a**) whole-lobe stereomicroscope view showing agarose labeled with Evans blue injected into the lung subpleural space. (**b**) Confocal microscopy of alveoli near the injected agarose do not change size in response to changing air pressure at the trachea. (**c**) Timelapse imaging of the distribution of a bolus of dye perfused into the lung shows that blood flow is shunted around the injected agarose, so that the vasculature near the agarose is not perfused. Representative data shown for m=2 ROI, for n=1 mouse.

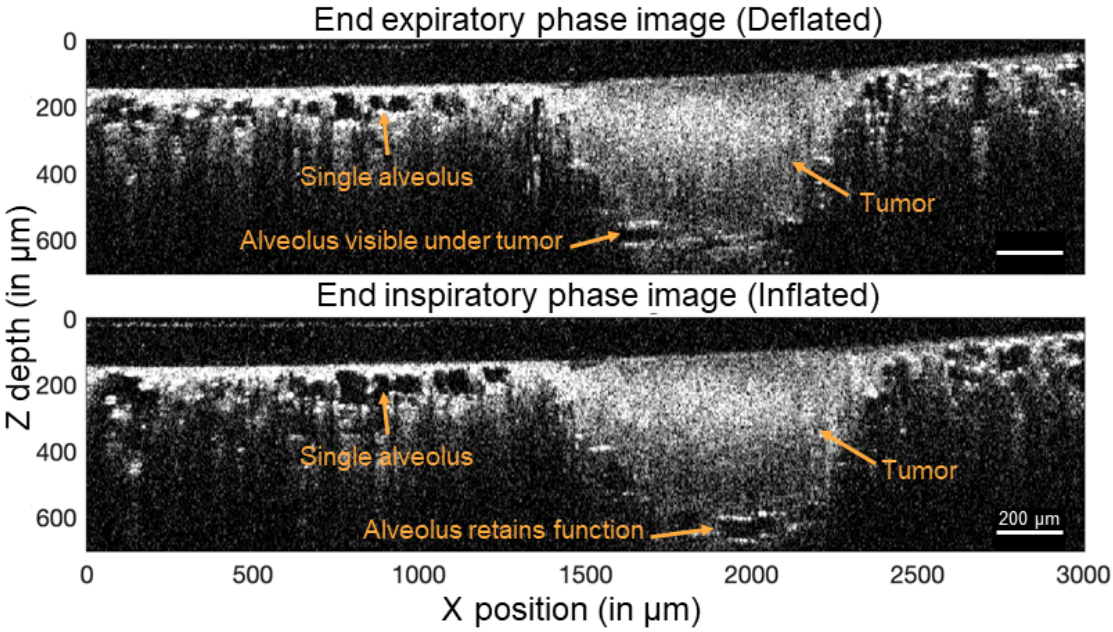

Extended Data Figure 32 | Solid phase nodular growth tumor increases imaging depth in sagittal image section using optical coherence tomography. Alveolar function deeper than 100µm from the surface can be imaged through the tumor nodule up to a depth of 400µm from the surface, as the gas phase of the alveoli is replaced by the solid phase tumor, which reduces light scattering at the air-liquid interface in the alveoli.

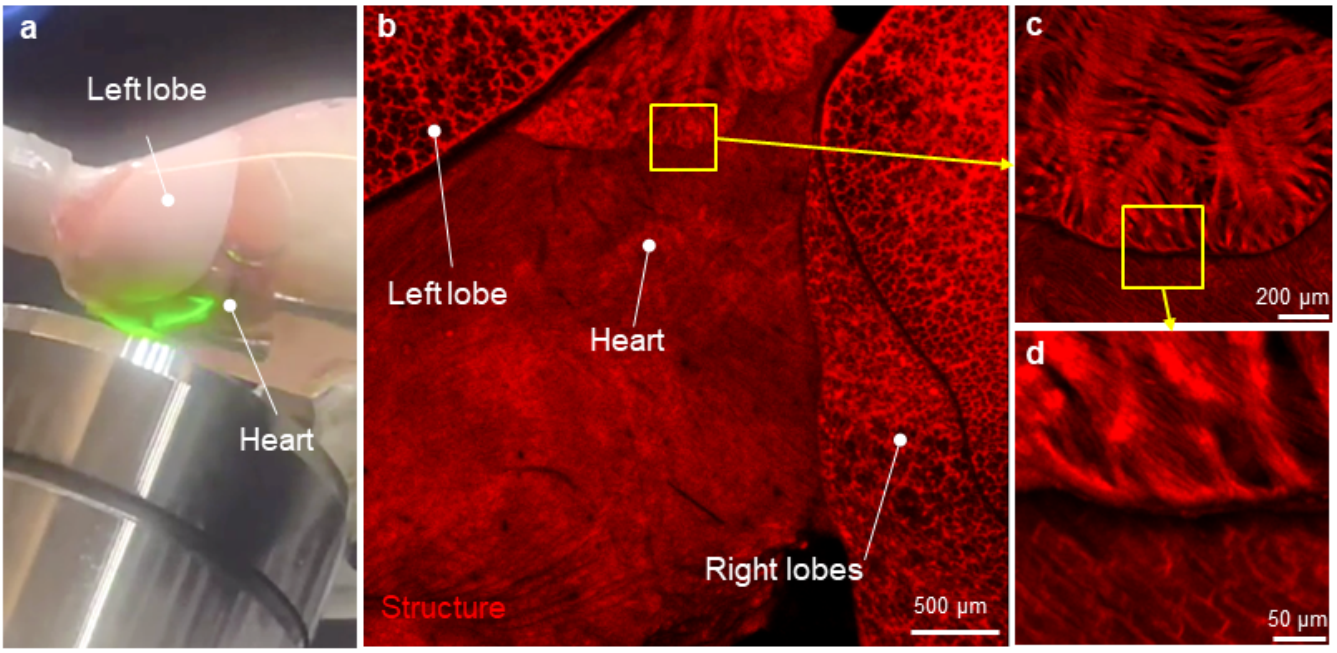

Extended Data Figure 33 | Lung adjacent organs like the heart can also be imaged with the crystal ribcage. Here using a laser scanning confocal (**a**) the heart is imaged with a 1.25x objective to show (**b**) the overlapping lobes of the lung followed by (**c**) higher resolution images of the atrial surface and (**d**) muscle structures.